



**HAL**  
open science

# Carbon steel corrosion scales protectiveness study in CO<sub>2</sub> aqueous solution

Edoardo Basilio

► **To cite this version:**

Edoardo Basilio. Carbon steel corrosion scales protectiveness study in CO<sub>2</sub> aqueous solution. Material chemistry. Université de Lyon, 2021. English. NNT : 2021LYSE1305 . tel-03736581

**HAL Id: tel-03736581**

**<https://theses.hal.science/tel-03736581>**

Submitted on 22 Jul 2022

**HAL** is a multi-disciplinary open access archive for the deposit and dissemination of scientific research documents, whether they are published or not. The documents may come from teaching and research institutions in France or abroad, or from public or private research centers.

L'archive ouverte pluridisciplinaire **HAL**, est destinée au dépôt et à la diffusion de documents scientifiques de niveau recherche, publiés ou non, émanant des établissements d'enseignement et de recherche français ou étrangers, des laboratoires publics ou privés.



N°d'ordre NNT : 2021LYSE1305

**THESE de DOCTORAT DE L'UNIVERSITE DE LYON**  
opérée au sein de  
**l'Université Claude Bernard Lyon 1**

**Ecole Doctorale ED 206**  
**UNIVERSITE DE LYON ÉCOLE DOCTORALE DE CHIMIE**

**Spécialité de doctorat** : Electrochimie  
**Discipline** : Corrosion

Soutenue publiquement le 14 décembre 2021 par :  
**Edoardo Luigi Carlo Basilico**

---

**Carbon steel corrosion scales  
protectiveness study in CO<sub>2</sub> aqueous  
solution**

---

Devant le jury composé de :

De Brauer, Christine, Professeur des Universités INSA Lyon	Présidente
Pébère, Nadine, Directrice de recherche CNRS INP Toulouse	Rapporteuse
Remazeilles, Céline, Maître de Conférences Université de la Rochelle	Rapporteuse
Barker, Richard, Professeur Associé Leeds University	Examinateur
Marcelin, Sabrina, Ingénieure de recherche INSA Lyon	Examinatrice
Normand, Bernard, Professeur des Universités INSA Lyon	Examinateur
Trasatti, Stefano, Professeur Associé Università degli studi di Milano	Examinateur
Ropital, Francois, Professeur PAST INSA, IFP Energies Nouvelles	Directeur de thèse
Fregonese, Marion, Professeur des Universités INSA Lyon	Invitée
Deydier, Valérie, Ingénieur de recherche ANDRA	Invitée
Mingant, Remy, Ingénieur de recherche IFP Energies Nouvelles	Invité



## Abstract

This study is concentrated on the protectiveness of the carbon steel corrosion product scales in CO<sub>2</sub> aqueous conditions. At first, a bibliographic study is performed on the characteristics of a corrosion product layer both from the electrochemical perspective and a structural perspective dealing with its morphology and composition. A specific section is dedicated to pseudo-passivation of carbon steels, a particularly protective condition that forms spontaneously in certain environments. Finally, the effect of relevant impurities presents in industrial environments such as chlorides, calcium ions and oxygen, is analyzed in relation to the protectiveness of the scales and the corrosion processes.

In order to investigate the scales protectiveness and the changes that some inputs have on them pseudo-passivation, a reference experimental condition is selected. Pseudo-passive scales are composed by siderite; magnetite is observed occasionally and never forming a continuous film between the siderite layer and the carbon steel substrate.

The electrochemical reaction mechanism explaining pseudo-passivation is investigated by applying different overpotential and flow conditions on the pseudo-passivated scales. Using the observations obtained with those experiments, an electrochemical impedance model is proposed explaining the behavior of the reactions before and after pseudo-passivity. It is considered that before pseudo-passivation, a simple reduction of the active surface slows down the corrosion of the carbon steel. After the pseudo-passivation, a diffusion limitation attributed to the anodic reaction (going through an adsorbed step process) is proposed.

Finally, the effect of oxygen contamination in CO<sub>2</sub> aqueous conditions is investigated. Oxygen contamination is introduced in the hundreds of ppb range. O<sub>2</sub> changes the corrosion morphology from a uniform corrosion type to a localized one. Inside the localized corrosion features, other phases than siderite such as chukanovite, precipitate. The propagation of the localized corrosion features depth is strongly correlated to the oxygen content of the solution. The propagation of the pits stops when O<sub>2</sub> is not present anymore and for our experimental conditions, a protective pseudo-passive layer is rebuilt. Our results could be explained with an O<sub>2</sub> contamination model already proposed in the literature.

## Résumé

Cette étude se concentre sur la protection de la couche des produits de corrosion de l'acier au carbone dans une solution aqueuse avec du  $\text{CO}_2$  dissous. D'abord, une étude bibliographique est réalisée sur les caractéristiques d'une couche de produit de corrosion tant du point de vue électrochimique que d'un point de vue structurel traitant de sa morphologie et de sa composition. Une section spécifique est dédiée à la pseudo-passivation des aciers au carbone, celle-ci est une condition particulièrement protectrice qui se forme spontanément dans certains environnements. Enfin, l'effet des impuretés présentes dans les environnements industriels tels que les chlorures, les ions calcium et l'oxygène, est analysé en relation avec la protection de la couche des produits de corrosion et les processus de corrosion.

Afin d'étudier la protection de la couche et les changements que certains paramètres ont sur la pseudo-passivation, une condition expérimentale de référence est sélectionnée. La couche pseudo-passive est composée presque uniquement de sidérite ; de la magnétite est observée occasionnellement et elle ne forme jamais un film continu entre la couche de sidérite et le substrat d'acier au carbone.

Le mécanisme de réaction électrochimique expliquant la pseudo-passivation est étudié en appliquant différentes conditions de surtension et d'écoulement de la solution à la couche pseudo-passive. En utilisant les observations obtenues avec ces expériences, un modèle d'impédance électrochimique est proposé pour expliquer le comportement des réactions avant et après la pseudo-passivité. On considère qu'avant la pseudo-passivation, une simple réduction de la surface active ralentit la corrosion de l'acier au carbone. Après la pseudo-passivation, une limitation de diffusion attribuée à la réaction anodique (passant par un processus d'étape adsorbée) est proposée.

Enfin, l'effet de la contamination par l'oxygène dans une solution aqueuse avec du  $\text{CO}_2$  dissous est étudié. Une contamination par l'oxygène est introduite dans la gamme des centaines de ppb. L' $\text{O}_2$  change la morphologie de la corrosion en passant d'un type de corrosion uniforme à un type localisé. À l'intérieur des éléments de corrosion localisés, d'autres phases que la sidérite telle que la chukanovite, précipitent. La propagation de la profondeur de ces éléments de corrosion localisées est fortement corrélée à la teneur en oxygène de la solution. En effet la propagation des piqûres s'arrête lorsque l' $\text{O}_2$  n'est plus présent dans la solution et pour nos conditions expérimentales, une couche protectrice pseudo-passive est reconstruite. Les résultats obtenus pourraient être expliqués avec un modèle de contamination avec  $\text{O}_2$  déjà proposé dans la littérature.





Cyril, Pierre-Jean, Manon je n'aurais pu trouver des colocs et des personnes meilleures que vous en France. Vous m'avez accueilli, vous m'avez fait apprendre la langue, vous m'avez fait sentir chez moi, vous m'avez fait passer des moments entre les meilleures de ma vie. Je vous remercie du fond de mon cœur, je ne pourrais que vous souhaiter du bien dans votre vie n'importe où Dieu a décidé de vous emmener. Rappelez-vous, jamais la polenta au four autrement vous perdrez la dignité. Également merci à M., Mme. Garcia et M. Mme. Frechin pour votre sympathie et bienveillance vers moi.

Maintenant je suis obligé à passer à l'italien, vous m'excuserez si j'abandonne la langue de la « grandeur » pour un instant mais le français est tellement grand qu'il n'arrive pas à passer les cols des alpes.

Un grandissimo grazie a Giulia, Gabriel, Laura, Maxime e tutti gli amici che ho incontrato in R12. Il sostegno reciproco che ci siamo dati in questi anni è stato per me indispensabile per non impazzire definitivamente. Sono anche molto grato a tutti gli amici che mi hanno seguito anche più da lontano senza farmi mancare sostegno e risate. In particolare, un grazie per questo a Ruben, Athos e Mattia. Ringrazio anche gli amici con cui ho condiviso tanti progetti insieme come Vincenzo, Michael e Davide. Tutte le nostre iniziative mi hanno migliorato molto sotto tutti i punti di vista.

Per la prima volta devo ringraziare pure l'Inter che dopo 10 anni di insulti più o meno variopinti è riuscita a vincere nuovamente lo scudetto. Grazie per l'ultima magnifica stagione, per aver lottato e creduto. Sempre e solo forza Inter.

Un ringraziamento speciale va anche ai miei nonni Carlo, Pina, Maria e Luigi. Mi avete insegnato ed ispirato tanto. Soprattutto grazie per avermi fatto apprendere che il lavoro paga sempre, che nulla è precluso ad un gran lavoratore e che l'impegno sul lavoro deve esser motivo di orgoglio. So che non è stato facile per voi vedermi così lontano, ma ho sempre sentito il vostro amore, affetto e supporto ovunque io fossi, così come io lo avrò sempre ed ovunque per voi. Grazie per tutte le belle chiamate che abbiamo fatto, vi voglio tanto bene.

Mamma, Dad, Don Lud non potrò mai ripagare la riconoscenza che ho nei vostri confronti per tutto ciò che siete stati per me. Il vostro sostegno i vostri insegnamenti ed amore mi hanno permesso di arrivare dove sono ora, spero che siate fieri di quello che ho fatto perché lo devo a voi. Sono molto felice di fare parte di questa famiglia perché tutti sanno che ci siamo in ogni momento l'uno per l'altro. Grazie per preoccuparmi sempre per me (a volte eccessivamente), sono attenzioni che rimarcano ogni giorno quanto ci tenete. Non vedervi per così tanto tempo durante la pandemia non è stato semplice per nessuno. Sappiate che vi ho pensato ed amato sempre e così sarà anche in futuro.

Ti ho lasciata per ultima come fai tu durante le cene quando lasci la pietanza che ti piace di più alla fine. Sara senza di te nulla di tutto questo sarebbe stato possibile. Hai supportato la mia decisione di partire all'estero senza esitare dal primo giorno anche se sapevi che sarebbe stato difficile, anche se sapevi che ti avrebbe fatto male. Nonostante il Covid ci abbia tenuto lontani tanto a lungo non mi hai mai fatto mancare il tuo amore ed il tuo sostegno. Ringrazio Dio per ogni istante passato con te, sono stati meravigliosi e mi hanno fatto diventare una persona ed un ricercatore migliore. Grazie per i tuoi infiniti consigli, la tua infinita pazienza, il tuo grande amore. Sei una persona magnifica ed unica, il tuo difetto più grande è che te ne dovresti accorgere di più. Grazie, mille volte grazie per tutto. Non vedo l'ora di affrontare il prossimo capitolo, con tutte le sue gioie e difficoltà, finalmente insieme. Sara, sappi che ti amo tanto ancor più del primo giorno, ora come sempre.

**AD MAIORA**



## INDEX

<b>CONTEXT AND OBJECTIVE</b> .....	<b>1</b>
Context.....	1
Objective.....	2
<b>1 BIBLIOGRAPHY</b> .....	<b>5</b>
1.1 Introduction.....	5
1.2 Solution chemistry .....	5
1.3 Electrochemical reactions in a CO <sub>2</sub> aqueous solution.....	7
1.4 Carbonate layer properties .....	12
1.4.1 Iron carbonate precipitation.....	12
1.4.2 Composition of the corrosion product layer .....	15
1.4.3 Mechanical properties of the corrosion product layer .....	18
1.4.4 Influence of surface microstructure .....	18
1.4.5 Tortuosity .....	20
1.4.6 Pseudo-passivation .....	20
1.5 Contaminants effects.....	22
1.5.1 Influence of chloride ions .....	22
1.5.2 Influence of Calcium cations .....	25
1.5.3 Effect of oxygen .....	27
1.6 Bibliography conclusion .....	29
<b>2 MATERIALS AND EXPERIMENTAL METHODS</b> .....	<b>31</b>
2.1 Material.....	32
2.2 Electrochemical devices.....	33
2.2.1 Electrochemical cells.....	33
2.2.2 Control of pH and dissolved O <sub>2</sub> .....	35
2.3 Electrochemical techniques .....	36
2.3.1 Open circuit potential (OCP).....	36
2.3.2 Electrode polarization.....	36
2.3.3 Linear polarization resistance technique (LPR).....	37
2.3.4 Electrochemical impedance spectroscopy (EIS).....	37
2.3.5 Flow convection - rotating electrode .....	38
2.4 Complementary characterization techniques for scales and carbon steel surfaces.....	39
2.4.1 Mass-loss measurement.....	39
2.4.2 Scanning electrochemical microscopy (SEM).....	39
2.4.3 Grazing incidence X-ray diffraction (XRD).....	40
2.4.4 Raman spectroscopy .....	41
2.4.5 Profilometer.....	41

<b>2.5</b>	<b>Experimental protocols.....</b>	<b>42</b>
2.5.1	Standard protocol for the electrochemical tests .....	42
2.5.2	Dissolved iron setup for pseudo-passivation acceleration .....	43
2.5.2.1	Static conditions.....	43
2.5.2.2	Dynamic conditions .....	44
2.5.3	Reference conditions for pseudo-passivation, pH 6.8.....	44
2.5.4	Studying the “pseudo-passivation” protection mechanism.....	45
2.5.4.1	Potentiodynamic polarization test.....	45
2.5.4.2	The effect of potential.....	45
2.5.4.3	The effect of convection .....	46
2.5.5	Effect of an oxygen contamination.....	47
2.5.5.1	Potentiodynamic polarization test with O <sub>2</sub> contamination .....	47
2.5.5.2	Oxygen contamination test .....	47
2.5.5.3	Lower temperature oxygen contamination.....	48
2.5.5.4	Oxygen introduction in pseudo-passive state.....	48
2.5.5.5	Recovery test.....	49
<b>2.6</b>	<b>Experimental conditions summary.....</b>	<b>50</b>
<b>2.7</b>	<b>Conclusions.....</b>	<b>53</b>
<b>3</b>	<b>IDENTIFICATION OF A REFERENCE CONDITION.....</b>	<b>54</b>
<b>3.1</b>	<b>Iron buffering method occurred at pH 6.6 .....</b>	<b>54</b>
3.1.1	Static conditions. ....	54
3.1.2	Iron buffering method, dynamic conditions.....	58
3.1.2.1	Experiments without rotation of the electrode. ....	59
3.1.2.2	Experiments with 180 rpm rotation .....	61
3.1.2.3	Experiments with 600 rpm rotation .....	62
<b>3.2</b>	<b>Experiments at pH=6.8, static electrode .....</b>	<b>65</b>
<b>3.3</b>	<b>The onset of pseudo-passivation .....</b>	<b>67</b>
<b>3.4</b>	<b>The choice for a reference condition .....</b>	<b>68</b>
<b>4</b>	<b>STUDYING THE “PSEUDO-PASSIVATION” PROTECTION MECHANISM .....</b>	<b>70</b>
<b>4.1</b>	<b>The effect of an applied potential to the electrode .....</b>	<b>72</b>
4.1.1	Potentiodynamic polarization .....	72
4.1.2	Electrochemical characterization of the scales before pseudo-passivation (active scales) .....	73
4.1.3	Electrochemical characterization of pseudo-passive scales.....	77
4.1.4	Analysis of the results on the influence of potential.....	81
4.1.5	Discussion on a possible mechanism.....	83
<b>4.2</b>	<b>The effect of convection on the pseudo passivity .....</b>	<b>85</b>
<b>4.3</b>	<b>Conclusions on the investigations of the pseudo-passive state protection mechanism.....</b>	<b>88</b>
<b>4.4</b>	<b>Modeling scales protectiveness before and after pseudo-passivation.....</b>	<b>89</b>
<b>4.5</b>	<b>Conclusion on modeling pseudo-passivity.....</b>	<b>90</b>

<b>5</b>	<b>OXYGEN CONTAMINATION .....</b>	<b>91</b>
5.1	Potentiodynamic polarization .....	93
5.2	Oxygen contamination test introduced at $t_0=0$ .....	94
5.3	Contamination test at a lower temperature .....	101
5.4	Introduction of $O_2$ in pseudo-passive state .....	103
5.5	Recovery test.....	107
5.6	Conclusions on the oxygen contamination in a $CO_2$ saturated aqueous solution. ....	113
<b>6</b>	<b>SUMMARY AND GENERAL CONCLUSIONS .....</b>	<b>115</b>
<b>7</b>	<b>PERSPECTIVES .....</b>	<b>117</b>
<b>8</b>	<b>REFERENCES .....</b>	<b>118</b>

# Context and objective

## *Context*

This study is focused on the protectiveness of the corrosion product layer (CPL) that forms spontaneously in certain condition over carbon steel in a carbon dioxide aqueous solution. This film has important properties in term of corrosion protection since it can decrease the value of the uniform corrosion rate caused by the corrosiveness of the solution. The nature of the corrosion product layer depends strongly on the precipitation conditions and other environmental parameters like the temperature.

Carbon steel is a widely diffused material in the industrial domain because it combines good mechanical properties with contained cost. Moreover, carbon steel can be machined easily and even welded. However, carbon steel is particularly exposed to the risk of corrosion because it does not develop a protective film by itself as it is the case for stainless steels. Stainless steels are more expensive and could have some problems related to intergranular corrosion when welded. Because of the susceptibility to corrosion, appropriate measures for containing the corrosion must be put in place for safety, cost and environmental reasons.

A good protection from uniform corrosion is particularly welcome for carbon steel in the case of CO<sub>2</sub> aqueous solutions because the dissolution of carbon dioxide into water makes the environment naturally acid.

Carbon dioxide aqueous solutions are found in several industrial application, a classical issue was the corrosion in the upstream part of the pipelines for oil extraction. In that case carbon dioxide could be found in the well or in the injection well as a result of enhanced oil recovery operations.

However, this environment is also common in the technologies related to a sustainable development such as carbon capture and storage (CCS), biofuels production and geothermal energy production (Figure 1 and Figure 2). Also, for underground nuclear waste storage, the water in contact with the carbon steel surrounded by concrete is rich in carbonates CO<sub>3</sub><sup>2-</sup> and can promote the formation of a corrosion product layer akin to the one originating from a CO<sub>2</sub> solution.

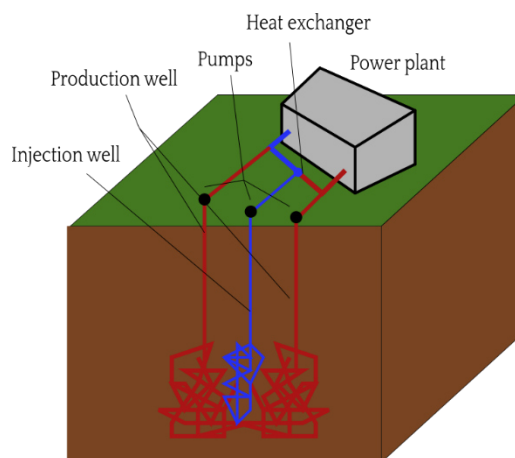


*Figure 1 Geothermal energy production plant diagram.*

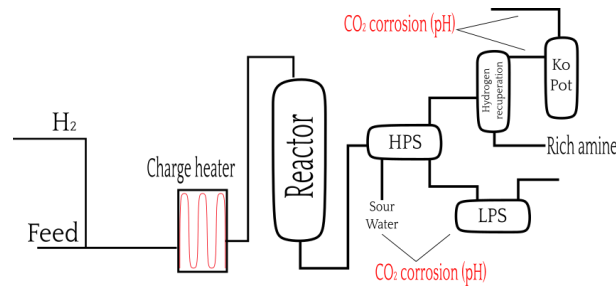


Figure 2 Corrosion in bio-fuel refining diagram.

Geothermal energy consists in exploiting the heat naturally produced by the earth in order to generate energy through steam. Water is pumped into the earth crust in a hot zone where it is heated. Afterward the hot fluid emerges through a pipeline and it goes to a turbine where electrical energy is generated. In geothermal energy applications, the pipelines transporting hot water from the geological reservoir to the energy production site contain scaling ions such as carbonates that promote the formation of a corrosion product layer. The high temperature of the fluid promotes both carbon steel corrosion and the precipitation of the scales. However the corrosion product layer (CPL) morphology, nature and its related protectiveness depend from the operating temperature [1]. The same problem arises when the fluid reaches the power plant in the heat exchanger because of the composition of the feedwater and the temperature. Besides the precipitation of corrosion products, other ions present in the feed may precipitate inside the solution because the saturation threshold of a specific compound is crossed. Fouling and inefficient heat transfer can be the result of the precipitation of mineral compounds in the feed water. The formation of scales with its related fouling problems affect even stainless steels [2,3]. The removal of these unwanted precipitates is responsible for additional costs and productivity loss. However, the presence of other ions can also affect the corrosion product layer altering its properties leading to a lower protectiveness.

Carbon capture and storage is a complex technology where  $\text{CO}_2$  is involved all along the process from its capture inside the industrial facilities to its disposal into the geological site designated for the purpose. The conditions of temperature and pressure are dependent on the part of the process considered: pipelines and storage vessels are particularly concerned because of the material they are made (carbon steel) and the conditions of temperature and pressure of carbon dioxide. A great variety of industrial processes are eligible for capture of their  $\text{CO}_2$  emission such as hydrogen protection from steam reforming. Unfortunately, it means that the impurities present in the  $\text{CO}_2$  stream are not constant neither in nature nor in concentration. Some impurities that can be found in CCS applications are  $\text{O}_2$ ,  $\text{NO}$ ,  $\text{NO}_2$ ,  $\text{SO}_2$  and  $\text{H}_2\text{S}$  each one with specific reactions producing characteristic feature for  $\text{CO}_2$  aqueous solution [4]. Sometimes impurities can be beneficial to the protectiveness of the corrosion product layer which is the case of small quantities of  $\text{H}_2\text{S}$  whereas in other cases such as acetic acid, corrosion rates increase as a result of the more aggressive medium.

## Objective

The objective of the PhD thesis is focused on the study of the protectiveness of the corrosion product layer that spontaneously form on carbon steel when immersed in a  $\text{CO}_2$  aqueous solution. Evaluating the protectiveness of the scales means ultimately to know the corrosion morphology, to determine the corrosion rate of the sample and to understand the corrosion mechanism. Understanding these parameters is essential in order to foresee the corrosion behavior in this environment even in different experimental conditions.

Therefore, a first objective of the thesis is to characterize the corrosion mechanism of carbon steel in the presence of the scales in order to identify how the film protects the surface.

The precipitation of the scales depends on the exposure time and the experimental conditions where they precipitate. Therefore, in order to study reproducibly the impact of external variables on the protectiveness of the scales, a reference condition either of protectiveness either of experimental conditions (temperature, pH exposure time) has to be found. Pseudo-passive state was identified as a good starting point for several reasons, because it is easily identified with electrochemical measurements and represents a highly protective condition in all cases and the conditions that promote pseudo-passivation are known. On the other side, the drawbacks are that pseudo-passivation time cannot be predicted and the conditions producing pseudo-passivity are narrow.

Moreover, the reasons explaining why the corrosion layer becomes pseudo-passive and how the electrochemical reaction are slowed down so to ensure the relative protection, are still debated. There is not a consensus on the protection mechanism that leads to an enhanced corrosion protection during pseudo-passivation. Therefore, studying pseudo-passivity was motivated by the need to find an explanation elucidating the way the scales protect the surface before and after pseudo-passivity.

Furthermore, the solutions normally encountered in the industrial environment are more complex than a simple CO<sub>2</sub> aqueous solution. Other chemical species such as Ca<sup>2+</sup> ions or oxygen can alter the scales so much that the corrosion morphology and rates are significantly changed because of the interaction between those chemicals, the corrosion product layer and the electrochemical reactions. Besides dissolved ions, gas impurities can be present with carbon dioxide. For instance, H<sub>2</sub>S is one of the impurities present in oil extraction and refining. Excluding hydrogen embrittlement problems, H<sub>2</sub>S can be beneficial increasing scales protectiveness [5]. For carbon capture and storage application, oxygen can be a contaminant impacting on the scales and whose effect must be investigated further.

Therefore, the investigation of the protectiveness of the scales in a CO<sub>2</sub> aqueous solution with small concentration of oxygen is set as an objective. Particularly the aim is to determine whether a change in the layer composition, structure, corrosion morphology or rate arises in the presence of a small oxygen contamination. In the literature the effect of O<sub>2</sub> was studied in a complex chemistry solution and with a concentration in the order of the ppm. In this study the oxygen will be analyzed in a simple system, previously characterized, with a one order of magnitude less dissolved oxygen in the solution. Furthermore, the oxygen effect will be studied both on an already protective corrosion product layer and on a bare steel surface. Finally, a simulation of a temporary contamination will be performed on protective scales.

A target was to determine if a concentration threshold exists after which the effects of oxygen are relevant. For this case O<sub>2</sub> was introduced starting at the beginning of the test and the evolution of the system was followed. The experimental conditions adopted previously for scales pseudo-passivation will be reused for investigating the O<sub>2</sub> effect. In those conditions, the possible dissolved oxygen concentrations are in the order of the hundreds of ppb. Therefore, this study will address this range of concentration testing the response of the corrosion coupons and working electrodes at increasing dissolved oxygen concentration.

Another target was to assure that the observed variations in CO<sub>2</sub> aqueous corrosion were truly due to oxygen and what could happen in the case of a temporary and accidental contamination. Thus, the oxygen contamination was introduced in pseudo-passive state and the oxygen feed was interrupted in a second moment. The samples were then analyzed with surface analysis techniques before and after the contamination in order to observe the variations that O<sub>2</sub> had on the scales and corrosion process.

## *Structure of the document*

This document is divided in five chapters. The first one will deal with a bibliographic review of the literature concerning corrosion in CO<sub>2</sub> aqueous environments. The chemistry of CO<sub>2</sub> aqueous solution will be analyzed. Both anodic and cathodic processes will be considered in relation to this environment. Afterwards the precipitation of the corrosion product layer will be considered. Both the conditions in which precipitation is promoted and the impact of the scales on the electrochemical reactions will be analyzed. A literature section will be dedicated to pseudo-passivation, a particularly protective condition of the corrosion product layer. Finally, the effect of some chemical contaminants on the corrosion product layer will be discussed. Particularly Ca<sup>2+</sup> ions and chlorides that are commonly found in the operative solutions will be considered as their influence on the film of corrosion products is significant. Gas contaminants are as important as mineral dissolved ions for the evolution of the scales, particularly oxygen plays an important role in CCS applications and has a significant impact on the corrosion product layer and the associated corrosion properties.

The second chapter will be dedicated to the experimental techniques and procedures adopted for investigating the protectiveness of the scales. In the first section the approaches to obtain pseudo-passive scales will be considered. Afterwards a description of the material and the used electrochemical cells will be reported. The following two sections will deal with the adopted electrochemical and surface analysis techniques. In fact, a synergy between these two investigation methods are needed in order to elucidate the relationship between the scales' protection and their composition. Those sections will report the techniques parameters as well as the reason for their choice in this study. Finally, the experimental methods used for obtaining the experimental results will be described. At the end of the chapter a summary of all the experimental conditions will be reported

The three following chapters are dedicated to the presentation and the discussion of experimental results. The third chapter will concern the development of adequate scaling conditions. These experimental parameters are key features for the following investigation of the scales since they must be reliable for the precipitation of pseudo-passive scales. However, several conditions were tested in order to find the most suitable for the following analysis to be made.

The fourth chapter will exploit those conditions for investigating the properties of a pseudo-passive corrosion product layer. Impedance spectroscopy will be the key technique in this section investigating the electrochemical response of the reactions after applying a given stimulus. Specifically, the effect of potential and the effect of convection on the electrochemical reaction in pseudo-passive state will be studied. Based on the observations collected through impedance and other electrochemical techniques in pseudo-passive state, an electrochemical model was proposed. This model aims to explain how the electrochemical reactions change through the exposure to the corrosive solution and the precipitation of the scales.

Finally, the fifth chapter will address the effect that a small O<sub>2</sub> contamination (hundreds of ppb) has on the corrosion product layer protectiveness. At first oxygen was introduced since the start of the test at various concentrations. This procedure was meant to observe the effect of different oxygen contamination concentration on the film. Afterwards the effect of oxygen directly introduced in pseudo-passive conditions was investigated. This last experiment was designed both for better understanding the role of oxygen on the film and to simulate the case of an accidental contamination.

# 1 Bibliography

## 1.1 Introduction

The bibliographic section concerns the issues related to carbon steel corrosion in a CO<sub>2</sub> water solution, particularly the effects played by the corrosion product layer over carbon steel corrosion performances. As it was mentioned in the introduction, particular environmental circumstances such as pH and temperature cause precipitation of iron carbonate scales, which protect the surface hindering the corrosion process, leading to smaller corrosion rates for the protected surfaces. CO<sub>2</sub> (also called sweet) corrosion can also be dangerous when non-uniform scale precipitation due to local surface conditions occurs. A small part of the surface is not protected and as a result, pitting-like phenomena takes place leading to unexpected failure of the material [6] The effect of some impurities on the corrosion process is analyzed in the final part of this bibliographic chapter. A deeper discussion related to chemical impurities can be found in the following reference [7].

## 1.2 Solution chemistry

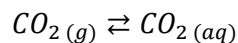
In this section, the CO<sub>2</sub> aqueous solution is described in order to understand all the chemical species that can participate in the corrosion process as electrochemical reagents or precipitating ions.

CO<sub>2</sub> dissolved into water is responsible for complex solution chemistry, which determines the aggressiveness of the environment towards the metal. Carbon dioxide dissolution into water is the first step of the process. CO<sub>2</sub> dissolved concentration can be calculated through Henry's (Equation 1). If not specified, the entire chemical species are intended as dissolved into the solution (aqueous, *aq*).

$$[CO_2] = K \cdot p_{CO_2}$$

*Equation 1*

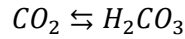
Henry's law assumes that the considered gas is in equilibrium between the gas phase and the aqueous phase (*Reaction 1*).



*Reaction 1*

Proportionality constant *K* is dependent on the temperature and the salt concentration. For higher temperature and ionic force values, the values of *K* decrease its value, therefore carbon dioxide solubility in water decreases. Henry's law is independent of the considered gas as long as the proper Henry's constant is considered, and the gas does not dissociate when dissolved into water. Other limitations of the law are that gas ideal conditions are assumed. Henry's law is more relevant to experimental results when the gas solubility is low, thus when the molar fraction of the gas is negligible with respect to the liquid, in the opposite case Raoult's law applies.

Unlike oxygen, carbon dioxide is not inert in H<sub>2</sub>O and it reacts with water itself. Dissolved carbon dioxide undergoes a hydration reaction (*Reaction 2*), which produces carbonic acid H<sub>2</sub>CO<sub>3</sub> (*Reaction 3*).



Reaction 2

$$K_{Hyd} = \frac{[H_2CO_3]}{[CO_2]}$$

Reaction 3

The reaction is regulated by its reaction constant ( $K_{Hyd}$ ) as any other chemical reaction: since water is the solvent its contribution is considered constant in the reaction constant equation. The value of  $K_{hyd}$  at 25°C is  $1.7 \cdot 10^{-3}$  and  $1.2 \cdot 10^{-3}$  in pure water and seawater, respectively [8]. Dissolved carbon dioxide is the principal species in the reaction. The reaction constant are defined by the concentrations of the chemicals, this assumption is valid only for low concentrations when the activity coefficient is close to unity, otherwise, chemical activities have to be used.

In an open system, namely, a system where carbon dioxide partial pressure remains constant, the carbonic acid concentration is also constant. All the tests in this study are in open system conditions since the aqueous solution was kept saturated with  $CO_2$  at any time with continuous bubbling inside the aqueous phase. The product of  $CO_2$  hydration reaction,  $H_2CO_3$ , is a diprotic acid with two dissociation constants  $K_{a1}$  and  $K_{a2}$  (Reaction 4). Hereafter the reactions involving carbonic acid are reported along with their respective equilibrium equations.

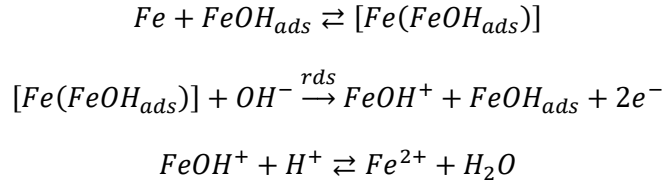


Reaction 4

The dissociation reactions are responsible for both a decrease in pH solution which favors corrosion and the presence of carbonate ions that are involved in the iron carbonate scales formation [6]. The dissociation constants for  $H_2CO_3$  as for all the acids depend on the ionic constants and the temperature. At 25°C in seawater, the pKa are 5.85 and 8.90 for the first and the second dissociation respectively [9]. These low values are quite important because they keep  $CO_2$  inside the validity limit of Henry's law due to their low dissociation constant. As expected, the values of pKa confirm that  $H_2CO_3$  is more acid than bicarbonate ions.

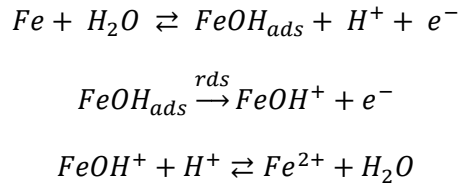
The dissociation of carbonic acid is of paramount importance in  $CO_2$  aqueous solution because it results in the formation of carbonate ions. Carbonate ions are responsible for the precipitation of relevant insoluble salts such as calcium carbonate or iron carbonate which is the main subject of this study. These precipitates are responsible for dangerous phenomena for industrial facilities such as pipe fouling, or beneficial outcomes such as corrosion protective scales.





*Reaction 5 [14]*

Determination of the anodic reaction mechanism is a key step in order to foresee the kinetics of the corrosion process. Heusler and Bockris investigated the anodic iron dissolution without CO<sub>2</sub> using steady-state techniques proposing two different mechanisms with an anodic slope of 30mV/dec and 40 mV/dec respectively [14–16]. The Heusler mechanism is dubbed catalytic whereas Bockris mechanism is called consecutive (*Reaction 5*, Heusler and *Reaction 6*, Bockris). However, the only use of steady-state techniques is considered not sufficient for unveiling an electrochemical reaction mechanism. Steady-state and transient techniques should be used together in order to have a complete picture of the ongoing electrochemical processes to allow the identification of all the mechanisms and the presence of intermediates at the surface.



*Reaction 6 [15,16]*

Besides Heusler and Bockris mechanisms, Keddum *et al.* investigated the iron dissolution reaction in an acid aqueous solution in a sulfate anoxic environment [12,13]. In order to do that, electrochemical impedance spectroscopy (EIS) was performed at several potentials of the polarization curves. The selected potentials were in the active, pre-passive and passive domain. The time constants that were detected with the impedance measurements were analyzed so as to relate them with a reaction mechanism. Figure 4 reports the mechanism developed in the study. The key player in the mechanism is a Fe(I) species, the passage between pure iron and Fe(I) is irreversible. Following this first step, several other reaction pathways open up that lead to Fe<sup>2+</sup> dissolved in solution. Three intermediates species are therefore considered: Fe(I), a Fe(I) excited state Fe<sup>\*</sup>(I) and Fe<sup>\*</sup>(II). The kinetic constants were simulated by Keddum as a function of the solution pH. Anyhow the solution investigated was in the acid range (max. pH 5) and in deaerated sulfate solutions. Although the proposed mechanism is insightful, it lacks one of the protagonists of CO<sub>2</sub> aqueous corrosion which is indeed CO<sub>2</sub>.

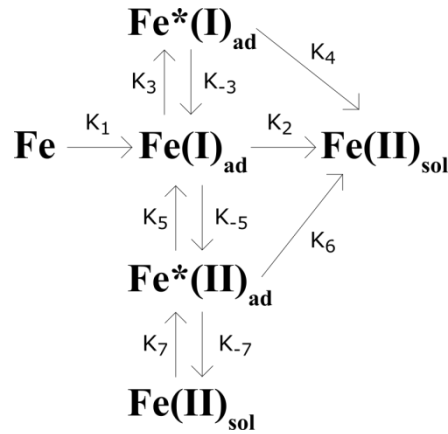
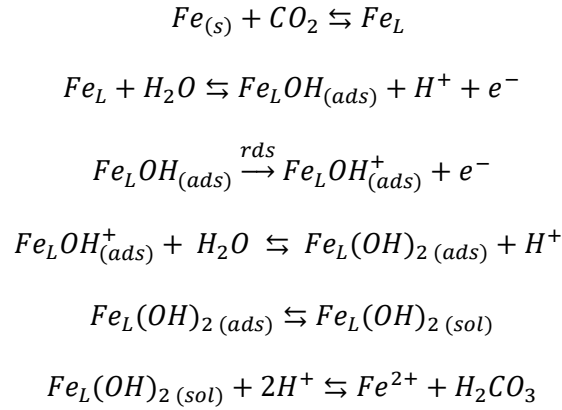


Figure 4 Keddam mechanism schema [12,13].

In fact, the involvement of carbon dioxide in the anodic process of iron dissolution remains not clear in the literature. A mechanism involving a complex Fe-CO<sub>2</sub> formed through direct adsorption of carbon dioxide on the metal surface (*Reaction 7*) is proposed by Nesic *et al.* [17]. It was used to explain the different orders of reaction and Tafel slopes measured in different pH and P<sub>CO<sub>2</sub></sub> conditions. Similarly, the role of carbon dioxide on the anodic reactions was investigated by Kahyrian *et al.* through steady-state techniques at different CO<sub>2</sub> pressures [18]. The authors claim that the involvement of CO<sub>2</sub> in the reaction is proven by the slightly different Tafel slope coefficient for different carbon dioxide partial pressures. Wright *et al.* used potentiodynamic polarization in CO<sub>2</sub> saturated and deaerated solutions [19] for different pH of the electrolyte. The solution was adjusted using either NaOH or NaHCO<sub>3</sub>/Na<sub>2</sub>CO<sub>3</sub> to have different ion concentrations in the solution. The results show higher anodic currents in the case of CO<sub>2</sub> saturated solutions in the presence of carbonate and bicarbonate ions. The authors proposed that the exchange current of the anodic reaction linearly depends on the concentration of CO<sub>2</sub>, HCO<sub>3</sub><sup>-</sup> and CO<sub>3</sub><sup>2-</sup>. An increase of their concentration would produce higher anodic currents during the anodic sweep and as a consequence, an increase of the corrosion rates. In any case, no detailed mechanism was proposed in this work. The effect of carbonate ions (CO<sub>3</sub><sup>2-</sup>) on deaerated and CO<sub>2</sub> saturated aqueous solutions at high pH conditions was studied by Martinelli-Orlando *et al.* [20] where two buffer solutions, namely HCO<sub>3</sub><sup>-</sup>/CO<sub>3</sub><sup>2-</sup> and borate/NaOH, were tested with a pH equal to 9.8. The potentiodynamic polarization experiments also show higher currents during the anodic sweep in the case of a CO<sub>2</sub> saturated solution. The authors suggested that the precipitation of iron carbonates lowers the equilibrium potential of the anodic reaction due to a lower concentration of Fe<sup>2+</sup> ions. The authors also proposed a direct reduction of HCO<sub>3</sub><sup>-</sup> that leads to a rise of the open circuit potential (OCP) and an increase of the corrosion current density (*i*<sub>corr</sub>). Therefore, the presence of CO<sub>2</sub> and carbonates have opposite outcomes related to the magnitude of *i*<sub>corr</sub> but the authors were not able to determine which of the two mechanisms is predominant.



*Reaction 7 [17]*

Nevertheless, the Tafel slope coefficients obtained in Kahyrian study [21] are not so dissimilar and they can be explained by an experimental error that was observed by Almeida *et al.* [22]. Moreover, they sustain that the use of steady-state techniques only is not sufficient to prove the contribution of carbon dioxide to the iron dissolution reaction. In fact, the importance of supporting the steady-state technique results with transient techniques such as EIS was remarked. Previously, EIS was used by Almeida *et al.* to verify the effect of different carbon dioxide partial pressures at pH 4 [23]. With those measurements, the authors observed one inductive loop attributed to the adsorption of FeOH intermediates as it was previously identified by Keddam [12,13]. Moreover, through an impedance mechanism analysis, the authors showed that at the studied pH, the eventual direct adsorption of CO<sub>2</sub> would produce a second inductive loop. Therefore, Almeida *et al.* concluded that no direct adsorption of carbon dioxide on the metal surface occurs but they did not exclude eventual adsorption of carbon dioxide on other surface intermediate species. Nevertheless, Almeida *et al.* drew their conclusion from the above-mentioned impedance measurements performed at pH 4 only: this does not consider the great variety of environmental conditions that can be encountered dealing with CO<sub>2</sub> corrosion in an aqueous environment.

Moreover, Barcia and Mattos investigated the effect of chloride ions on the carbon steel iron dissolution mechanism [24]. An interpretation of the impedance diagrams was proposed. Chloride ions, above a critical concentration, influence the secondary reaction pathways forming a Fe<sup>2+</sup>(I) oxidized species different from the one proposed in the Keddam mechanism presented in Figure 4. Neither in this case, direct adsorption of chloride ions on the bare surface takes place. Therefore, the authors used this example besides the above-mentioned experimental results to exclude the possibility of direct CO<sub>2</sub> adsorption on Fe(0).

Similar to the CO<sub>2</sub> adsorption mechanism proposed by Nescic *et al.* [17], Xiang *et al.* explained that sulfur species such as HSO<sub>3</sub><sup>-</sup> can adsorb on carbon steel producing higher anodic currents during potentiodynamic polarization in a CO<sub>2</sub>/SO<sub>2</sub> aqueous environment. However, even in this study, steady-state techniques only were applied [25].

The carbonic species dissolved into water have a major impact on the electrochemical reactions, the presence of CO<sub>2</sub> increases the corrosion rate in the case of two solutions at the same pH (one without and one with CO<sub>2</sub>) either because of a direct reduction or “buffering effect” mechanism. An increase of the anodic current is observed with higher carbon dioxide partial pressure. The role of CO<sub>2</sub> in the anodic dissolution has yet to be completely understood. The electrochemical impedance spectroscopy did not allow to observe the direct adsorption of CO<sub>2</sub>.

The other actor of the corrosion process is the metal itself; carbon steel plays a minor part if compared to the corrosion of stainless steel, nevertheless, the perlite present at the surface plays a role in cooperation with the corrosion product layer.

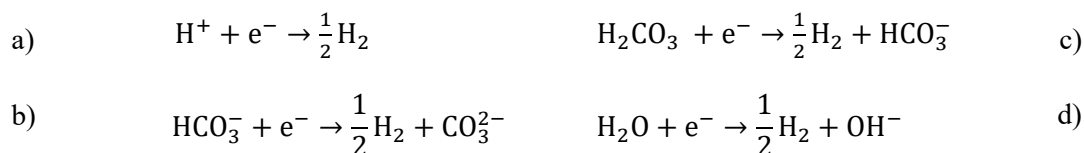
The mechanism of the anodic reaction in CO<sub>2</sub> aqueous solution is still debated. Shedding light on this matter would be beneficial for the understanding of the corrosion process as a whole and in the case of other system perturbations. After the analysis of the anodic reaction in this environment, the following section deals with the mechanism of the cathodic reactions.

### *Cathodic reaction*

In an anoxic acid solution, the key cathodic reaction is the proton reduction: by increasing the pH, water can be an oxidizing agent instead of H<sup>+</sup>. This matter has been extensively studied in the literature. However, two main visions are still present in the scientific community related to the participation of carbonate species in the cathodic processes of a CO<sub>2</sub> aqueous solution.

Previous scientific studies present two different approaches: the direct reduction of carbonate species and the “buffering effect”. Those two mechanisms do not exclude each other but understanding which one is more relevant to explain the carbon dioxide influence over the cathodic processes and thus the corrosion rate is crucial. However, the most recent works bring more evidence supporting the “buffering effects” mechanism. Anyhow, contrarily to the anodic processes, the debate on the cathodic reactions is focused on a narrow range of mechanisms.

The “buffering effect” takes into account only the proton reduction (*Reaction 8 a*) whereas the direct reduction of carbonic acid and bicarbonate ion is deemed possible in the case of a direct reduction mechanism (7 b-c). In the “buffering effect” the contribution of carbonic acid and bicarbonate ion acts simply as a reservoir of protons to be reduced. Particularly the dissociation of carbonic acid gives additional protons to the systems more than the free protons available due to the pH of the solution.



### *Reaction 8*

A rotating disk electrode was used by Remita *et al.* to quantify the contribution of the buffering effect related to the bicarbonate ions [26]. The measured potentiodynamic polarization curves both in CO<sub>2</sub> saturated and deaerated solutions show a potential zone with a kinetic control regime and, at higher potentials, a mass-transfer control one. The cathodic limiting currents are higher in the presence of carbon dioxide, but they do not follow a linear function versus the square root of the electrode rotation speed as per Levich’s equation. The authors developed a model considering only the proton reduction reaction and the buffering effect: this model fits with the experimental polarization curves for each rotation speed for both the desaturated and the CO<sub>2</sub> cases. Therefore, it has been proved that the higher limiting current measured for the CO<sub>2</sub> case could be explained without considering acid carbonate or bicarbonate electrochemical reduction directly on the surface. Confronting the two solutions, the cathodic currents in the kinetic control potential range have similar values. If the mechanism of the cathodic reaction involves the direct reduction of carbonic acid, the presence of carbon dioxide and related ions produces a higher current even in the activation-controlled domain.

A similar approach was used by Kahyarian *et al.* to generalize the buffering mechanism even in the presence of hydrogen sulfide [27–29]. Their model considers proton reduction as the only cathodic reaction possible. Furthermore, the model includes the flux equations for the determination of the rates of the homogeneous reactions related to all the acids and conjugated bases present in the corrosive solution. The proposed model can foresee even the second limiting current plateau during the cathodic reaction in the presence of H<sub>2</sub>S as well as the cathodic polarization in the case of a CO<sub>2</sub> saturated solution. Therefore Kahyarian *et al.* concluded that the shape of the polarization curves depends on the solution pH and the pK<sub>a</sub> of the first and second conjugated bases and excluded any significant direct reduction of carbonic acid.

On the other side, several authors reported the direct reduction mechanism to explain the higher corrosion rate that was measured in the case of higher carbon dioxide or acetate dissolved concentrations. In another study, Nesic *et al.* reported higher corrosion limiting current in a water solution containing carbon dioxide than in a HCl solution and at the same pH [30]. They attributed this effect to the direct reduction of carbonic acid on the metal surface. However, this interpretation is at variance with one of their other studies [31]. An increase of the corrosion rate was also observed by Gulbransen *et al.* at increasing the acetic acid concentration in the solution even if the anodic part, *i.e.* iron dissolution, was inhibited as showed by potentiodynamic polarization [32]. This effect on the corrosion rate measured with LPR and mass loss was attributed to the direct reduction of carbonic and acetic acid.

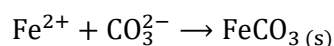
Concerning the effect of NaCl, Fang *et al.* reported a decrease in the cathodic limiting current when the NaCl concentration goes up to 10-20% wt. Although a higher salt concentration increases the conductivity of the solution thus reducing the ohmic drop between the anodic and cathodic areas, it diminishes the carbon dioxide solubility in the water as well. As a result, a carbonate ion concentration depletion in the solution occurs leading to a lower saturation value of iron carbonate [33].

In the previous two sections, the behavior of the anodic and cathodic reactions was considered. Their analysis is necessary in order to understand how the corrosion product layer could protect the metal. In the following sections, the interplay between the CO<sub>2</sub> aqueous solution and the products of the electrochemical reactions is considered, particularly related to the precipitation of iron carbonates.

## 1.4 Carbonate layer properties

### 1.4.1 Iron carbonate precipitation

In certain conditions, carbon steel is covered by iron carbonate scales which are the results of the corrosion process in a carbon dioxide solution. Iron carbonate is an insoluble compound whose solubility product is  $1.28 \cdot 10^{-11}$  at 25°C and whose ionic strength (I) is equal to 0 [5]. It is formed thanks to dissolved Fe<sup>2+</sup>, produced by the corroding surface, and carbonate ions, present in the solution, when their concentration product overcomes the solubility product (Reaction 9).



Reaction 9

In order to evaluate the iron carbonate precipitation, a useful parameter is the system supersaturation (SS Equation 2) [34]. System supersaturation is the ratio of the product of [Fe<sup>2+</sup>] and [CO<sub>3</sub><sup>2-</sup>] and the solubility product K<sub>sp</sub>.

$$SS = \frac{[Fe^{2+}] \cdot [CO_3^{2-}]}{K_{sp}}$$

*Equation 2*

Supersaturation is a thermodynamic stability factor, nonetheless, multiple theories suggest a correlation with crystal growth rate [35].

However, *SS* is not sufficient to evaluate the precipitation of corrosion products. In fact, the metallic surface must support the corrosion product layer as its substrate. In order to account for the corrosion rate, a “scaling tendency” parameter (ST) is suggested (Equation 3). Scaling tendency is the ratio of crystal growth rate ( $R_{gr}$ ) and the corrosion rate (CR). The metal surface is covered with corrosion products whenever ST is higher than unity [36].

$$ST = \frac{R_{gr}}{CR}$$

*Equation 3*

Similar to any chemical reaction, the solubility products depend both on temperature and ionic strength.  $CO_2$  aqueous corrosion is found in a wide variety of industrial applications where more or less saline media are present so foreseeing the variation of  $K_{sp}$  with ion concentration is essential. Dealing with solubility product, Sun proposed a solubility product equation derived from literature data which considered temperature and ionic strength variation at the same time (Equation 4) [5].

In order to calculate the ionic strength, in most cases, the salt concentration can be approximated to sodium chloride concentration or other support electrolytes. A good example is a saltwater solution. In fact, NaCl concentration is so high that one of other species such as carbonates and bicarbonates is negligible.

$$\log K_{sp} = -59.3498 - 0.041377T_k - 2.1963T_k + 24.5724 \log_{10}(T_k) + 2.518 \cdot I^{0.5} - 0.657 \cdot I$$

*Equation 4 T Temperature, I ionic strength. [5]*

By analyzing the calculated values of  $pK_{sp}$  at different temperatures in Figure 5, it is observed that the values of solubility product monotonically increase. Therefore, the precipitation of iron carbonate scales is thermodynamically favored at a higher temperature. On the contrary, the solubility product is lower at higher ionic strength making iron carbonate formation hindered [5][37–39]. Therefore, rising the temperature promotes precipitation both according to thermodynamics and kinetics (Arrhenius law).

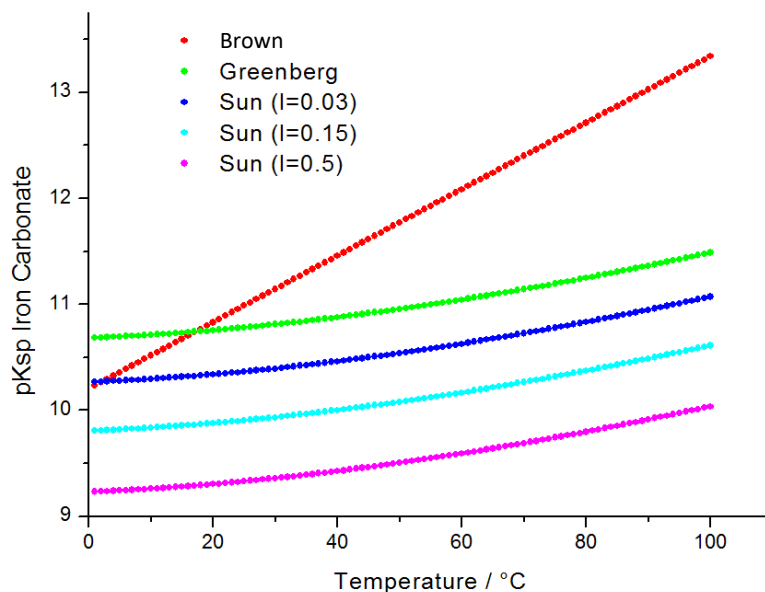


Figure 5 Solubility product of iron carbonate as a function of temperature. The curves were calculated using Brown Greenberg and Sun equation as a function of temperature [5] [37,38].

Concerning the temperature influence over precipitation, Nesic *et al.* proposed a numerical simulation of a carbon steel corroding surface in a CO<sub>2</sub> solution [34]. In the case illustrated, iron carbonate supersaturation is already attained at room temperature, however, at this temperature, no protective corrosion deposits are formed on the carbon steel surface. An appropriate scaling tendency factor, *i.e.*  $ST > 1$ , is attained only above 50°C. Similarly, Nesic and Lee reported in its simulation, a scaling tendency factor higher than one only at a temperature over 60°C [40]. Nevertheless, at 55°C, the formation of a porous iron carbonate film was predicted [40,41]. Experimental results on the temperature effect are in agreement with numerical simulations showing a decrease in the global corrosion rate and the formation of a compact iron carbonate layer at higher temperatures.

In order to evaluate the scales precipitation, accurate control of the pH and the partial CO<sub>2</sub> pressure is mandatory. In fact, the carbonate ion concentration, which is directly responsible for the scaling tendency of the system, is strongly linked through an equilibrium equation to the pH and the carbon dioxide pressure as seen in the “Solution chemistry” section.

In fact, a ten-fold increase in carbonate ion concentration can be achieved by raising pH from 6.8 to 7. Moreover, a lower pH increases the corrosion rate, thus decrementing the scaling tendency. Crystal nucleation and growth relevant for the corrosion process occur at the carbon steel/electrolyte interface. When possible, it is preferable to consider the parameters such as salt concentration and pH at the metal solution boundary which may be very different in respect to the bulk pH [42].

The mechanism of the scale nucleation has not been fully investigated yet, so little information is provided on the first stages of the precipitation of the corrosion product layer.

The composition of the scales deposit is complex since many compounds are present depending on the system condition. The mechanism of nucleation of siderite (FeCO<sub>3</sub>) and chukanovite (Fe<sub>2</sub>(OH)<sub>2</sub>CO<sub>3</sub>) was investigated by Ingham *et al.* through Small Angle X-ray Scattering (SAXS) and Wide Angle X-ray Scattering (WAXS) analysis [43]. The film nucleation and growth were obtained under potentiostatic anodic conditions at -500 mV vs saturated Ag/AgCl reference. A CO<sub>2</sub> saturated NaCl 0.5 M solution at pH and 80°C was used.

The current density measured at the interface shows a first period about an hour-long where current density remains stable. Subsequently the current density peaks. After the current density peak, its value drops to lower values than those present at the beginning of the test. When the current density started to increase, X-ray measurements identified the first signals of crystalline  $\text{FeCO}_3$ . However, no crystalline products were detected before although SAXS results show that the X-ray reflectivity plummeting. The intensity of  $\text{FeCO}_3$  continuously increases even when the measured corrosion density drops. The same behavior is observed for chukanovite. Furthermore, supersaturation values for iron carbonate colloid formation were extrapolated from SAXS experimental data at different concentrations of additional dissolved iron showing a critical value of 2.5 for the experimental conditions. As seen in the previous sections, the precipitation of iron carbonate comes from iron oxidation that produces  $\text{Fe}^{2+}$  ion. Because of the elevated measured currents density values due to working electrode polarization, supersaturation of iron carbonate at the solution is immediately attained. The authors advanced an hypothesis involving a gradual formation of an amorphous iron carbonate layer starting from small areas then extending to the entire metal surface. The amorphous iron carbonate layer has a density lower than iron thus the decrease in X-ray reflectivity could be explained by this process. However, the polarization may have produced a high value of saturation and, consequently a fast nucleation that does not allow iron carbonate to precipitate in a crystalline form but rather in an amorphous one.

After the formation of this amorphous iron carbonate layer, crystallization occurs at the interface between the rough metal surface and the amorphous layer. As a consequence of the siderite crystals nucleation, the amorphous film becomes thinner or even punctured at some points. This phenomenon could explain the increase in measured current after an initial incubation time. Besides crystal nucleation, crystal growth played a key role in the recorded current density peak. This is due to a decrease in pH because crystal growth liberates  $\text{H}^+$ .

Once the growth process forms a compact crystalline layer, the current density returns to a low value. Chukanovite ( $\text{Fe}_2(\text{OH})_2\text{CO}_3$ ), appearing later as a crystalline product on the metal surface, can be formed as a consequence of  $\text{Fe}^{2+}$  excess that reacts with the amorphous ferrous carbonate (AFC) giving a “hydrated iron excess gel” (amorphous  $\text{Fe}_2[\text{CO}_3][\text{OH}]_2$ ) “that could resemble amorphous chukanovite”.

#### **1.4.2 Composition of the corrosion product layer**

So far, the precipitation of iron carbonate was analyzed regardless of the phases that form the corrosion product layer. The nature of the iron carbonate precipitates is also relevant for understanding the scales protectiveness. Siderite ( $\text{FeCO}_3$ ) is the main phase detected as a result of corrosion in the  $\text{CO}_2$  aqueous solution, however other substances such as magnetite ( $\text{Fe}_3\text{O}_4$ ), chukanovite ( $\text{Fe}_2(\text{OH})_2\text{CO}_3$ ), goethite ( $\text{FeOOH}$ ) were identified as part of the corrosion product layer [44,45].

Tanupabrungsun reported that iron carbonate precipitates at lower temperatures ( $80^\circ\text{C}$ , Figure 6) and higher  $\text{CO}_2$  partial pressure in  $\text{CO}_2$  aqueous solution whereas magnetite is stable at higher temperature ( $200^\circ\text{C}$ ) [10].

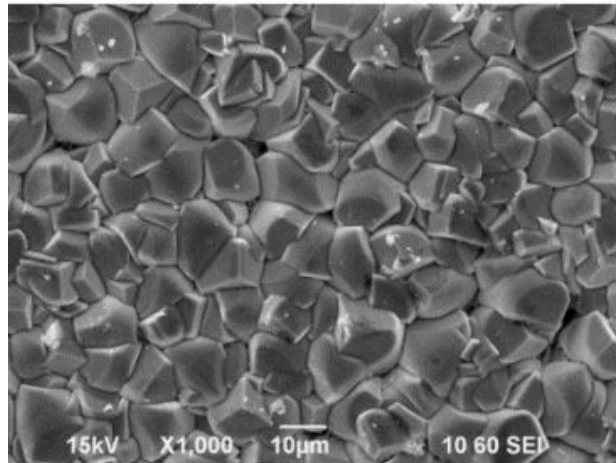


Figure 6 SEM images of the corrosion product layer at 80°C, 1 wt.% NaCl,  $c\text{CO}_2 = 0.030\text{ M}$  after 20 hours of exposure time [10].

Li *et al.* investigated iron corrosion deposits that precipitated in different conditions of pH and of the initial concentration of  $\text{Fe}^{2+}$  dissolved into the solution [46]. A previous study in 2005 noticed that adding  $\text{Fe}^{2+}$  does not affect the protectiveness of the deposit, only influencing the kinetic of carbonates precipitation [47]. The temperature was kept constant at 80°C, likewise NaCl concentration was fixed at wt. 1%. In those conditions and with a high pH (7.1 and 7.8), a compact layer of shaped crystals is formed, and the surface coverage is almost complete. Nonetheless, at pH 7.8, the size of the crystals is bigger than at pH 7.1 probably because of different nucleation kinetics. Descending towards more acidic values, *i.e.* 6.6 and 6, a platelets crystal morphology accompanies the shaped crystals seen before. Nevertheless, all the cases presented so far displays a continuous corrosion product layer covering the surface (Figure 7). Contrary, at pH 5.6, a continuous film is not observed although tiny amounts of shaped and platelets crystals form. Grazing Incidence X-Ray Diffraction (GIXRD) analysis was carried out showing that  $\text{FeCO}_3$  is the main phase covering the metal surface at both the highest pH investigated. No other phases were identified. The intermediate pH results display the coexistence of chukanovite ( $\text{Fe}_2[\text{CO}_3][\text{OH}]_2$ ) and iron carbonate. The same phases are observed at pH 5.6. The chukanovite phase was also observed by other authors who attributed to chukanovite the platelets type shape crystals of scale deposit [10] [48]. The other crystals with a classical rhombohedral shape were identified as siderite ( $\text{FeCO}_3$ ) crystals.

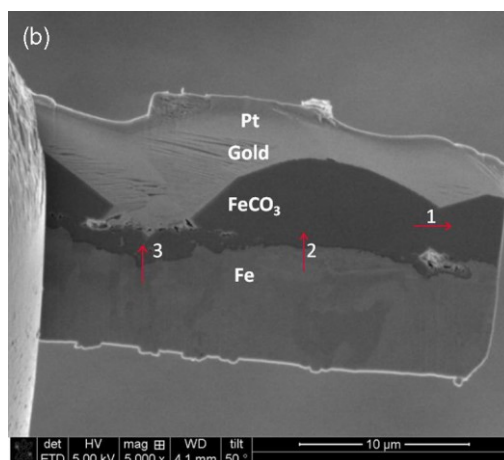


Figure 7 Continuous iron carbonate layer precipitated in 80°C, 0.53 bar (53 kPa)  $\text{CO}_2$ , 1 wt% NaCl, pH 7.1 aqueous solution [46].

Electrochemical measurements point out a greater protection ability for the scales at pH 7.1 and 7.8: indeed, a corrosion rate inferior to 0.01 mm/yr is reached by the samples after approximately 20 h. Intermediate pH (6.6 and 6) display corrosion rate values in the order of 0.1 mm/yr, however these rates are attained after 3-5 days. No significant corrosion protection is reached at pH 5.6.

Similar experiments were performed by Han *et al.*, however, the conditions were slightly different: the solution pH was set at 8 in order to accelerate the iron carbonate formation and no additional  $\text{Fe}^{2+}$  was provided to the system [49]. Samples cross-sections and GIXRD were compared before and after the pseudo-passive state. Pseudo-passivity is a condition of protection of the metal surface that is presented in the following sections. In addition to the usual iron carbonate corrosion product, after pseudo-passivation the precipitation of iron oxides occurred between the crystals of  $\text{FeCO}_3$ . Magnetite was identified as the oxide phase and its role as a passivation species in pseudo-passive conditions was proposed.

For experiments performed in  $\text{CO}_2$  saturated solutions at pH=6.6 and  $80^\circ\text{C}$ , de Motte *et al.* observed the formation of siderite crystals and chukanovite platelets on carbon steel surfaces [50].

De Motte *et al.* and Joshi *et al.* performed a study of the phases present in the corrosion products deposit and its relation with the corrosion rate [44,51]. Particularly Joshi *et al.* performed in situ XRD measurements on pure iron working electrodes immersed into a pH 6.8  $\text{CO}_2$  saturated solution at  $80^\circ\text{C}$ . In situ measurements are very powerful because they can follow the evolution of the precipitation behavior in real-time. Chukanovite and siderite were the only phases observed. The quantity of siderite and chukanovite crystals on the surface changes with immersion time (Figure 8). Furthermore, the average siderite crystal size evolves during the test: an increase of the dimension to a maximum followed by a decrease in the size of the crystals was observed. Trends in the corrosion rate, total surface coverage, relative coverage of chukanovite and siderite were analyzed.

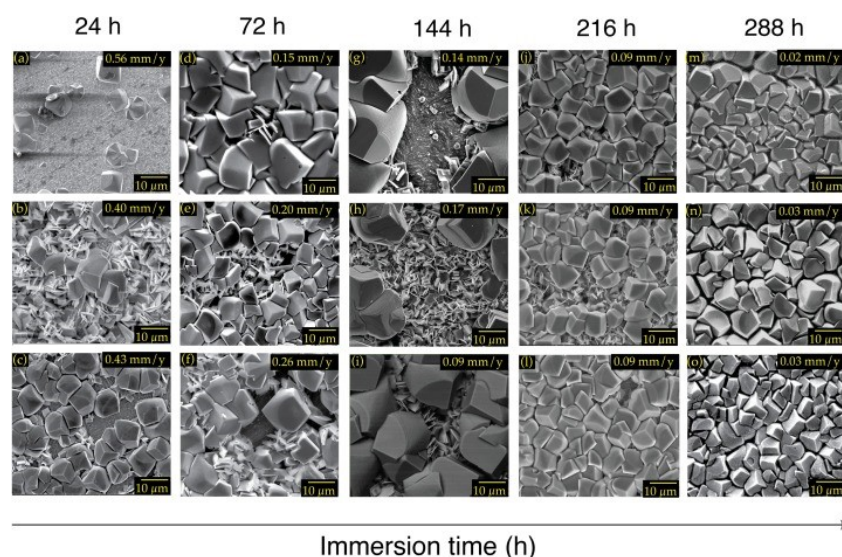


Figure 8 Corrosion product layer evolution as a function of exposure time in  $\text{CO}_2$ -saturated water ( $T = 80^\circ\text{C}$ ,  $\text{pH} = 6.80 \pm 0.02$ ) [44].

An initial stark decrease in the corrosion rate was associated with the increase in the coverage of the surface. The corrosion rates recorded when a mixed siderite-chukanovite covers the surface, are not as low as those obtained when siderite only is protecting the metal surface. Therefore, the authors suggested a limited protective role played by chukanovite. The SEM cross-section images underline

void spaces between the plate-like deposit and the metal surface especially at low immersion time. At longer exposure time, the gaps are filled with siderite while chukanovite gradually disappears. Thus, higher protection is to be expected when siderite crystals form a compact layer on the metal surface.

The formation of siderite was attributed to the initial surface conditions of the metal surface, particularly concerning two ratios: firstly between  $[\text{Fe}^{2+}]$  and  $[\text{OH}^-]$ , secondly between the carbonate and hydroxyl ion concentrations. Thereafter the dissolution of chukanovite as a result of undersaturation and metastability towards siderite was advanced as a hypothesis for its disappearance [10][52]. Indeed chukanovite is metastable with respect to siderite as proved in a previous study [52]. Furthermore, in the presence of oxygen chukanovite can be oxidized to goethite ( $\text{FeOOH}$ ) [45].

The role of chukanovite in protecting the surface points out that this compound is less effective and it could even hinder compact siderite layer precipitation and, consequently, the CPL corrosion protection. No oxide species are identified on the metal surface, even after pseudo-passivation (Pseudo-passivation 1.4.6 section), therefore the role of surface protection agent is attributed to siderite [50].

### 1.4.3 Mechanical properties of the corrosion product layer

Different studies addressed the issue of carbonate layer mechanical resistance [53–55]. The results show that the mechanical resistance of the carbonate layer is in the order of 10 MPa, or even greater because of experimental difficulties in separating the different adherence contributions of adhesive and metal iron carbonate interface. In any case, a film removal due to a single-phase fluid flow is observed. The removal of the film occurs after a crack initiation process. Values of shear stress are deemed insufficient concerning previous findings in order to explain film detachments. Therefore, a model involving local turbulences was proposed. The model involves an initial separation of the film from the substrate due to fatigue-like damage. As a consequence, cracking perpendicular to the flow direction occurs, leading to crack growth and to an ultimate film detachment. The corrosion products layer is also susceptible to be chemically dissolved because the environment becomes more acidic for example. The acidity of the solution that controls the degree of supersaturation, is indeed a major factor for the film dissolution kinetics and the film damage.

### 1.4.4 Influence of surface microstructure

Williams *et al.* investigated the influence of different carbon steel - solution interphase conditions on the formation of siderite-chukanovite scales [56]. A pH 6.8  $\text{CO}_2$  solution at 80°C was used and the NaCl concentration was 0.5 M. The samples were polarized at -500 mV vs Ag/AgCl and investigated with in situ XRD. Firstly, different alloy microstructures, *i.e.* martensitic and ferritic-perlitic carbon steel were tested. Ferrito-perlitic carbon steel shows a shorter current density induction time, *i.e.* a stationary current time frame before a current density peak, and a more rapid appearance of the crystalline corrosion products (siderite and chukanovite). Moreover, the in-situ fractal dimension measurements of Fe (110) planes display a higher surface roughness for the ferritio-perlitic structure due to the selective dissolution of small ferrite grains. Indeed, an increasing cementite relative phase volume is observed. These features are in agreement with the previous mechanism proposed by Ingham: a greater surface roughness, produced by selective corrosion, leads both to an increase of the concentration of  $\text{Fe}^{2+}$  and to the development of active sites for the nucleation of crystals [56]. Initial polishing with diverse surface roughness produces similar results. Siderite always crystallizes before chukanovite. Furthermore, SEM images display chukanovite crystals on top of siderite. Therefore, a mechanism involving chukanovite crystallization with siderite acting as nucleation sites is suggested.

Our work will use an API 5L X65 ferrite-perlitic steel. Ferrite interacts with the environment providing the iron ions needed for the precipitation of the scales. However, the role of cementite cannot be neglected.

Farelas *et al.* reported that the  $\text{Fe}_3\text{C}$  network that forms after ferrite dissolution, serves as a precipitation network of the iron carbonate corrosion product layer (CPL). Moreover, this effect increases the charge transfer resistance of the steel [57]. Scale precipitation was investigated with EIS and it was found that the precipitation of iron carbonates inside a cementite matrix results in enhanced corrosion resistance. This effect is due to the physical blocking of the cementite network which is a favorable location for proton reduction.

Kinsella *et al.* also used EIS in order to investigate the properties of the corrosion product layer and the related chemical reactions [58]. An high frequency time constant appears on the impedance diagram when the samples are exposed for a longer time to the  $\text{CO}_2$  aqueous solution. Both time constants have a circular shape on the Nyquist representation for all the pre-scale exposure times. Kinsella *et al.* associated the capacitive high-frequency time constant with a protective corrosion product layer, in particular protective scales that form at higher temperatures, pressures and exposure time [59]. No electrochemical mechanism was proposed for the different degrees of protection, nonetheless the higher protection effect was related to smaller crystal size whereas the same composition,  $\text{FeCO}_3$  and  $\text{Fe}_3\text{C}$ , was observed in all conditions.

Pessu *et al.* investigated the effect of temperature on pitting corrosion of carbon steel. Their results in a saturated  $\text{CO}_2$  environment at  $30^\circ\text{C}$  and atmospheric pressure revealed that in the early stages of the test, both the corrosion rates and OCP increase [60,61]. The TEM images show that ferrite is preferentially dissolved, leaving a rich cementite surface exposed to the corrosive solution. Cementite was proposed to enhance the corrosion rate as it acts as a preferential site for cathodic reduction. Furthermore, the galvanic coupling between the ferrite areas and the nobler  $\text{Fe}_3\text{C}$  produces suitable conditions for pitting.

Finally, it was observed that  $\text{FeCO}_3$  precipitates in the cementite rich layer, in agreement with Crolet *et al.* work [62]. The authors reported that the precipitation of iron carbonate scales could happen on top of the cementite layer. In particular, protective CPLs were only formed when the cementite network was not in contact with the steel surface. For other configurations, the cementite-rich surface could induce a mesa corrosion type attack of the carbon steel.

Anyway, an increase in the solution pH was measured in the first stages of corrosion at  $30^\circ\text{C}$ , possibly due to the cathodic reduction of  $\text{H}^+$ . This increase of pH rises the iron carbonate supersaturation, encouraging the  $\text{FeCO}_3$  precipitation [63]. At longer exposure time, the precipitation of the scales protects the surface, stabilizing the corrosion rate value. Acidification of the solution occurs at the ferrite - solution interface, whereas the precipitation of the carbonate occurs preferentially inside or on top of the cementite matrix. At higher temperature conditions, the study showed that the actual increase of the corrosion rates up to a peak value is greater than at lower temperatures. The ferrite selective dissolution and the consequent exposure of a cementite rich surface impacts more the corrosion rates at a higher temperature. At  $80^\circ\text{C}$ , TEM cross-section images confirm that traces of  $\text{FeCO}_3$  were present inside the  $\text{Fe}_3\text{C}$  network that can generate a self-healing mechanism against pits formation. Nonetheless, the cementite effect over the cathodic reactions and its eventual link with pitting corrosion need further investigations as no specific electrochemical tests have been performed to confirm the electrocatalytic properties of  $\text{Fe}_3\text{C}$ .

### 1.4.5 Tortuosity

The carbonate layer is not completely impermeable to the corrosive solution: permeable paths rather than pores still exist that allow the solution to be in contact with the metal. Nonetheless, considering the space randomness of crystal nucleation and growth, the formation of a straight path into the scales is unlikely. So dealing with tortuosity and its effects on electrical conductivity and diffusion coefficients is mandatory.

The resistivity of a porous material filled with an electrolyte can be higher up to two orders of magnitude concerning a simple electrolyte and can vary as a linear function of the porosity [64]. As a consequence, the corrosion product layer thickness calculated from film resistance can be overestimated if the tortuosity is not considered. The tortuosity affects the diffusion coefficients through the film, making them smaller than in the bulk solution. As Figure 9 shows, chemical species follow a non-linear path through the porous media. As a consequence, the flux of reactants would be slowed down in comparison with a straight path.

Finally, when certain conditions occur, simultaneously the electrical and diffusion tortuosity coincide. Specifically, no conduction in the solid phase, no reaction between porous solid and diffusing species and no electrokinetic drag or no anion exclusion are the requirements to be met. In the case of iron carbonate scales, those requirements are satisfied [65,66].



Figure 9 Scheme of tortuosity in a porous media. the blue line describes a viable path for a chemical species from point A to B.

### 1.4.6 Pseudo-passivation

Pseudo-passivation is the result of the precipitation of the scales at the surface. It occurs spontaneously in certain environmental conditions that are explained in the following paragraphs. When the corrosion product scales reach the pseudo-passive state, the metal is particularly protected with respect to uniform corrosion. The values of the corrosion rates are very low. This state can be identified with classical electrochemical techniques as the open circuit potential rises to more anodic values when pseudo-passivation occurs.

The electrochemical features of a pseudo passive system were investigated by Han *et al.* in several system conditions [67,68]. The study highlighted that in a CO<sub>2</sub> saturated solution at 80°C and atmospheric pressure, the potentiodynamic polarization curves at high pH (7 - 8) show a transition

similar to stainless steel. Moreover, the OCP of the working electrode was measured during the exposure to an aqueous solution saturated by carbon dioxide at 80 °C, total atmospheric pressure and a pH between 7 and 8. All the tests presented a S-shaped potential transition towards more anodic potential. However, the test showed this transition occurs earlier, the higher the pH of the solution was.

The same results were obtained at different temperatures keeping the rest of the solution conditions constant. The OCP transition was observed earlier for higher temperatures. The same concept was applied using different CO<sub>2</sub> partial pressure and a quicker transition was observed for higher carbon dioxide pressures.

The observed potential transition along with the potentiodynamic polarization curves suggests a sort of passivation of the surface due to the precipitation of the corrosion product layer. In order to prove that a higher corrosion protectiveness was attained, LPR measurements were performed. They highlighted a significant increase in resistance polarization after passivation. However, reducing the solution pH immediately lead to a drop of the polarization resistance pointing out a loss in film protectiveness.

The protective properties of the film are reversible and strongly linked with the chemistry of the solution. This particular situation where the scales effectively protect the surface was dubbed pseudo-passivation.

Another study from Han *et al.* deepened the investigation of this passivation, focusing specifically on the composition and morphology of the corrosion product layer [69]. SEM, TEM and GXRD were the main techniques for characterizing the scales. GXRD measurements determined that siderite (iron carbonate) is the main component of the scales both before and after pseudo-passivation. Furthermore, traces of magnetite were detected only in the case of a pseudo-passive surface. TEM-EDS directional analysis confirms the presence of an iron oxide placed right on top of the metal surface. For these reasons, magnetite was deemed responsible for the formation of a pseudo-passive layer. The precipitation of magnetite was justified by the high surface pH present underneath the iron carbonate scale because of proton reduction as a consequence of the corrosion process. In that situation, the carbonate layer acts as a diffusion barrier preventing bulk H<sup>+</sup> to reach the metal surface. Although the scales characterization shows magnetite at the top of the surface, no Fe<sub>3</sub>O<sub>4</sub> continuous film was observed separating the metal surface from the corrosive solution.

In another study, the passivating role of magnetite was reaffirmed when decreasing the pH led to a drop of the polarization resistance even if the solution remained over-saturated with respect to iron carbonate [49]. Siderite was not deemed responsible for pseudo-passivation. Even in this case, although magnetite was detected, a continuous film of magnetite was not found. The fundamental role of the iron carbonates layer was proven by comparing corrosion rates of the same steel in a deaerated NaOH and CO<sub>2</sub> saturated solution at different pH. Electrochemical tests involved both passivation in spontaneous conditions and with potentiodynamic polarization. Regarding the potentiodynamic tests, the passivation conditions were reached for all the potential scan speeds in CO<sub>2</sub> saturated solution. However, lower passivation current density values were obtained for lower scan rates due to the longer time necessary for the growth of the corrosion product layer. On the contrary, a NaOH solution provided only suitable conditions for passivation in the low potential scan speed case. Similarly, the metal passivates spontaneously in different conditions when CO<sub>2</sub> saturated solutions were used whereas no spontaneous passivation was observed in deaerated NaOH solution even when an anodic polarization was applied. Spontaneous passivation in CO<sub>2</sub> saturated environment follows coherently the conditions in which a carbonate layer develops more easily, *i.e.* higher pH and temperature. A test

of re-acidification of the corrosive solution was performed after pseudo-passivation going from pH 7.8 to 5.4. The system lost the polarization resistance typical of pseudo-passivation even if  $\text{FeCO}_3$  saturation was maintained. Although the presence of  $\text{CO}_2$  significantly affects the formation of pseudo-passive scales, the latter result points out that siderite is not responsible for pseudo-passivation because pseudo-passivation is lost even in iron carbonate saturation conditions. The TEM images showed a small layer of magnetite between the metal and iron carbonate. Magnetite was considered responsible for pseudo-passivation even though there was no continuous film completely covering the metal substrate. In a previous study pseudo-passive behavior was attributed to the formation of a  $\text{Fe}(\text{OH})_2$  passive layer underneath the iron carbonate layer. This effect was rationalized considering an increase of surface pH [67].

Another study related to the pseudo-passivation of carbon steel was done by Li *et al* [46]. The study used LPR and OCP to study the evolution of the scales in a  $\text{CO}_2$  saturated solution at different pH. The results showed that a stark decrease of the corrosion rate was observed at the same moment of the pseudo-passivation transition. The solutions at higher pH developed protective scales earlier in agreement with Han *et al.* [67].

SEM images showed that more compact siderite scales with an inferior crystal size develop at higher pH (7.8) whereas at lower pH (6) looser scales precipitated. In the latter case chukanovite co-precipitated with siderite. The film was compact and well adherent to the metal substrate with a 2-3  $\mu\text{m}$  thickness. The corrosion product layer is significantly more thick in this case than in stainless steel where the film thickness is nanometric [70].

Different studies remarked a particularly protected surface condition that was called pseudo-passivation. The role of  $\text{CO}_2$  and its related species is essential in forming pseudo-passivation. The pseudo-passive transition was well characterized from an electrochemical perspective namely a significant OCP S-shaped rise and a simultaneous decrease of the corrosion rate were observed. Nevertheless, no definitive proof was given that could explain why the surface becomes pseudo-passive and the related mechanism. Although magnetite was found in the pseudo-passive scales just small traces were identified and in no circumstance a continuous film formed. Therefore, identifying magnetite as the main compound to cause a pseudo-passive layer on carbon steels, seems a bold affirmation. Further investigations are required to elucidate pseudo-passivation origin and mechanism.

## 1.5 Contaminants effects

So far, the precipitation of the scales and the corrosion process in a pure  $\text{CO}_2$  aqueous solution were analyzed. However, the solution chemistry in the industrial application is rather complex and the effect of other chemicals has to be investigated for evaluating the possible risks that may arise. The following sections deal with the effect of the three most common contaminants chlorides,  $\text{Ca}^{2+}$  and  $\text{O}_2$ .

### 1.5.1 Influence of chloride ions

Chloride ions have an important impact on the corrosion rate in a carbon dioxide aqueous environment. There is quite a consensus on the effect that chlorides have on the corrosion rate. For an increased content of chlorides, the first increase of corrosion is observed followed by a decrease at higher concentration in chloride. Nevertheless, the role of  $\text{Cl}^-$  on the pitting mechanisms under a corrosion product layer (CPL) and its breakdown process mechanism, still needs to be further clarified.

The effect of different chloride concentrations over the CO<sub>2</sub> corrosion of N80 carbon steel was tested by Liu *et al.* [71]. The measured corrosion rates firstly increase up to a maximum with increasing the chlorides concentration and then decrease for higher dissolved chlorides content in the corrosive solution. Furthermore, hand top-view SEM images show the evolution of the corrosion product layer with increasing chlorides concentration: from a compact layer formed by well-shaped crystals, it transforms into bulky, loosely packed crystals that do not effectively cover the carbon steel surface. Additionally, cross-sectional SEM images display that the corrosion product layer was formed by an inner compact layer and an outer layer composed of regular crystals. With increasing Cl<sup>-</sup> concentration, the boundary between these two layers becomes less evident and the outer layer crystals have less regular shapes. At the highest tested Cl<sup>-</sup> concentrations, *i.e.* 75 g/L, the CPL is thin and barely visible.

Corrosion current densities obtained from potentiodynamic polarization measurements follows the trend of the mass-loss measurements with a further increase of corrosion current density up to a maximum and then a reduction at higher chlorides content. XRD analysis is in agreement with the results of Ingham *et al.* that found siderite only in the CPL of anodically polarized carbon steel specimens immersed in saturated brine, whereas chukanovite Fe<sub>2</sub>(OH)<sub>2</sub>CO<sub>3</sub> was present in the same conditions with the addition of MgCl<sub>2</sub> [72]. Fe<sub>2</sub>(OH)<sub>2</sub>CO<sub>3</sub> was reported as well by Joshi *et al.* in the first stages of the corrosion process in a CO<sub>2</sub> saturated solution at pH ≈ 4 in the absence of other salts [51].

The corrosion properties and pitting susceptibility of carbon steel were investigated in several corrosive solutions that simulated the sour and sweet operative conditions of Canadian oil pipelines by Papavinasam *et al.* [73]. Electrochemical noise and potentiodynamic polarization techniques were used to investigate this complex system that involved the co-presence of several corrosive gases such as CO<sub>2</sub> and H<sub>2</sub>S. Higher values of pitting index and corrosion current densities were found when the chloride concentration is higher. The authors observed that thinner corrosion product layers were formed at higher chloride concentration and thus they attributed a higher risk of pitting corrosion for greater dissolved Cl<sup>-</sup> concentration.

Fang *et al.* investigated the effect of flow and the increase of chlorides concentration in a carbon dioxide saturated water solution on the corrosion of carbon steel [74]. The results show a diminution of the uniform corrosion rate with increasing NaCl concentration (which is an unexpected result) whereas the corrosion rate increases with a higher rotation of the electrode. Nevertheless, the effect of flow conditions becomes less important for higher chloride concentrations. The potentiodynamic polarization indicates that the dissolved NaCl slows down both the anodic and the cathodic reactions and this behavior was attributed to the change from a mixed charge transfer/limiting current control to a charge transfer control. Finally, no pitting was observed on the metal surface in any of the tested conditions.

A double electrochemical role is attributed to Cl<sup>-</sup>. It interacts directly with the iron surface accelerating the anodic reaction while it lowers the CO<sub>2</sub> solubility leading to a decrease of the cathodic reduction rates [75]. Nonetheless, the conclusion related to the anodic reaction is not supported by transient techniques, as the use of steady-state techniques is not sufficient to ascertain a reaction mechanism. The lack of corrosion product precipitation at higher chlorides concentration was attributed to the accumulation of oxygen vacancies at the metal/film interface that stops the growth of the CPL while its dissolution still occurs at the solution/film interface.

Eliyian *et al.* [76] pointed out that the experimental conditions of Papavinasam *et al.* [73] and Fang *et al.* [74] namely complex corrosive solution chemistry and the gap between chlorides concentration tested respectively are not ideal in order to isolate the chlorides contribution on the corrosion process. In their study, the polarization curves at progressive chlorides concentration show a monotonous decrease of corrosion potential whereas the corrosion current density increases up to a peak at lower chlorides concentrations and then it plateaus at lower corrosion rates for greater concentration values. Those results were obtained for both tested temperatures namely 20°C and 80°C. The authors claimed that the corrosion rate decline after the peak value is due to the slower kinetics of the cathodic reactions. In fact, the limiting current plateau during the cathodic polarizations is lower in the high [Cl<sup>-</sup>] case. Electrochemical impedance results show that chlorides do not impact the overall corrosion process mechanism as the shape of the impedance diagrams on Nyquist plot does not change. Furthermore, impedance measurements performed at high cathodic overpotential display that these anions do not interfere with the cathodic reduction of protons. The slower cathodic kinetics have to be linked to other physicochemical interactions between the Cl<sup>-</sup> ions and the corrosive environment.

In another study, CO<sub>2</sub> corrosion of carbon steel at different chlorides concentrations was tested and blank tests were made with Cl<sup>-</sup> ions only without CO<sub>2</sub> [77]. The mass loss measurements show a rise in the corrosion rate for increasing chlorides concentration up to threshold concentration upon which the corrosion rate started to decrease. The impedance measurements do not show variations between the chlorides of the solutions and the electrochemically inert perchlorate ion. According to these findings, Cl<sup>-</sup> does not impact the electrochemical mechanism of the corrosion process. This last result is in contrast with the anodic iron dissolution mechanism proposed by Liu *et al.* that involved a direct interaction between the steel surface and Cl<sup>-</sup> ion leading to an adsorbed hydroxyl-chloride anion [71]. According to these authors, competitive adsorption occurs between Cl<sup>-</sup> and HCO<sub>3</sub><sup>-</sup> [78].

Furthermore, injecting chlorides in the testing solution results in a reduction of the corrosion scales surface coverage. In fact, considering the surface coverage variation at different chloride concentrations, the trend is the opposite of the corrosion rate whereas the crystal size follows the same tendency of corrosion rate. Cross-sectional SEM observations of the samples show that the corrosion product layer is more porous in the presence of chlorides ions, highlighting the formation of less protective scales. Moreover, top-view SEM micrographs reveal an increasing number of CPL defects when increasing the Cl<sup>-</sup> concentration [77]. Furthermore, the EDS investigation of the corrosion products in the surroundings of the film defects reveals traces of chlorides pointing out the possible involvement of Cl<sup>-</sup> in the formation of the film defects. Profilometry measurements of the metal surface after the removal of the corrosion product layer show more corrosion pits in the solutions containing chlorides than in those simply saturated with carbon dioxide. Pessu *et al.* [62] claimed that the intervention of the chloride ions on the corrosion product layer is related to the decrease of carbon dioxide solubility inside the solution. This decrease in the carbon dioxide concentration would result in a slower iron carbonate formation because it does not react with Fe(OH)<sub>2</sub> thus leading to a less effective diffusion barrier and protection when chlorides are dissolved in the solution. This results in the localization of the anodic areas over the metal surface that initiates pitting corrosion.

A final proposed mechanism involves oxygen vacancies that are promoted by a higher chlorine activity. Accumulation of those vacancies at the interface between the corrosion product film and the metallic surface leads to localized film breakdowns and thus pits formation. This mechanism was also proposed by Liu *et al.* to explain the corrosion product layer breakdown at increasing Cl<sup>-</sup> concentration [71].

### 1.5.2 Influence of Calcium cations

Iron carbonate is not the only precipitate that can be formed at the metal surface. Joshi *et al.* observed the co-precipitation of siderite and chukanovite that is a hydroxycarbonate. The presence of iron oxides was detected below the siderite scales [75] [69]. Nonetheless, carbonate anions form many insoluble compounds in the presence of other cations such as  $\text{Ca}^{2+}$ . In fact, calcium carbonate is an isostructural form of the siderite that can readily incorporate  $\text{Ca}^{2+}$  ions [79] in its structure. Similarly,  $\text{Fe}^{2+}$  ions can be incorporated into the crystal structure of calcium carbonate. An average calcium concentration ranges between 2.5 and 26 g/L in oilfield waters [80].

Alsaiani *et al.* investigated the interaction between the  $\text{Fe}^{2+}$  and the calcium carbonate precipitation in a batch reactor [81]. The results showed that  $\text{Ca}^{2+}$  enhances the siderite ( $\text{FeCO}_3$ ) solubility whereas  $\text{Fe}^{2+}$  does not affect the calcium carbonate solubility. The experiment revealed that the presence of  $\text{Ca}^{2+}$  attenuates the temperature effect over  $\text{FeCO}_3$  precipitation *i.e.* siderite precipitated more slowly at 65°C when  $\text{Ca}^{2+}$  ions were inside the solution. Finally, four precipitation interactions between  $\text{CaCO}_3$  and  $\text{FeCO}_3$  were identified. Particularly, one of them displays the inhibition of the  $\text{FeCO}_3$  (siderite) nucleation and growth at the beginning of the  $\text{CaCO}_3$  (aragonite) precipitation. In a later study, calcium carbonate precipitation was found faster than iron carbonate one despite a higher calcium carbonate solubility. Higher calcium to iron ratio in the solid than in the solution was found [82]. Finally, the formation of a mixed iron-calcium carbonate  $\text{Fe}_x\text{Ca}_{(1-x)}\text{CO}_3$  was reported and a method to predict the calcium content in the mixed precipitate using as inputs the concentration values of  $\text{Ca}^{2+}$  and  $\text{Fe}^{2+}$  in the solution was developed [83].

Later, the impact of calcium ions on the precipitation of iron carbonates that form the corrosion product layer on the metal surface was highlighted by N. Esmaeely *et al.* [84]. The corrosion tests show that for low  $\text{Ca}^{2+}$  concentrations such as 10 and 100 ppm, the measured corrosion rate is similar to that of the blank solution whereas, for higher  $\text{Ca}^{2+}$  concentrations ( $10^3$  and  $10^4$  ppm), the corrosion rate is higher. The corrosion rate for the lower concentration decreases with exposure time while it remains constant for  $10^3$  and  $10^4$  ppm. pH measurements highlighted that the presence of calcium ions at higher concentrations corresponds to a lower pH of the solution. According to the authors, the pH shift towards lower values is due to the precipitation reaction of calcium carbonate that produces free  $\text{H}^+$ . As reported in reaction 2, a pH change can have a dramatic impact on the homogeneous reactions equilibria and saturation values of the corrosion products leading to different outcomes for the CPL protectiveness.

The measurements of the dissolved  $\text{Fe}^{2+}$  and  $\text{Ca}^{2+}$  ions in correlation with the related carbonate saturation show that, after the initial precipitation of iron and calcium carbonates, the iron carbonate precipitation rate becomes slower due to the lack of available  $\text{Fe}^{2+}$ . Iron carbonate precipitates at the surface although its saturation rate is significantly lower than the one of calcium carbonate, pointing out a faster kinetic for the  $\text{FeCO}_3$  precipitation [84]. The minimum value of the  $\text{FeCO}_3$  saturation is followed by an increase of the parameter due to corrosion producing free  $\text{Fe}^{2+}$  ions in the solution leading to new growth of the iron carbonate saturation rate.

Finally, XRD analysis on the CPL shows that a mixed iron-calcium carbonate forms in the higher dissolved  $\text{Ca}^{2+}$  concentration in association with higher corrosion rates underlining that  $\text{CaCO}_3$  and the mixed carbonate are less protective than  $\text{FeCO}_3$ . The molar fraction of calcium is not equal along the CPL cross-section but, for the higher values of dissolved  $\text{Ca}^{2+}$ , it is richer in calcium close to the surface. For lower calcium concentration both the XRD analysis and the SEM top-view images confirm that dissolved  $\text{Ca}^{2+}$  does not affect the morphology and crystallographic structure of the corrosion product layer. The increase of calcium molar fraction in the CPL for higher dissolved  $\text{Ca}^{2+}$

concentration agrees with the results of Ding *et al.* that measure the molar fraction of the mixed iron-calcium carbonate using XRD analysis. The results confirm that the presence of calcium ions in the solution makes the corrosion product layer less protective [85].

The effect of the calcium ions on the protectiveness in the corrosion product layer was also investigated by Esmaeely *et al.* [86]. Different flow conditions were tested keeping the same concentration of  $10^4$  ppm of calcium ions. The findings showed that the corrosion rate in the presence of dissolved  $\text{Ca}^{2+}$  is lower even in flow conditions, contrary to what was found in the previously mentioned studies. As a result of the precipitation of iron carbonate, the solution pH was stabilized to a higher value than without  $\text{Ca}^{2+}$ . SEM micrographs display morphologies that are different from the siderite crystals: probably the CPL should be a mixed iron-calcium carbonate film. Through the analysis of the XRD diffraction {104} interplanar d spacing, a calculation method for the  $\text{Ca}^{2+}$  fraction of a mixed iron-calcium carbonate was developed.

Pitting corrosion occurred during the test in stagnant and for 300 rpm conditions in the presence of  $\text{Ca}^{2+}$ . Nonetheless, it was not possible to determine if the above-mentioned pits were filled by the corrosion products and thus stopped or kept propagating. The authors claimed that  $\text{Ca}^{2+}$  ions are responsible for pits formations rather than the  $\text{Cl}^-$  ion because they did not observe any pits in the NaCl only solutions whereas they did when  $\text{Ca}^{2+}$  ions were added. However, the range of experimental conditions such as temperature and concentration of  $\text{Cl}^-$  and  $\text{Ca}^{2+}$  ions are not wide enough to exclude the role of  $\text{Cl}^-$  in pit formation for iron carbonate scales.

The scales formation in simulated produced water (SPW) was investigated at supercritical  $\text{CO}_2$  pressure on carbon steel [87]. Since the corrosive solution used is an oil well simulated produced water (SPW), dissolved  $\text{Ca}^{2+}$  is guaranteed by the dissolution of  $\text{CaCl}_2$ . The presence of both  $\text{Cl}^-$  and  $\text{Ca}^{2+}$  makes it hard to distinguish the role of each single chemical species on the pitting initiation and propagation or overall pitting risk of the CPL in comparison with a pure saturated  $\text{CO}_2$  water solution. Anyway, XPS and XRD analysis confirmed the presence of an iron-calcium carbonate  $\text{Fe}_x\text{Ca}_{(1-x)}\text{CO}_3$ , which is the main phase of the scales.  $\alpha\text{-FeOOH}$  is also detected. The composition of the corrosion product layer is in agreement with the observations of Wu *et al.* that performed corrosion tests with the same solution at a lower pressure (0.5 MPa) [88].

The influence of calcium ions under supercritical  $\text{CO}_2$  pressures in the aqueous phase was also investigated by Tavares *et al.* [89]. To provide the desired calcium contamination, an appropriate quantity of solid  $\text{CaCO}_3$  was added to the autoclave. In supercritical conditions and for all the tested exposure times, the addition of  $\text{CaCO}_3$  results in a lower corrosion rate. For both the blank and the  $\text{CaCO}_3$ -containing solutions, the corrosion rate decreases over time because of the precipitation of a corrosion product layer. Diffusion barrier properties were attributed to the precipitated film, even if SEM observations reveal that the scales that precipitate with the addition of calcium carbonate in the solution are thinner and more porous. Combined XRD and EDS analysis on the samples reveal that in the presence of  $\text{CaCO}_3$ , the corrosion product layer is a mixed calcium-iron-carbonate layer. Some precipitation reactions were proposed involving co-precipitation of iron with  $\text{Ca}^{2+}$  and carbonate-bicarbonate ion or iron with calcium bicarbonate. Finally, the scaled samples were tested using electrochemical measurements as well. The potentiodynamic polarization reveals a passive domain both with and without  $\text{CaCO}_3$  but in the latter cases, pits were observed beyond the “trans-passive” potential.

Shamsa *et al.* investigated the impact of  $\text{Ca}^{2+}$  ions over the precipitation of the corrosion product layer and the corrosion protective properties of the film [90]. Experiments were performed in an autoclave

at 80°C and 150°C. Two corrosive solutions were tested with and without dissolved  $\text{Ca}^{2+}$ . The samples were analyzed after different exposure times in order to follow the evolution of the corrosion scales during testing. The corrosion product scales that form at higher temperatures provide superior protection from corrosion although the porosity of the layers is comparable for both temperatures. The precipitation of the scales at 150°C occurs during the first 6 hours of exposure in the corrosive environment. Considering the corrosive solution with dissolved  $\text{Ca}^{2+}$  at 80°C, the scales that precipitate are less protective after four days of testing although a higher CPL mass was measured. Faster precipitation of the CPL in the first 48 hours of the experiment was detected without  $\text{Ca}^{2+}$ . The relationship between the mass loss and the corrosion product mass after two days shows that the corrosion film is less adherent at the metal surface with the addition of  $\text{Ca}^{2+}$  ions in the solution due to greater solubility of  $\text{Fe}^{2+}$  with  $\text{Ca}^{2+}$  contamination as previously reported by Alsaïari *et al.* [81]. At 150°C the addition of dissolved  $\text{Ca}^{2+}$  ions results in similar corrosion rates to in the NaCl-only solution after four days of exposure to the corrosive environment. However, this similar protectiveness of the deposit was attained with a smaller corrosion film mass. The higher protectiveness obtained at higher temperatures is also observed in the profilometry analysis for the investigation of the localized corrosion beneath the CPL. The results show that at 150°C the uniform corrosion rate reaches low values with and without  $\text{Ca}^{2+}$  in the solution and that the pit growth is constant throughout the test. On the contrary, at 80°C a higher uniform corrosion penetration was observed for the case with  $\text{Ca}^{2+}$  ions whereas the pit penetration depth is similar for the two conditions. The authors claimed that  $\text{Ca}^{2+}$  ions at lower temperatures expose the surface to a higher risk of pitting corrosion as the higher rate of uniform corrosion makes the pit penetration to be underestimated. Higher temperature conditions present the same risk of pitting corrosion regardless of the presence of the  $\text{Ca}^{2+}$  ions, but the protective scales formed seem to prevent the pitting propagation.

SEM micrographs of the corrosion product layer formed at 80°C after 96 hours of exposure show that the film is more porous with the addition of  $\text{Ca}^{2+}$ . A mixture of  $\text{FeCO}_3$  and iron-calcium carbonate ( $\text{Fe}_x\text{Ca}_y\text{CO}_3$ ) forms the CPL. The two components co-precipitated together on top of the metal surface whereas at a higher temperature, after the same exposure time, this mixed-phase was embedded inside the  $\text{FeCO}_3$  film. XRD analysis allowed to determine the evolution of the content of  $\text{Ca}^{2+}$  ions inside the corrosion product layer. The results show that the calcium fraction inside the film decreases overtime at 80°C, whereas the film precipitated at 150°C has a constant concentration of calcium throughout the all test duration.

### 1.5.3 Effect of oxygen

Few studies have reported the effect of oxygen in a  $\text{CO}_2$  corroding system. Xiang *et al.* investigated the effect of a complex  $\text{CO}_2/\text{SO}_2/\text{O}_2/\text{H}_2\text{O}$  mixture in supercritical conditions, on the corrosion of X70 carbon steel [91]. In this case, oxygen was considered as an oxidant for sulfites leading to the formation of hydrated sulfates inside the corrosion product film.

Some tests were performed in water-saturated supercritical  $\text{CO}_2$  conditions with the addition of traces of oxygen (2000 ppmv), hydrogen sulfide (2000 ppmv) and both the contaminants at the same time [92]. The results show similar and low values of the corrosion rates for pure  $\text{CO}_2$  and mixed  $\text{CO}_2\text{-O}_2$  systems. One order of magnitude higher values was obtained for the  $\text{CO}_2\text{-H}_2\text{S}$  system whereas when all the contaminants were present at the same time, a hundred-time greater corrosion rate values were observed. Observation of the samples after removal of the corrosion product layer was performed. In the pure  $\text{CO}_2$  with oxygen trace cases in supercritical conditions, localized corrosion was observed whereas the other experiments with oxygen and hydrogen sulfide contaminations, displayed generalized uniform corrosion. Concerning the corrosion product layer, a thin grey film was present with  $\text{CO}_2$  and with  $\text{H}_2\text{S}$  contamination. A layer of rust was present when adding oxygen. In the last

situation, *i.e.* CO<sub>2</sub>-H<sub>2</sub>S-O<sub>2</sub>, the macroscopic film was present with a loose outer part and an inner denser layer. This structure of the CPL points out an evolution of the corrosion product film precipitation that cannot be elucidated by observing one sample only at the end of the test. SEM images with EDS analysis revealed that small amounts of corrosion products precipitated with CO<sub>2</sub> only, whereas in the case of O<sub>2</sub> worm-like structures were present and they were attributed to Fe<sub>2</sub>O<sub>3</sub> because of the iron/oxygen ratio. XRD analysis shows complex chemistry for the precipitates when all the gases were present. A variety of corrosion products such as FeCO<sub>3</sub>, S<sub>8</sub>, FeS, FeOOH and Fe<sub>2</sub>O<sub>3</sub> was identified. As EDS analysis only shows oxides on the surface, the authors proposed that oxygen inhibits the iron carbonate precipitation. The corrosion product layer precipitation was therefore attributed to the iron oxidation products Fe<sub>2</sub>O<sub>3</sub> and FeOOH.

In another study, the effect of oxygen on mild steel samples was investigated [93]. The potentiodynamic polarization results show that the cathodic reactions of the corrosion process are dominated by charge transfer with an oxygen concentration inferior to 100 ppb whereas for higher concentrations (1 ppm) the mechanism is a mixed control one. Moreover, at 3 ppm of O<sub>2</sub> after 24 hours, pitting initiation occurs but propagation does not take place. The observed pits came from the ferric oxide layer that precipitated on the steel surface. Its thickness depends on the oxygen concentration and finally, no iron carbonate precipitation occurs due to the low pH value (5) at which the test was carried out.

Oxygen effect on sweet corrosion in enhanced oil recovery situations was studied by Rosli *et al.* [94]. They investigated the impact that the addition of 1 ppm of dissolved oxygen has on carbon steel. The oxygen contamination was added at different exposure times in a water solution at 80°C and pH 6.6. The results reveal that, with the introduction of oxygen, the OCP increases by 200 mV after 48 hours. Furthermore, the corrosion rates measured with O<sub>2</sub> are slightly higher than those without oxygen. The corrosion product layer displays some clusters, mounds and craters that are considered as the porous corrosion products on top of a pit whose outer layer is composed of iron oxides. XRD analysis reflected the SEM observation, identifying hematite and magnetite inside the CPL. The addition of oxygen from the start of the test, resulted in postponing the formation of a protective corrosion product layer as reflected by the measured corrosion rates and the concomitant OCP rise. In the CPL, iron oxides hindered the coverage of FeCO<sub>3</sub> because of competitive precipitation.

The effect of oxygen contamination on the composition of carbonates corrosion product layer through in situ XRD work was studied by Ingham *et al.* [95]. The experimental setup consisted of a classical three electrodes electrochemical cell with an API J55 carbon steel as the working electrode. The electrolyte was a 0.5 mol/kg NaCl CO<sub>2</sub> saturated solution. 20g/kg of 2 mol/kg NaOH solution was added to attain a calculated pH of 6.8. The operating temperature was set to 80°C as other tests previously discussed for the sake of optimal scaling conditions. Oxygen was not directly introduced into the electrolyte but it diffused through the tubes of silicone rubber that connected the electrochemical cell with the solution reservoir. Therefore, the oxygen concentration was a function of the solution flow rate into the tubes. In any case, there was no monitoring of the dissolved oxygen concentration, which does not guarantee constant chemical conditions throughout the test.

The working electrode was polarized at different anodic potentials to accelerate the corrosion product layer formation. Furthermore, the oxygen concentration into the cell was changed by regulation of the solution flow thanks to a peristaltic pump. The more the solution flux the less the oxygen was dissolved into the electrolyte.

Although anodic polarization of the working electrode speeds up scaling, it may have influenced the kinetics and thermodynamic conditions of the precipitated compounds altering their saturation in the solution.

The addition of oxygen causes the crystallization of green rust immediately after the polarization potential is applied. Green rust composition was identified as  $\text{Fe}_6(\text{OH})_{12}\text{CO}_3$  unlike the aforementioned mechanism suggested by Ingham where amorphous iron carbonate had first precipitated and then precipitation of crystallized siderite occurred. Crystalline  $\text{Fe}_6(\text{OH})_{12}\text{CO}_3$  appeared also in the first stages *i.e.* dissolution phase of the corrosion process [43].

The volume of the green rust that precipitated is dependent only on the solution flow, *i.e.* the oxygen concentration, and not on the applied anodic potential. This phase does not cause a diminution of the current density peak value recorded whereas a current density fall is observed when siderite crystals form on the metal surface. The chukanovite precipitation rate and amount are both dependent on the flow rate and the electrode potential; particularly its amount grows at a lower flow rate, *i.e.* higher oxygen concentration, and its rate has higher values for a more negative electrode potential. Chukanovite precipitation is faster, with respect to siderite, for higher flow rates at the same potentials. The accelerated precipitation advances the chukanovite appearance before the siderite one. Because the  $\text{Fe}_6(\text{OH})_{12}\text{CO}_3$  kinetic is only dependent on  $\text{O}_2$  concentration and does not correlate with the dissolution current density peak, its formation as a direct dissolution product of iron is discarded, therefore the green rust has no direct effect on the precipitation of other iron carbonates. Nonetheless, its formation was explained by the oxidation of dissolved iron (II) present in the solution. It was observed that oxygen does not affect the siderite precipitation.

Regarding the chukanovite precipitation, the green rust has an indirect effect by altering the surface pH. In fact, the reaction that leads to  $\text{Fe}_6(\text{OH})_{12}\text{CO}_3$  produces almost twice  $\text{H}^+$  compared to the siderite precipitation reaction.  $\text{Fe}_6(\text{OH})_{12}\text{CO}_3$  formation is accelerated at a low flow rate, so is the precipitation rate of chukanovite with respect to siderite. Chukanovite precipitation is faster at lower applied anodic potential when  $\text{Fe}^{2+}$  supersaturation is lower. The green rust precipitation is unaffected by the applied potential. At low dissolved iron conditions, the  $\text{Fe}_6(\text{OH})_{12}\text{CO}_3$  precipitation overcomes the siderite one, leading to a decrease in the surface pH that favors chukanovite precipitation over siderite. The formation of secondary phases such as magnetite and  $\text{FeOOH}$  is attributed to chukanovite further oxidation [45]. In any case nor corrosion rate or weight loss measurements were performed, therefore it was not possible to determine which phase is the most protective. Considering the work of Joshi *et al.*, a reasonable assumption would be that siderite is the most effective component that protects the metal surface [44].

## 1.6 Bibliography conclusion

The protectiveness of corrosion products is an extensive subject with multiple aspects to be considered. The chemical interactions between metal and the environment are rather complex because there are several carbonated species involved with the electrochemical reactions. Many questions are left open: no clear species are identified as responsible for the pseudo-passive behavior of the iron carbonate scales, nor the exact electrochemical mechanism that makes a surface pseudo-passive. A thorough correlation between conditions of nucleation and growth and corrosion deposit protectiveness is missing.

The conditions for promoting pseudo-passivation will be a major objective in the study in order to investigate the protection mechanism of the scales. As reported in this section, there are multiple

factors affecting the formation of iron carbonate scales. The first important parameter is the supersaturation factor (defined by Equation 2) which is linked to the pH, the carbon dioxide partial pressure and  $\text{Fe}^{2+}$  concentration inside the solution. A second key parameter for the iron carbonate precipitation is the temperature which has to be above a certain threshold in order to allow film nucleation. In fact, the corrosion rate has to be slower than the scales precipitation rate in order to avoid undermining effect (the steel corrodes too fast, no substrate for the CPL) and to obtain compact scales [40].

Pseudo-passive scales could precipitate on API X65 carbon steel in a  $\text{CO}_2$  saturated solution at  $80^\circ\text{C}$ ,  $p_{\text{CO}_2} = 0.53$  bar 1% NaCl aqueous solution [46]. Pseudo-passive scales precipitated for pH values higher than 6, nevertheless  $\text{Fe}^{2+}$  ions were added for the lowest pH tested in order to accelerate the scales formation. In fact, 100 ppm and 50 ppm  $\text{Fe}^{2+}$  were added to pH 6 and pH 6.6 solutions, respectively. Pseudo-passivation occurred in less than one week for all cases.

These studies will be useful in the experimental part as a starting point for finding reference conditions

The link between protectiveness and scales precipitation is necessary to prevent uniform and localized type  $\text{CO}_2$  corrosion attacks. As the chemical composition of a protective layer depends on the experimental conditions of the tests, many compounds were observed such as chukanovite, siderite, goethite, magnetite and  $\text{Fe}_6(\text{OH})_{12}\text{CO}_3$ . Understanding their respective role in the protectiveness of the iron carbonates scales is a key passage in order to manage the corrosion phenomenon.

The composition of the surface chemistry plays also an important role: several studies highlight the “anchorage role” of the cementite network with respect to siderite nucleation and growth.

Several studies have been made investigations on the effect of contaminant species such as oxygen,  $\text{Cl}^-$  and  $\text{Ca}^{2+}$  in the formation of iron carbonate scales. For industrial applications, these contaminations have an important impact and one of them (oxygen) is studied in this work.

This section surveyed the prominent features of  $\text{CO}_2$  aqueous solutions in relation to the scales precipitation and their protectiveness. In this study the protectiveness of the scales is the major topic and it is analyzed considering the electrochemical mechanism leading to surface protection and the impact  $\text{O}_2$  has on scales protectiveness. Therefore, a thorough knowledge of the literature concerning the conditions of precipitation, electrochemical reactions and chemical contamination was necessary in order to investigate efficiently these aspects. In particular, the literature concerning precipitation kinetics and pseudo-passivation was considered in order to gather information relative to possible mechanism explaining the reaction behavior before and after pseudo-passivation. The contaminants literature was surveyed in order to observe the experimental methods in order to better isolate the effect of the contaminants and to find new situations for better investigating the oxygen effect on the scales that precipitate in this environment.

The following part of the document concerns the experimental methods that were used for investigating the protectiveness of the corrosion product layer. A first section deals with the experimental techniques whereas the second part addresses the procedures adopted for the experiments.

## 2 Materials and experimental methods

This chapter is dedicated to the experimental methods that were applied in this study. The techniques used are presented from a practical viewpoint and in relation to their contribution to the study results.

The developed procedures for the investigation of the corrosion product film were designed with the aim of observing several aspects of the film protectiveness such as the pseudo-passivation features and the effect of the introduction of small quantities of oxygen (hundreds of ppb) in several moments of the test. A summary of the path followed in designing the experiments is reported in Figure 10.

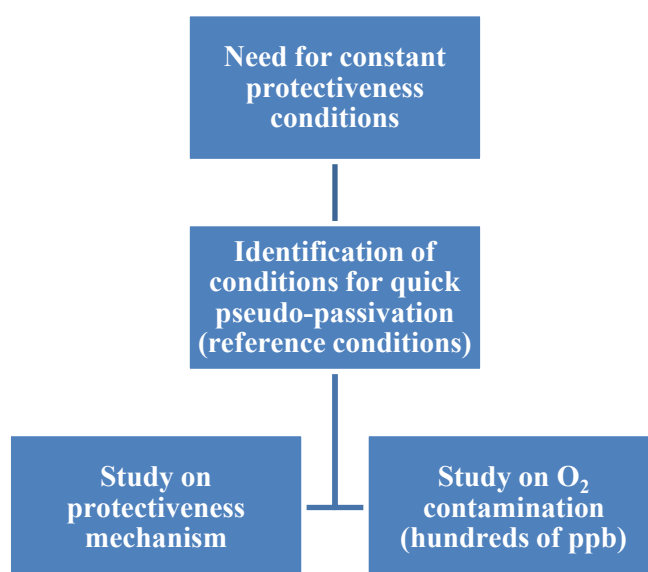


*Figure 10 Diagram of the experiment design path.*

This study is focused on a corrosion product layer which is a complex system requiring to be analyzed from different perspectives for linking protectiveness with surface properties. Besides the electrochemical measurements, other surface analysis techniques such as XRD, SEM, Raman spectroscopy were used for finding a relationship between the electrochemical results, the morphology and the composition of the corrosion product layer. Moreover, ASTM standards were followed for the determination of corrosion rate through mass loss and the quantification of localized corrosion after the introduction of oxygen contamination in the CO<sub>2</sub> gas flow.

## 2.1 Material

In this section the composition and metallographic structure of the carbon steel material studied are reported.

API 5L X65 steels can have a wide variety of carbon content. The material used in this study has a low carbon content. Its composition is reported in *Table 1*.

*Table 1 API 5L X65 chemical composition in weight percent.*

C	Si	Mn	P	S	Cr	Mo	Ni	Cu	Nb	Ti	V	Fe
0.04	0.33	1.33	0.009	0.002	0.056	0.015	0.041	0.029	0.042	0.016	<0.005	bal.

To characterize the metallographic structure of the carbon steel, a sample of 0.5 cm x 1 cm x 0.5 cm was embedded in an epoxy resin. Then, it was polished with SiC paper with increasingly finer granulometry. In the end, diamond paste was used for the final mirror finishing. Afterwards, an attack was performed wetting half the surface with a Nital solution (2 % HNO<sub>3</sub> in EtOH) using a cotton stick. The attack was carried out at room temperature for one minute. Subsequently, the sample was rinsed with distilled water and ethanol. The etching cycle was repeated until a satisfactory contrast was given between the carbon-rich phases and the rest of the surface. The observation of the metallic attacked surface was carried out with the optical microscope Leica DM 4000 M controlled by a PC using the in-house software Leica application suite.

Figure 11 shows the metallographic structure of the metal after etching. It is mainly formed of ferrite grains with small cementite islets dispersed on the surface and where few carbon-rich perlite grains are found.

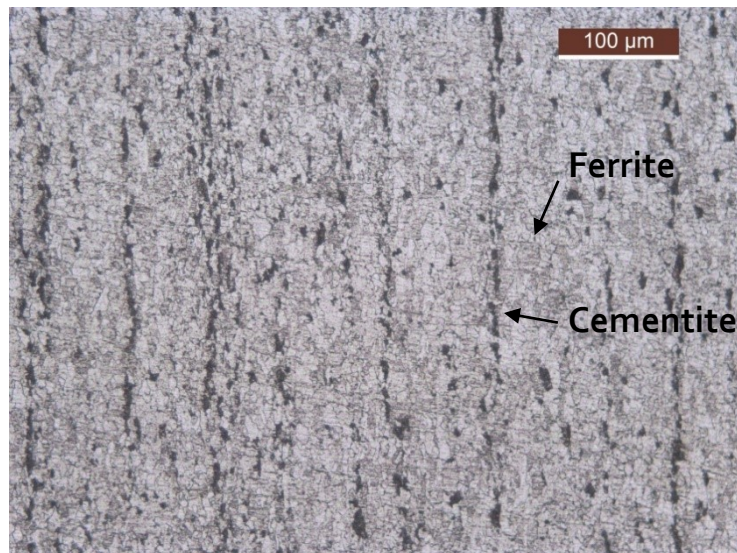


*Figure 11 Optical micrograph showing the metallographic structure of the API 5L X65.*

## 2.2 Electrochemical devices

This section is dedicated to the electrochemical cells for testing the corrosion behavior of carbon steel in a CO<sub>2</sub> aqueous solution. A Biologic VSP 200 potentiostat was used for all the electrochemical measurements performed. The potentiostat was controlled by the EC-LAB software V11.31.

All electrolytes used and their conditions (CO<sub>2</sub> and O<sub>2</sub> content, the pH and the temperature) are precised in the protocol definition part. Many different experimental conditions were chosen to carry out the thesis work. For the purpose of clarity, the chapter ends with a summary of all these conditions chosen for the search for the reference experimental condition, the study of pseudo-passivity and the effect of oxygen contamination on it.

### 2.2.1 Electrochemical cells

Two 3 electrodes setup electrochemical cells were used. One with a rotating electrode (cell A, Figure 12) and one with several working electrodes (cell B, Figure 13). The rotating electrode cell (cell A) had a small volume (250 mL) with the place for a pH electrode, the three electrodes for the electrochemical measurements and the gas inlet and outlet. The cell had a double jacket for heating the solution inside, a condenser was placed at the gas outlet in order to keep the corrosive solution volume constant. The corrosion coupons were placed at the bottom of the cell on their side. The multi working electrode cell (cell B) was bigger than cell A with a 1.2 L volume. This cell was equipped with all the instruments of cell A with the addition of a thermometer and a septum for the pH correction of the corrosive solution. Both cells were airtight to avoid atmospheric contamination of the corrosive solution. In order to check that airtight conditions were maintained, the gas going out from the cell was directed into a check valve. If bubbling occurred in the check valve, the system was deemed airtight.

The three electrodes cells are composed by a reference electrode, a counter electrode and by a working electrode. The reference electrode (RE) was an Ag/AgCl 3 M (208 mV/SHE). It has a constant potential throughout the measure so to ensure that any change in OCP is attributed to a variation of the working electrode potential. Because of the temperature used for the most part of the experiments (80°C), a salt bridge was used in order to avoid any deterioration of the RE. The salt bridge solution was a 3 M KCl solution. The counter electrode (CE) was a platinum grid whose active surface is significantly greater than that of the working electrode. Platinum electrodes used in the experiments were conical section baskets with a fine mesh whose dimensions are 2 cm smaller diameter, 3.5 cm higher diameter, 2 cm height. The baskets were connected with a platinum wire embedded in a resin and a glass tube.

Concerning the working electrode, it was constituted by API 5L X65 carbon steel. The geometry of the samples depended on the test and their objective (Figure 14). For the rotating cylinders electrodes (cell A), the sample was a cylinder with 1 cm diameter and 2 cm height. The upper face was pierced and threaded to attach the WE to the rotating axis. For the study of localized corrosion (cell B), prismatic samples (1 cm x 1 cm x 1.8 cm) were used. The upper surface was pierced, and an electrical connection was tin welded. A high-temperature resistance resin was applied over the upper face and the welding. The corrosion analysis coupons were pierced with a hole of 2 mm diameter. For all tests, every steel specimen was polished with P800 SiC paper. After that, they were cleaned with distilled water and rinsed with ethanol in an ultrasonic bath.

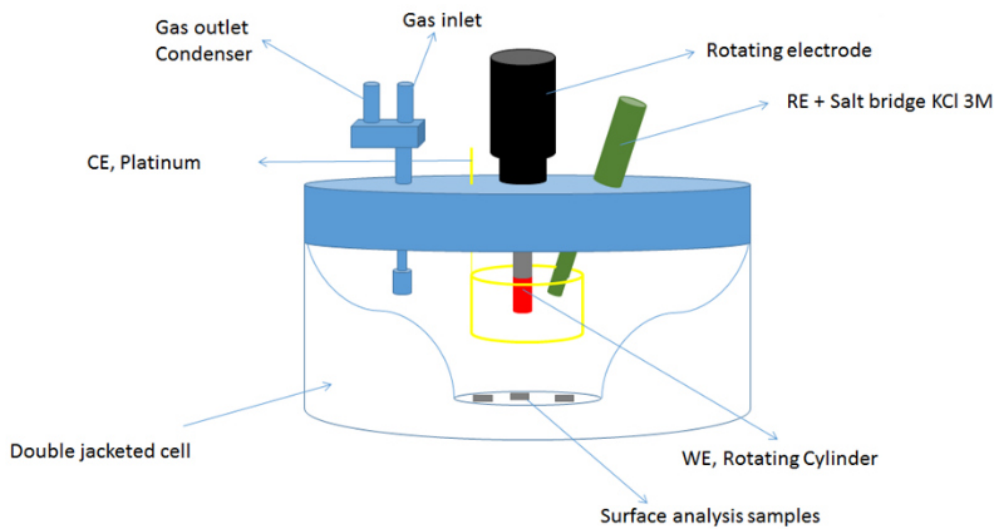


Figure 12 Diagram of the electrochemical cell A.

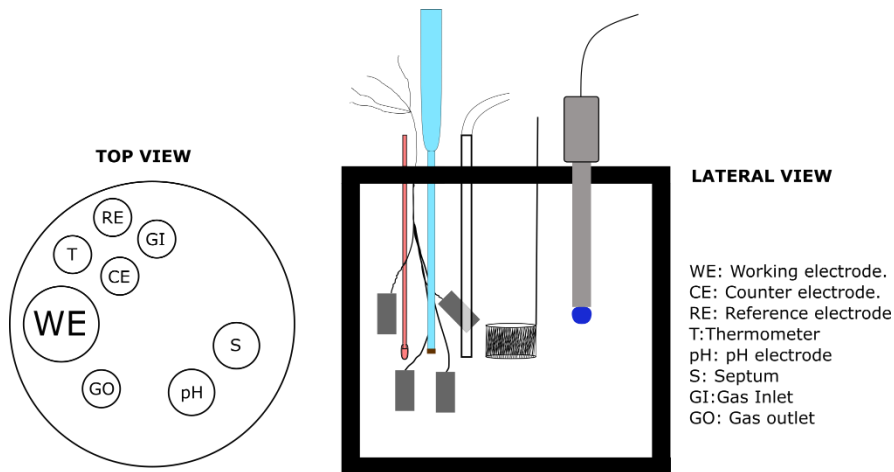


Figure 13 Diagram of the electrochemical cell B.

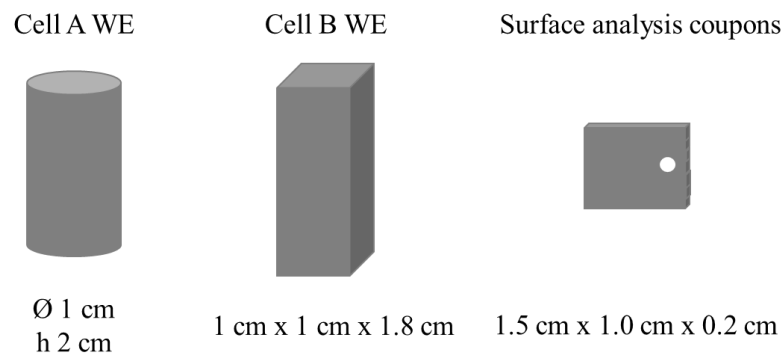


Figure 14 Diagrams of working electrodes geometry. Cell A iron wool method in dynamic conditions, pseudo-passivity investigations and introduction of oxygen since the start of the test. Cell B: iron wool method in static conditions and oxygen introduction in pseudo-passive state.

### 2.2.2 Control of pH and dissolved O<sub>2</sub>

Among the instruments that equipped the electrochemical cell, the pH electrode is a key one since pH is a key parameter for carbonates precipitation as seen in the bibliography part.

In this study, Fisherbrand pH electrodes by Fischer were used for the monitoring of solution pH throughout the test. Before each test, the pH electrodes were calibrated using two buffer solutions at pH 4 and 7. The calibration was performed at room temperature, a mathematical temperature correction was automatically applied by the instrument so to read the correct pH at the experimental temperature. No correction was made for dissolved Na<sup>+</sup>. Between each buffer measurement and before the test, the pH electrodes were rinsed with distilled water. They were immersed in a slightly acidic solution for storage. As the pH electrodes were used at 80°C, their calibration was regularly checked for monitoring the degradation of the electrode.

A part of this study is dedicated to the verification of O<sub>2</sub> contamination in a CO<sub>2</sub> aqueous solution. Therefore, continuous control of the oxygen concentration dissolved inside the test cell was mandatory. In order to do that, an oxygen probe was inserted in the gas flow exiting the electrochemical cell. Optical oxygen probes exploit the quenching effect of oxygen in order to determine its concentration. The oxygen probe (Orbisphere M1100 by Hach) measured the oxygen concentration in the gas phase flowing outwards the electrochemical cell. In order to evaluate the dissolved oxygen inside the corrosive solution, Henry's law was applied (Equation 1). Henry's coefficient was adapted from literature values to the different conditions of salinity and temperature.

A gas control system was used: pure CO<sub>2</sub> and a 20 % O<sub>2</sub>/CO<sub>2</sub> mixture were blended until the desired oxygen contamination of the gas feed was attained.

The mixing of the two gasses took place at the intersection of the two gas lines. The flux is regulated by a flow meter valve; the concentration of oxygen inside the cell is measured *a posteriori* at the gas outlet with an O<sub>2</sub> probe. This system has the advantage of finely tuning the extent of the contamination to be introduced into the gas flow. Moreover, it allowed an immediate interruption of the contamination flow at any moment. Nevertheless, this setup is not able to provide a value of the oxygen content *a priori*, *i.e.* knowing just the gas flow inputs.

Obtaining the needed oxygen content in the gas flow requires progressive oxygen addition before reaching the optimal set-up conditions. Particularly, the hardest difficulty is to have a CO<sub>2</sub> flow that dilutes oxygen to the desired concentration without emptying the CO<sub>2</sub>/O<sub>2</sub> bottle and a CO<sub>2</sub> flow strong enough to keep the testing solution saturated with carbon dioxide.

The electrochemical cells, the electrodes and the O<sub>2</sub> control used in the study have been detailed in this section. In the following one the electrochemical techniques that were applied using the described equipment will be presented in regard with the desired electrochemical information.

## 2.3 Electrochemical techniques

This section deals with the electrochemical techniques used in this study. Those techniques have been mainly employed to determine the corrosion rate relating to the evolution of the scales and their properties. A combination of both steady-state and transient techniques is presented. In the end, a small paragraph dedicated to the rotation electrode for controlled flow conditions is included.

### 2.3.1 Open circuit potential (OCP)

OCP is measured confronting the difference in potential between the reference electrode and the working electrode. Open circuit potential, particularly its evolution during a test, highlights the variations of the kinetics of the cathodic and anodic reactions. Open circuit potential was used for identifying when pseudo-passivation is taking place on the surface. Identifying in which direction the electrochemical reaction rates vary, is an important indicator used for modeling the reaction mechanism and the relative influence of the scales. However, OCP measurements do not give any information on the reason behind those changes that can be related to the nature of the surface or the chemical conditions of the electrolyte. Finally, corrosion rate cannot be determined with this technique, other methods have to be used.

### 2.3.2 Electrode polarization

Polarizations are applied to the sample in order to determine some electrochemical parameters and even to determine the corrosion rate.

In this study both potentiostatic and potentiodynamic polarization were adopted with different purposes.

Potentiostatic polarization was used because it could give important information on the kinetic of the electrochemical reactions before and after pseudo-passivation. The dependency of the variation of the current density, as a function of potential is a key parameter to be observed in order to determine which mechanism (activation / mass-transfer control for example) occurs. As the potentiostatic polarization is not enough to determine exactly the mechanism, the electrochemical impedance spectroscopy was performed right after. Furthermore, potentiostatic polarization had the advantage of putting the system in a steady state condition right before the impedance measurement. Therefore, potentiostatic polarization was used both to investigate the electrochemical mechanism of the reactions and, at the same time, to take the system to a steady state before electrochemical impedance spectroscopy (EIS).

Potentiodynamic polarization was used to determine the Stern-Geary coefficients of the reaction in active and pseudo-passive states both in the presence and absence of oxygen contamination. Moreover, potentiodynamic polarization can give easily more kinetic information on a wider potential range than potentiostatic polarization. Therefore, potentiodynamic polarization was used to further verify the behavior of the electrochemical reaction in the presence and absence of the corrosion scales and how some processes such as the reduction of oxygen influence the global kinetic of the cathodic reactions. Unfortunately polarizing the samples at high overpotentials may lead to modifications of the corrosion product layer thus it can be used only once on each sample.

Concerning the experimental parameters, each sample was polarized either to anodic or cathodic potentials for avoiding any modifications of the surface that could alter the result of the polarization. Potentiostatic measurements were polarized at  $\pm 40$  mV then  $\pm 80$  mV then  $\pm 120$  mV vs OCP.

Polarization lasted 15 minutes. EIS was performed after the polarization before going to the next overpotential step.

In relation to potentiodynamic polarization, each sample was polarized from its OCP to  $\pm 25$  mV at  $0.25$  mV/s. Before the polarization, an impedance measurement was performed to determine the solution resistance. This impedance for ohmic drop determination was performed between  $300$  kHz and  $1$  Hz with a  $10$  mV sinus amplitude starting from the OCP using a conductimetric cell.

### 2.3.3 Linear polarization resistance technique (LPR)

Electrode polarization can be employed to determine the corrosion rate of the WE. However, its destructive nature does not allow to follow the evolution of protectiveness throughout the test. For this specific need, linear polarization resistance was employed.

Linear polarization resistance (LPR) is a technique widely employed for measuring the corrosion rate of the working electrode at any given moment. This method is particularly useful because it is non-destructive, however some assumptions must be verified in order to get the true value of the corrosion rate.

These assumptions are that the reaction is limited by the charge transfer, that the Ohmic drop is negligible and that the value of the Stern Geary coefficient is known. Stern Geary coefficient can be calculated using the parameters of a potentiodynamic polarization as it was done in this study in different conditions. The rest of the conditions are normally met for an active surface although careful considerations must be done if the scales change the mechanism of the electrochemical reactions.

Moreover, LPR is meaningless if corrosion is not uniform. Therefore, no significant corrosion rate values are obtained when dealing with localized corrosion.

Nevertheless, when these conditions are met, LPR is useful in determining the corrosion rate at any given moment in the system. Particularly, because of its non-destructive method, it was used in this study to follow the variation of the corrosion rate during the exposure time. This measurement provides indeed an important initial parameter to evaluate the change in protectiveness of a scale precipitating on the carbon steel surface as a function of the exposure time.

In this study for routine corrosion rate determination, the working electrode was polarized between  $\pm 15$  mV vs OCP at  $0.25$  mV/s. The Stern-Geary coefficient used is  $27$  mV/dec for pure CO<sub>2</sub> conditions,  $24$  mV/dec for CO<sub>2</sub> + O<sub>2</sub> in active state and  $31$  mV/dec for CO<sub>2</sub> + O<sub>2</sub> in pseudo-passive state.

Testing scales precipitation in different conditions is necessary to fully evaluate its protectiveness and electrochemical impedance spectroscopy can be used in order to investigate the mechanism of electrochemical reactions.

### 2.3.4 Electrochemical impedance spectroscopy (EIS)

Electrochemical impedance spectroscopy is a transient technique that gives precious information on the processes occurring at the interface between the metal and the solution as well as a quantification of physicochemical parameters of the interface.

EIS is a non-destructive technique (in stationary conditions) so it can be used in order to monitor the evolution of the corrosion process during the test. The fact that it does not alter the surface is particularly precious in the study of precipitated scales since the protectiveness provided by the corrosion product layer (CPL) is strongly affected by the exposure time.

The electrochemical impedance spectroscopy was used following three pathways. The first one was to follow the evolution of the electrochemical reactions during the precipitation of the scales in a qualitative manner. This approach involved measuring several spectra at different corrosion times. The second one was to exploit the impedance data in a quantitative way so to have a strong base for modelling the behavior of the electrochemical reactions before and after pseudo-passivation. Indeed, using the electrochemical equivalent circuit approach, several electrochemical parameters were obtained and compared one with each other in relation with several proposed mechanism. The third one was to observe the variation on the system impedance upon applying a given variation (potential and convection) in order to further support the model claims. Specifically, several electrochemical impedance spectra were either obtained in different flow conditions or starting from a potential different than the OCP. Furthermore, measuring the electrochemical impedance at different overpotential allow to find which electrochemical process, anodic or cathodic, is more relevant on the definition of the impedance at OCP.

Among several impedance representations Nyquist plot (real vs imaginary part of impedance) and Bode plots (impedance modulus and phase vs logarithmic frequency) are the most common. Nyquist plots are useful for visualizing the mechanism and system evolutions whereas Bode plots are better suited for detecting time constants and observing CPE behavior. In the study either one or both representations will be presented depending on their contribution to the results interpretation.

EIS requires a steady state to be able to interpret the electrochemical mechanism at the carbon steel/electrolyte interface. This condition was not met in specific conditions when oxygen contamination was present so that EIS data could not be exploited.

In this study for routine impedance measurement, the working electrode was polarized between  $\pm 10$  mV vs OCP with a frequency range going from 30 kHz to 10 mHz. A ten-point per decade resolution was used repeating the measurement at least twice for each frequency.

### 2.3.5 Flow convection - rotating electrode

The reaction rate can be influenced by the electrode potential or the reactant concentration at the surface. In order to study the latter, changing flow conditions are needed. Moreover, different flow conditions are interesting because they can mimic real scenarios such as a liquid flowing into a pipeline.

For this reason, the rotating electrode was used in this study and it will be described in this section. Electrochemical reactions are not always limited by the electron charge transfer (activation limitation) but also by the diffusion of the reagents to the surface electrode where the electrochemical reactions take place. Therefore, the rate of these reactions is not influenced by the potential or the chemical nature of the electrode but by the diffusion parameters that depend on hydrodynamic conditions or the scale thickness and porosity.

For these reasons, an electrode that works with controlled flow conditions is necessary to investigate this kind of reaction. A rotating electrode controls the flow conditions applying a rotation rate to the electrode with an engine. The rotating electrode was used for determining the properties of the electrochemical reactions in different flow conditions especially when in a pseudo-passive state. The observations were used in support of the modeling effort for explaining the protectiveness of pseudo-passive scales. The rotation electrode system used in this work was an Orignalys Oringatrod rotating electrode. The system was composed of an electric motor and a mechanical junction chamber. To preserve the mechanical part from corrosion, a steady flow of nitrogen or argon was supplied to the electrode. The working electrode was fixed to the vertical rod, which was connected to the control box

where the desired rotation rate was selected (in rpm). Cylindrical-shaped working electrodes were used. Use of classical RDE was discarded because gas bubbles remained adherent to the electrode, covering the surface entirely, and thus preventing any electrochemical measurement.

For identification of a reference condition, constant rates of 180 and 600 rpm were applied for the rotation of the cylindrical carbon steel. When dealing with the mechanism of the reaction in dynamic conditions, pseudo-passivity was reached applying a 600 rpm rotation. Subsequently the rotation rate was changed from 600 rpm to 2100 rpm with a 300 rpm step.

## *2.4 Complementary characterization techniques for scales and carbon steel surfaces*

The usefulness of the electrochemical techniques related to the investigation of the corrosion product layer was described in the previous section. In order to find a correlation between the protectiveness and scales features, surface analysis techniques must integrate the characterization of the corrosion product layer. The following section will explain the reasons behind the choice and use for the surface analysis techniques and the mass loss measurements.

### **2.4.1 Mass-loss measurement**

Mass loss measurement is the most reliable method for measuring the rate of uniform corrosion. It consists of measuring the mass of a corrosion coupon before and after the test. This method was used in the study to assess the global corrosion rate and to compare it with LPR corrosion rate measurements.

Unfortunately, the method requires dissolving the corrosion products layer. Therefore, the samples cannot be reused for other surface analysis methods.

Mass loss measurements were performed following ASTM G1 standard. Before the test, the mass and the dimensions of the specimen were measured. Once the test was completed, the samples were taken out of the cell rinsed with distilled water, acetone and then dried with compressed air. Their weight was measured the first time as they were. Afterward, several cycles in inhibited acid solutions were performed in order to remove the corrosion products layer. The pickling solution was prepared by mixing 500 mL of HCl 37% with 500 mL of distilled water and 3.2 g of HMTA as a corrosion inhibitor. After each cycle the mass was measured again, the final mass was obtained intersecting the line fitted with the data having a decreasing mass with those having a constant mass.

### **2.4.2 Scanning electrochemical microscopy (SEM)**

Scanning electrochemical microscopy (SEM) is interesting for observing the morphology of the corrosion product layer. SEM resolution is higher than the one of the optical microscopes because it uses electrons instead of light for surface observation. Moreover, the technique has a higher depth of field *i.e.* a higher portion of the image is in focus than optical microscopy.

Back-scattered electrons give both information related to the sample morphology as well as qualitative information about the phases present in the sample. The areas that have heavier atoms are seen brighter than the others.

This technique was widely used in this study for observing the morphology of the corrosion product layer and the surface coverage. The principal observed parameters were the crystals shapes, sizes, layer thicknesses and the features of localized corrosion morphologies. Observing the state of the surface is essential for correlating the protectiveness of the scales with the morphology of the surface.

A full characterization of the scales needs to integrate both top-view images and profile pictures in order to observe even the metal/scales interface.

SEM was used with secondary electrons imaging. The equipment was a FEI Nova Nanosem 450. The samples for direct observation were directly put on appropriate sample holders and then inserted in the high vacuum chamber. The cross-section samples were embedded in epoxy resin then polished with SiC paper up to 3  $\mu\text{m}$  diamond paste. Before the observation the specimens were made conductive through carbon deposition. The deposition was made passing a current between 60 A and 70 A for 0.8 s through two close graphite bars. Once a high vacuum was made inside the SEM chamber, the electron gun was turned on and different potentials spot combinations were adopted. The most used potential was 5 kV and spot 4, other configurations were 20 kV spot 3.5 or 15 kV spot 4. Before taking pictures, the beam was calibrated for avoiding electron oscillations and linking the working distance to the moving stage position. According to the needs, either back-scattered electron detector, secondary electron detector or EDS detectors were used. For each picture, a scanning time of 10  $\mu\text{s}$  was adopted.

The cross-section images of argon ion polished samples were obtained with the same instrument. Ion polishing was performed on 10 mm x 10 mm x 4 mm carbon steel samples exposed to the corrosion environment. The samples were prepared with a Gatan Ilion + in cross-section mode apparatus and were bombarded for 5 hours at 5 keV and 5 hours at 6 keV before observation with back scattered electrons.

SEM is a powerful technique for determining the morphology of the scales but it gives little information on the composition of the corrosion product layer. In order to answer to this question grazing incidence X-ray diffraction was used.

### 2.4.3 Grazing incidence X-ray diffraction (XRD)

X-ray diffraction (XRD) exploits the interaction of X-rays with a crystalline phase. The result of this interaction is a diffractogram that is characteristic of the phases analyzed. Grazing incidence X-ray diffraction (GIXRD) is a variation of XRD where the incident X-rays have a low incidence angle over the sample. This feature allows a better analysis of the sample surface composition.

The technique was employed to determine the composition of the corrosion product layer on dedicated surface analysis coupons. One application was to investigate the pseudo-passive scales composition. In order to have more information on the scales rather than the metal substrate, GIXRD was preferred to XRD. However, GIXRD does not concentrate on a specific spot, but it gives a composition information on a wider surface. Therefore, the composition of specific corrosion features identified with SEM such as the localized corrosion features found, cannot be detected with this technique. Knowing the scales composition is a key parameter in order to relate the phase composition to the protection provided to the metal substrate.

GIXRD analysis of the samples was performed using a PANalytical X'Pert Pro Diffractometer, using Cu-K $\alpha$ 1 as incident radiation whose wavelength is 1.5406  $\text{\AA}$ . The instrument was in a Bragg-Brentano geometry using a 35 mA-35 kV working power. The investigated angular range ( $2\theta$ ) was between 15° and 78° with a 0.033° angular step resolution. Total acquisition time was 2 h 40 min, which means each step was measured for 5 seconds. The incidence angle was inferior to 1°. A monochromator was present on the path of the diffracted beam in order to select the desired diffraction angle. The specimens were oriented so the incident light could get through the corrosion product layer at a low angle. As explained previously, this was done in order to avoid X-Ray penetration in the carbon steel substrate and to have a signal related to the composition of the CPL.

X-ray spectra were attributed with the Eva software by Bruker using the PDF 4-+ database of the international center of diffraction data.

GXRD is a powerful technique determining the composition of the corrosion product layer, but it is limited to large surface therefore it was not suited for analyzing the composition of the phases in specific spots that could be individuated with SEM. In order to overcome this limitation, Raman spectroscopy was used.

#### 2.4.4 Raman spectroscopy

Raman spectroscopy allows to detect the chemical phases that compose the corrosion product layer with a high lateral resolution. Moreover, the exact spot where to perform the analysis can be identified using imaging techniques. The micrometric lateral resolution allows to differentiate two phases close with each other.

These advantages make the technique essential for detecting the phases around the localized corrosion features observed in the presence of oxygen. The ability to select where to perform the analysis compensates the defects of GXRD and the technique is able to detect the phases on the surface since laser light does not penetrate in the iron carbonate layer. Moreover, the analysis of the results is more complicated since Raman Spectra databases have less references than XRD and some characteristic peaks may overlap if many species are present.

Anyhow these disadvantages did not prevent the analysis to be carried out successfully and indeed it was a powerful tool to determine the phases around and inside the localized corrosion features.

In this study, the instrument was a Renishaw inVia Raman spectrometer. The samples were first observed with an optical microscope to identify the spots where the analysis had to be performed. Once the desired spot was identified the instrument was switched to the laser mode in order to acquire Raman spectra. The incident light was produced with an argon laser whose wavelength is  $514\text{ nm}$ . A built-in CDD detector was used for acquiring the Raman spectrum of the corrosion product layer.

The exposure time and the power of the laser were adjusted in order not to saturate the detector and to have sufficient peak intensity and signal-noise ratio. The maximum laser power used was 0.5% of its total power, the maximum acquisition time was  $400\text{ s}$ , several combinations are possible in these two ranges. Identification of the phases was done comparing the spectra to other crystalline phases Raman spectra found in the literature.

Raman spectroscopy was the main technique used for determining the phases around and inside the localized corrosion features. Nevertheless, a further step was needed in order to measure the protectiveness of the scales with respect to localized corrosion. For this reason, pit depth was measured with a profilometer.

#### 2.4.5 Profilometer

The need for pit depth measurement was due to the localized corrosion features present when an  $\text{O}_2$  contamination was introduced in a  $\text{CO}_2$  aqueous solution. Particularly it was necessary to establish whether  $\text{O}_2$  was truly responsible of these effects and if the localized corrosion features stopped forming and propagating once the oxygen contamination was not present anymore. The profilometer was the perfect technique in order to achieve this result. Unfortunately measuring the pit depth with this technique requires that the corrosion product layer is removed from the surface. This means that the scales are destroyed for this measurement, thus any other surface analysis targeting the scales should be performed before.

In this study the profilometer used was a Hirox RX-100, the instrument was controlled with a PC thanks to the in-house software. After pickling with an inhibited acid solution (500 mL HCl 37%, 500 mL distilled water and 3.2 g HMTA) a 2 D cartography of each specimen facet was performed. Subsequently, all the pits visible to the naked eye were measured for pit depth determination. A 3D profile of the pit and the surrounding area was acquired and a correction for surface inclination was done. The pit depth was measured by extracting the profile of the pit across one direction. The reference line for depth determination was the area surrounding the pit. Subsequently, the data were treated following ASTM G46 standard.

## 2.5 Experimental protocols

In this section the protocols for the tests performed in this study will be detailed. Three sections are proposed: the investigations for finding a reference conditions, the study on the pseudo-passivation mechanism and finally, the effect of oxygen contamination on the corrosion product layer. At the end of this section, before concluding, a summary of the experimental conditions and the cells will be presented.

The first section is justified by the need of finding homogeneous protective conditions for further investigations, particularly for the oxygen contamination and the reaction mechanism. The second one uses the identified reference condition for investigating the pseudo-passivity mechanism. The third one uses the reference conditions adding O<sub>2</sub> for observing its effect on the corrosion product layer.

### 2.5.1 Standard protocol for the electrochemical tests

In order to study the reference conditions for pseudo-passivation, a standard procedure was developed. Hereafter the solution preparation and relative conditions are detailed as well as the electrochemical parameters used. These conditions are very important since they were used for all tests, any difference with this standardized procedure will be detailed in the relative section.

The testing solution was an aqueous solution saturated by carbon dioxide heated to 80°C. The solution contained 2 g/L dissolved salt to act as an electrolyte. The pH was different according to the experiments performed. When the iron wool was present the pH of the solution was set to 6.6, without iron wool the pH was set to 6.8. An appropriate amount of NaHCO<sub>3</sub> was added before saturation with carbon dioxide in order to get the desired pH in the testing conditions.

The experimental conditions used for carrying out those tests were kept constant during any test. Therefore, any evolution of pH was corrected with an appropriate deaerated solution. The pH of the carbonate buffer was corrected during the test, with deaerated 1 M HCl or 1 M NaHCO<sub>3</sub> according to the pH correction to be made.

The solution was prepared bubbling overnight carbon dioxide into the preparation bottle and transferred into the sealed electrochemical cell with all the equipment ready for the experiment. Before transferring the solution from the preparatory bottle, the electrochemical cell was deaerated with an inert gas for 30 min. The transfer took place without any contamination of the solution from the atmosphere. This procedure ensures that the residual dissolved oxygen content is maintained around 10 ppb, considered as an anoxic environment.

After the introduction of the solution into the electrochemical cell, the temperature was increased and maintained at 80 ± 2 °C. Continuous bubbling of CO<sub>2</sub> inside the solution gas was carried out during the experiment to keep a constant content of dissolved CO<sub>2</sub> (pCO<sub>2</sub> 0.54 bar). Gas bubbling was necessary because the concentration of dissolved carbon dioxide influences both the buffer pH and the

rate of the iron dissolution reaction. A scheme illustrating the experimental procedure is reported in Figure 15.

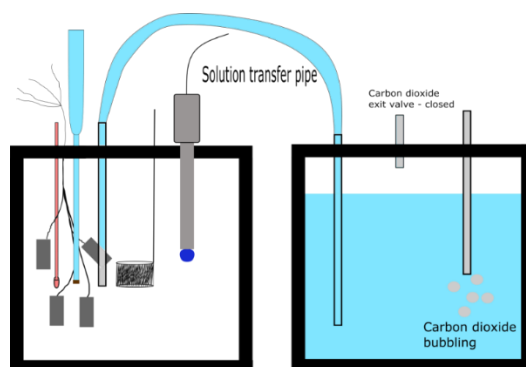


Figure 15 Solution transfer diagram.

LPR and EIS were performed at regular intervals (every three hours) in order to monitor the evolution of the scales over the surface. OCP was measured also in-between the electrochemical measurements for detecting when pseudo-passivation occurred.

### 2.5.2 Dissolved iron setup for pseudo-passivation acceleration

A reference condition is needed in order to further investigate the parameters affecting the corrosion product layers (CPL). The features of the scales depend on environmental conditions and exposure time, so a clear and fixed condition is to be found. Pseudo-passivation protection mechanism is still unknown, pseudo-passive scales have similar protectiveness and it is easy to detect with electrochemical techniques. Therefore, pseudo-passivation represents a promising starting point for scales protectiveness investigations.

Pseudo-passivation is strongly related to the kinetics and thermodynamics of iron carbonate precipitation. Previous testing at IFPEN showed that a pH 6.6 0.2% NaCl CO<sub>2</sub> saturated solution at 80°C produced pseudo-passive scales after 8 days of immersion on API X65 carbon steel samples. Therefore, the beginning of the study was focused on accelerating the same conditions of the previous IFPEN work and, most importantly, on verifying if these conditions methodically result in a pseudo-reproducible passivation process of the surface. Increasing the temperature or the supersaturation either with a pH increase or higher Fe<sup>2+</sup> concentration represents three possible pathways for the promotion of pseudo-passivation. The first path considered for promoting pseudo-passivation was to increase the concentration of iron ions in the solution “buffering” its concentrations with iron wool. Both static conditions and dynamic conditions were tested in order to observe the scaling properties of the selected parameters.

#### 2.5.2.1 Static conditions

Hereafter the experimental procedure adopted is reported, two confinement ratios were investigated 1.9 cm<sup>-1</sup> and 0.6 cm<sup>-1</sup>. In this study, the confinement ratio is defined as the ratio between the exposed area ( $A_{\text{exposed}}$ ) and the volume of the testing solution ( $V_{\text{solution}}$ ) as reported in the following equation.

$$C_{\text{ratio}} = \frac{A_{\text{exposed}}}{V_{\text{solution}}}$$

Equation 5

The testing solution conditions and preparation were described in the previous section.

The three electrodes set-up electrochemical cell (Figure 13) was prepared for the measurement with the addition of a carbon steel corrosion coupon (Area  $4 \text{ cm}^2$ ). Moreover, pure iron wool was added so to have a higher surface/volume. Particularly, two confinement ratios were tested:  $1.9 \text{ cm}^{-1}$  and  $0.6 \text{ cm}^{-1}$ .

Iron wool was added to the electrochemical cell in order to accelerate the pseudo-passivation of the surface increasing the rate of iron carbonate precipitation. In fact, higher dissolved  $\text{Fe}^{2+}$  concentration increases iron carbonate saturation and thus the precipitation rate.

The calculation for the quantity of iron wool to add was done considering its specific surface (surface over mass ratio). The diameter of the iron wool was measured with a stereomicroscope in order to determine the area-on-volume ratio assuming the iron filament as a perfect cylinder. The specific surface of the iron wool can then be calculated by knowing its density ( $7.8 \text{ g cm}^{-3}$ ). The relationships are reported hereafter in the following relationship.

$$\frac{A}{V} = \frac{2\pi r l}{\pi r^2 l} = \frac{2}{r} \Rightarrow \frac{A}{m} = \frac{A}{V} \cdot \rho^{-1}$$

*Equation 6*

Where  $A$  is the area,  $V$  the volume,  $r$  the filament radius,  $l$  the filament length,  $m$  the mass and  $\rho$  the iron density. The volume of the solution was measured at the end of the test so as to have the actual confinement ratio value.

At the end of each experiment, corrosion coupons were removed from the cell, rinsed with acetone and distilled water and dried to prevent the onset of further corrosion processes. The samples were then retained under vacuum in a freezer before surface analysis that consisted of scanning electron microscopy (SEM), X-Ray diffraction (XRD) analysis.

### **2.5.2.2 Dynamic conditions**

The conditions for the formation of pseudo-passive scales were also tested in dynamic conditions with an electrochemical cell adapted for the use of a rotating electrode (cell A, Figure 12). Dynamic conditions are similar to those found in industrial environments. Moreover, the need for studying pseudo-passivation even in a dynamic regime made necessary to have reliable conditions for obtaining pseudo-passive scales in dynamic conditions.

The experimental conditions for the corrosive solution were the same of the previous section. However, in this case three rotation rates were chosen namely 0 rpm, 180 rpm and 600 rpm.

Iron wool guaranteed a  $1.7 \text{ cm}^{-1}$  confinement ratio. The wool was positioned at the bottom of the electrochemical cell and kept there thanks to two Teflon grids. Those grids also kept the corrosion coupon (active surface =  $4 \text{ cm}^2$ ) in place.

### **2.5.3 Reference conditions for pseudo-passivation, pH 6.8**

Because of the unsatisfactory results obtained accelerating iron carbonate precipitation with the iron wool, other conditions with **higher pH (6.8) and without iron wool** were tested with the cell A (Figure 12). In this case the acceleration was made increasing the pH and thus the carbonates equilibrium concentration. For these reasons, the iron wool was removed and the pH raised to 6.8.

After each test with different dynamic conditions (0 to 600 rpm for the rotation rate of the carbon steel electrode), the corrosion coupons were rinsed with distilled water and acetone, then they were dried in order to remove all excess water. Finally, they were put under vacuum and conserved in a freezer for surface analysis. The techniques used were GXR and SEM both direct observation and cross-section analysis.

In the following sections the text will often refer to “reference conditions”. Those conditions are very important since all the following experiments are variations of these conditions. They are reported in Table 2.

*Table 2 Selected experimental parameters defining the reference condition for the next tests.*

Conditions	Values
Temperature	80°C
[NaCl]	2 g/L
pH	6.8
pCO <sub>2</sub>	0.54 bar

## 2.5.4 Studying the “pseudo-passivation” protection mechanism

### 2.5.4.1 Potentiodynamic polarization test

Tafel slope determination was carried out in order to calculate the Stern-Geary coefficient in different situations namely the state of the surface and the exposure to oxygen contamination. The polarization was used even to study the reaction kinetics in a wider potential range.

One test was conducted in pseudo-passive conditions and one when the surface was active. In the case of active surface, potentiodynamic polarization started after 5 h of exposure time. Both anodic and cathodic polarization was performed.

Cell B (Figure 13) was used for all tests because four samples could be measured in the same test so to maintain similar chemical conditions both for anodic and cathodic polarization. Reference conditions were used in this test, reported in Table 2.

### 2.5.4.2 The effect of potential

This experimental procedure was developed in to study the effect of potential on the electrochemical reactions after the pseudo-passivation of the corrosion product layer. The test had the double objective of monitoring the evolution of the scales until pseudo-passivation and measuring the variations of the behavior of the electrochemical reactions before and after pseudo-passivation. In order to do so, an overpotential was applied to the working electrode during the electrochemical impedance measurement.

The cell A was used for the experiment (Figure 12). No iron wool was present and the pH was 6.8 as per the reference conditions reported in Table 2.

Unfortunately, because of the geometry of the surface analysis coupons and the restricted volume in the electrochemical cell, they were put laying on the bottom of the cell.

The effect of potential was monitored in two situations: after 24 hours of exposure to the corrosive solution and when a pseudo-passive surface was obtained. The first situation represents a surface with scales in the early stage of precipitation providing low protection. The second one represents a later

stage of precipitation that strongly protects carbon steel from corrosion. In fact, 24 hours gives enough time to the system to corrode and also to be almost completely uncovered by the scales thus avoiding any influence on the mechanism of the electrochemical reactions. Pseudo-passivity was identified thanks to the impedance diagrams and the OCP measurement.

The evolution of the scales until pseudo-passivity was measured with EIS and LPR each three hours. A 6 h rest time was given to the system to reach steady state conditions. OCP was measured between the use of the techniques. Once the system was in one of the planned situations, an impedance diagram was registered around the open circuit potential. Subsequently, the sample was polarized to more anodic or cathodic potentials with respect to the OCP for fifteen minutes. The procedure was set as depicted in Figure 16 and it was adopted in order to guarantee a steady current right before the beginning of the impedance measurement. Immediately after the polarization, impedance was measured applying 10 mV sinusoidal oscillation with respect to the last imposed potential.

Increasing potential values were tested, namely  $\pm 40$  mV,  $\pm 80$  mV and  $\pm 120$  mV vs OCP. These values were selected because they were supposed to be higher than the anodic Tafel coefficient and to produce a clear effect when increasing the corrosion current density of one order of magnitude. Each sample was polarized either only anodically or cathodically to prevent modification of the surface or the corrosion product layer due to the polarization of the working electrode. The confrontation of the impedance results at increasing overpotential, at OCP and between the active surface non-passive and pseudo passive states, gives an overview of the mechanism evolution of the electrochemical reactions.

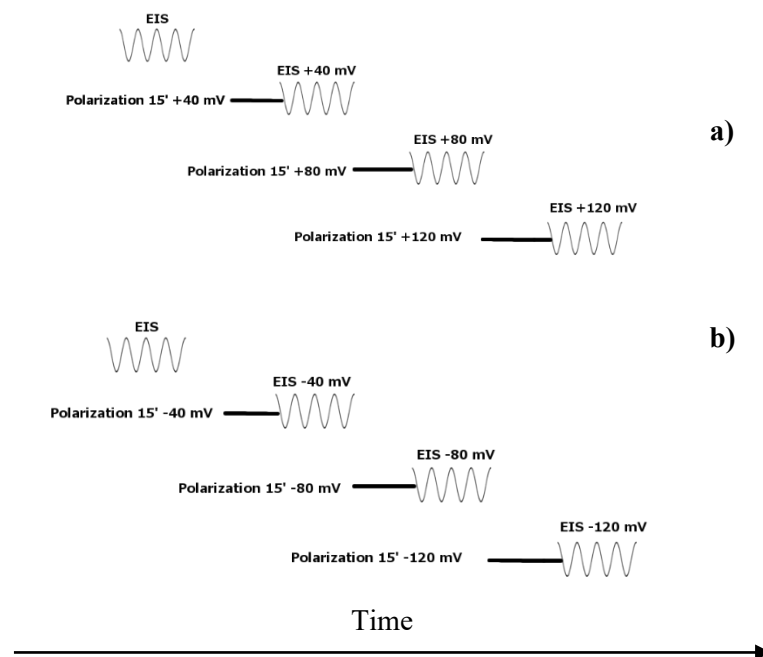


Figure 16 Schema of the chronological sequence of the impedance measurement test at different working electrode potentials a) in the anodic direction, b) in the cathodic direction.

### 2.5.4.3 The effect of convection

In order to have a complete picture of the electrochemical mechanism occurring when the surface is pseudo-passive, the effect of rotation, thus of flow conditions, over the electrochemical reactions was investigated.

The described reference conditions were adopted along with the cell A (Figure 12). A 600 rpm was applied to the working electrode throughout the duration of the test until pseudo-passivation. The flow conditions were the only variation with respect to the scaling conditions adopted so far.

The evolution of the scales until pseudo-passivity was measured with EIS and LPR each three hours. A 6 h rest time was given to the system to reach steady state. OCP was measured in between the techniques.

Once the surface reached a pseudo-passive state, impedance spectra were recorded changing the rotation rate of the working electrode. Keeping the solution conditions stable, the influence of the solution convection was investigated changing the rotation rate from the initial 600 rpm up to 2100 rpm with several steps of 300 rpm. An impedance measurement was performed after each step.

## **2.5.5 Effect of an oxygen contamination**

The experimental methods described in the following section aim to characterize the resistance of the corrosion product layer in the case of small oxygen contamination in the range of hundreds of ppb. Several experimental methods were used to determine to which extent O<sub>2</sub> influences the corrosion behavior.

### **2.5.5.1 Potentiodynamic polarization test with O<sub>2</sub> contamination**

Tafel slope determination was carried out in order to calculate the Stern-Geary coefficient as well as to study the reaction kinetics in a wider potential range. Tafel slope determination can be done only on activation-controlled reactions.

One test was conducted in pseudo-passive conditions and one when the surface was active. A small dissolved oxygen concentration (171 ppb) was added to the reference conditions. The polarization started one hour after oxygen introduction to give O<sub>2</sub> enough time to dissolve into the media. Oxygen was added into the CO<sub>2</sub> gas flow after 4 hours from the exposure to the corrosive solution for an active surface test and after the pseudo-passivation of the surface.

Cell B (Figure 13) was used because of its capacity. Similar chemical conditions were ensured both for anodic and cathodic polarization.

### **2.5.5.2 Oxygen contamination test**

The assessment of the impact of O<sub>2</sub> on the corrosion product layer was performed introducing progressive oxygen concentrations to a pure CO<sub>2</sub> aqueous solution. Cell B was used during this test (Figure 13).

Reference conditions were used with the addition of an O<sub>2</sub> contamination. The contaminants conditions are reported in Table 3. The percentage of oxygen in the gas flow and the relative dissolved oxygen concentration are reported on the left and right column of the table, respectively. The working electrode was exposed to the solution for 5 days. A fixed amount of time was chosen in order to better compare the protectiveness of the layer as a function of the dissolved oxygen concentration.

The evolution of the electrochemical reactions was measured with EIS and LPR each three hours. A 6 h rest time was given to the system to reach steady state. OCP was continuously measured between LPR and EIS measurements.

Table 3 Oxygen contamination used during the test at 80°C.

Oxygen outlet (%)	Dissolved oxygen (ppb)
0	≈ 10 ppb, no added O <sub>2</sub>
0.5	90
1	171
1.5	257

After the test, the working electrode was rinsed firstly with distilled water then with acetone and subsequently dried with compressed air. The samples were conserved under vacuum in a freezer for subsequent surface analysis with SEM and Raman spectroscopy.

### 2.5.5.3 Lower temperature oxygen contamination

As mentioned before, the temperature has a significant impact on the precipitation of a protective corrosion product layer. In particular, higher temperature promotes the precipitation of protective corrosion scales whereas lower temperature conditions result in loosely packed scales and higher corrosion rates. Therefore, the effect of oxygen at lower temperatures was tested to observe the evolution of the scales' protectiveness.

Reference conditions were used, however the temperature was lowered to 60°C. Cell B (Figure 13) was used for this test. The content of oxygen on the test atmosphere was monitored all along with the test and it was kept constant. The tested oxygen concentrations are reported in Table 4.

Table 4 Oxygen contamination used during the test at 60°C.

Oxygen outlet (%)	Dissolved oxygen (ppb)
0.5	116
1.5	348

The test lasted 5 days for comparing the protection outcome of the scales as a function of the contaminant's concentration keeping constant the exposure time.

### 2.5.5.4 Oxygen introduction in pseudo-passive state

Oxygen was introduced at a later stage in order to determine whether oxygen was truly responsible for the anodic potential rise and the localized corrosion features.

Cell B (Figure 13) and reference conditions (Table 2) were used for this test. They obviously changed when O<sub>2</sub> contamination was introduced.

Carbon dioxide was continuously bubbled into the solution to keep it saturated. The samples were exposed to pure CO<sub>2</sub> only until the pseudo-passivation of the surface. At that moment, EIS and OCP values were measured for each working electrode for checking the pseudo-passivity of the surface. Afterward, O<sub>2</sub> was introduced into the cell for reaching a 171 ppb dissolved oxygen concentration. Oxygen was bubbled into the solution along with CO<sub>2</sub> for one day then O<sub>2</sub> feed was suddenly cut and the system was left with CO<sub>2</sub> only for one day.

After the test, the working electrode was rinsed firstly with distilled water then with acetone and subsequently dried with compressed air. The samples were conserved under vacuum in a freezer for subsequent surface analysis with SEM.

### 2.5.5.5 Recovery test

The pit depth was evaluated in order to investigate the effect of oxygen on the pits propagations. Four working electrodes were prepared so to remove them from the electrochemical cell at any given moment.

Cell B was used applying the reference conditions. Of course, the conditions were different when O<sub>2</sub> contamination was introduced.

The test chronological sequence is reported in Figure 17. The first phase consisted of the exposure to pure CO<sub>2</sub> until pseudo-passivation of the surface. Afterward, oxygen contamination of 171 ppb was added for three days, following the contamination feed was suddenly cut. Finally, the working electrodes were exposed again to pure carbon dioxide for four days.

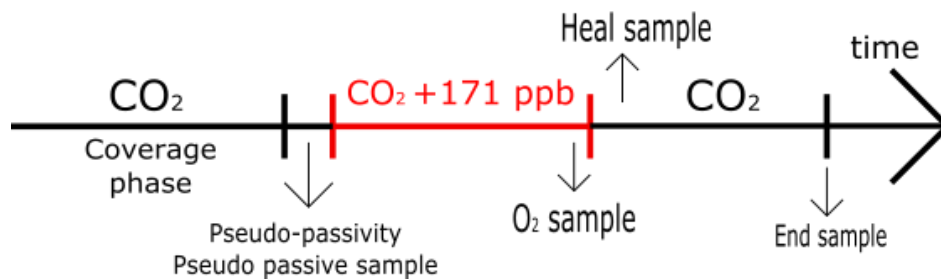


*Figure 17 Chronological test sequence for the pit depth determination after pseudo passivation. Arrows describes the moment when the samples were extracted from the cell for surface analysis. Pseudo passive sample was removed before introducing oxygen, O<sub>2</sub> sample was removed before stopping O<sub>2</sub> feed, Heal sample was removed 24 hours after O<sub>2</sub> feed interruption, finally End sample was removed at the end of the test.*

Throughout the test, the samples were removed at specific moments highlighted in Figure 17. The first one was removed before the introduction of oxygen, the second one just before the stop of the oxygen feed whereas the third and the fourth were removed 24 hours after the interruption of the contamination and at the end of test respectively.

SEM was used for the observation of the corrosion product layer and relative pit-like features. In order to determine the phase that precipitated on the surface, O<sub>2</sub> samples were analyzed with Raman spectroscopy.

Pit depth was measured according to ASTM G46 standard [96]. The samples were pickled with an inhibited acid solution (500 mL HCl, 500 mL distilled water, 3.2 g HMTA). The samples were immersed in the pickling solution and put in an ultrasonic bath for 5 cycles lasting 2 minutes each. After the complete removal of the corrosion product layer, the metallic surface was analyzed with a profilometer for the pit depth measurement. Following the G46 recommendation, the ten most deep pits were considered for the evaluation of the pit propagation.

## 2.6 Experimental conditions summary

### ELECTROCHEMICAL CELLS

Table 5 Summary of the electrochemical cells used in the study

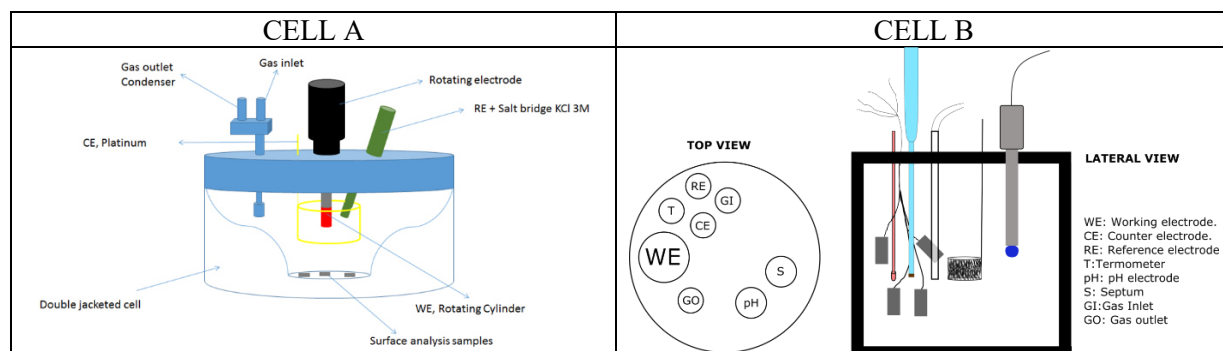


Table 6 Experimental parameters used for identification of reference condition. Dissolved iron setup, static conditions.

Experimental parameters	Values
Temperature	80°C
[NaCl]	2 g/L
pH	6.6
pCO <sub>2</sub>	0.54 bar
Confinement ratio	1.9 cm <sup>-1</sup> / 0.6 cm <sup>-1</sup>
Electrochemical cell	B

Table 7 Protocol for identification of reference condition. Dissolved iron setup, dynamic conditions.

Experimental parameters	Values
Temperature	80°C
[NaCl]	2 g/L
pH	6.6
pCO <sub>2</sub>	0.54 bar
Confinement ratio	1.7 cm <sup>-1</sup>
Electrode rotation	0 rpm – 180 rpm – 600 rpm
Electrochemical cell	A

Table 8 Reference conditions for further investigations on potential, convection and contamination.

Experimental parameters	Values
Temperature	80°C
[NaCl]	2 g/L
pH	6.8
pCO <sub>2</sub>	0.54 bar

Table 9 *Studying the pseudo-passivation protection mechanism, effect of potential.*

Experimental parameters	Values
Temperature	80°C
[NaCl]	2 g/L
pH	6.8
pCO <sub>2</sub>	0.54 bar
Starting time for experimental sequence	24 h / pseudo-passivity
Applied overpotential during EIS	± 40 mV ± 80 mV ± 120 mV vs OCP
Electrochemical cell	A

### EXPERIMENTAL SEQUENCE

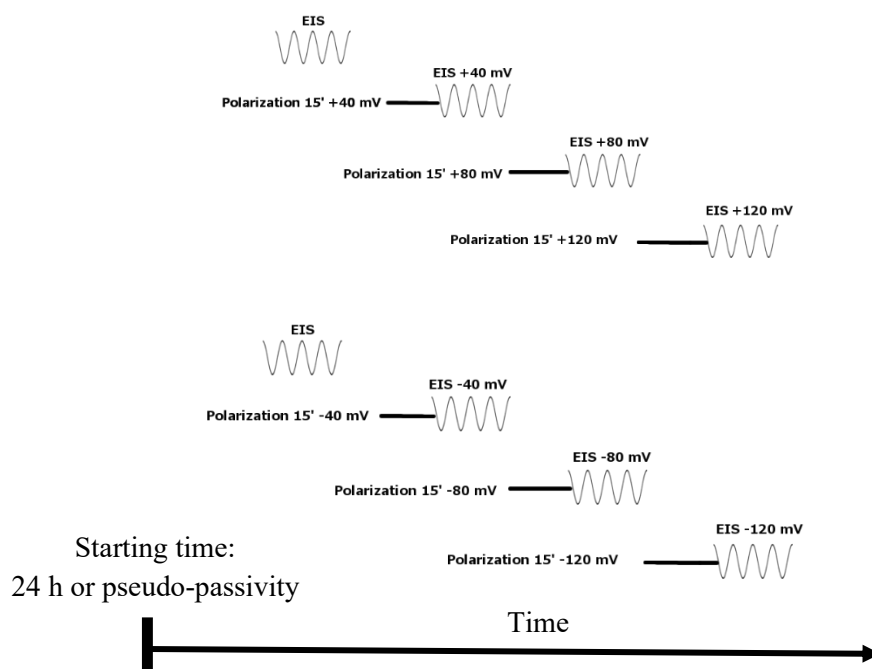
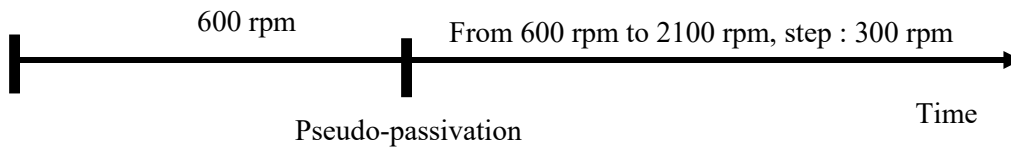


Table 10 *Studying the pseudo-passivation protection mechanism, effect of convection.*

Experimental parameters	Values
Temperature	80°C
[NaCl]	2 g/L
pH	6.8
pCO <sub>2</sub>	0.54 bar
Applied electrode rotation	600 rpm
Change of electrode rotation in pseudo-passive state	From 600 rpm to 2100 rpm with a 300 rpm step
Electrochemical cell	A

*EXPERIMENTAL SEQUENCE*



*Table 11 Oxygen contamination introduced at  $t_0 = 0$  for 5 days.*

Experimental parameters	Values
Temperature	78°C (60°C)
[NaCl]	2 g/L
pH	6.8
pCO <sub>2</sub>	0.54 bar
Exposure time	5 d
Dissolved O <sub>2</sub> contamination	No added O <sub>2</sub> , 90 ppb, 171 ppb, 257 ppb

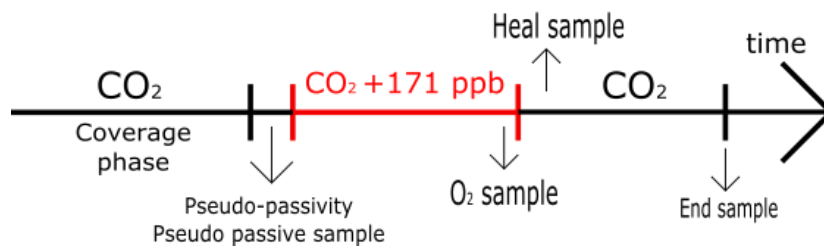
*Table 12 Oxygen contamination introduced in pseudo-passive state.*

Experimental parameters	Values
Temperature	78°C (60°C)
[NaCl]	2 g/L
pH	6.8
pCO <sub>2</sub>	0.54 bar
O <sub>2</sub> introduction time	Pseudo-passivity
Dissolved O <sub>2</sub> contamination	171 ppb

*Table 13 Recovery test.*

Experimental parameters	Values
Temperature	78°C (60°C)
[NaCl]	2 g/L
pH	6.8
pCO <sub>2</sub>	0.54 bar
O <sub>2</sub> introduction time	Pseudo-passivity
O <sub>2</sub> feed stop time	3 days
Dissolved O <sub>2</sub> contamination	171 ppb

*EXPERIMENTAL SEQUENCE*



## *2.7 Conclusions*

The techniques and experimental procedures were detailed in this chapter. Several techniques were adopted for the investigation of the corrosion product layer making possible observations of the evolution of the scales' precipitation and characterization of their morphologies and compositions.

The electrochemical techniques such as LPR and EIS are essential for evaluating the corrosion behavior but they are not sufficient for the investigation of a complex system such as a corrosion product film protecting the surface from further corrosion. Other surface analysis techniques XRD, SEM, Raman spectrometry and profilometry were used for the characterization of the main features of the corrosion product layer.

Besides the investigation techniques, controlled chemical conditions were ensured throughout the tests for all the experiments. A system for fine-tuning the gas impurities inside the electrochemical cell was developed to introduce a well-known quantity of oxygen with the CO<sub>2</sub> flow.

In the following chapters, the results found with the methods described in this chapter are presented. The results are divided in three chapters. The first one deals with the research for a reference condition in order to get a pseudo-passive state, the second one concern the investigation of the pseudo-passive condition with a proposed model for the protective pseudo-passivation mechanism. Finally, the third one is related to the oxygen contamination in the CO<sub>2</sub> saturated solution. Each subsection presents the results first. At the end of each chapter or after significant discussion sections, conclusion will be drawn.

## 3 Identification of a reference condition

### 3.1 Iron buffering method occurred at pH 6.6

Iron carbonate saturation depends on both the concentration of carbonate ions and dissolved  $\text{Fe}^{2+}$  content in the electrolyte. In this section, the saturation value of the corrosive solution was increased by adding iron wool into the electrochemical cell. It was added for accelerating pseudo-passivation of the carbon steel. Iron wool provides a steady source of iron ions into the solution exploiting the natural corrosion of the wool inside the cell. Another way of describing the system is through the confinement ratio *i.e.* the ratio between the exposed active surface and the volume of the solution. The area of the iron wool was calculated by knowing the specific area (area/mass) of the specific iron wool used.

Two confinement ratios ( $1.9 \text{ cm}^{-1}$  and  $0.6 \text{ cm}^{-1}$ ) were investigated in order to determine which one was better for accelerating pseudo-passivation of the scales.

Table 14 Summary of the experimental conditions, iron buffering method - static test

Experimental parameters	Values
Temperature	80°C
[NaCl]	2 g/L
pH	6.6
pCO <sub>2</sub>	0.54 bar
Confinement ratio	1.9 cm <sup>-1</sup> / 0.6 cm <sup>-1</sup>
Electrochemical cell	B

#### 3.1.1 Static conditions.

These results were obtained in the cell B described in Figure 13. The iron wool was placed at the bottom of the electrochemical cell.

At pH 6.6, the evolutions of the open circuit potential and the corrosion rate for two different confinement ratios,  $1.9 \text{ cm}^{-1}$  and  $0.6 \text{ cm}^{-1}$ , are reported in Figure 18.

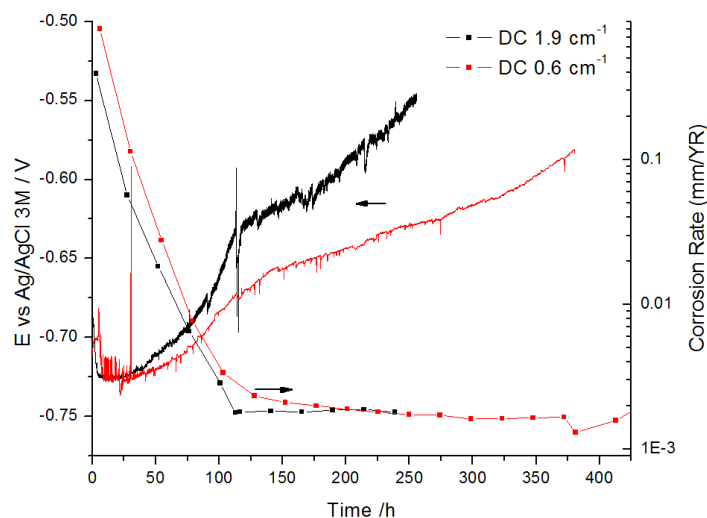


Figure 18 Corrosion potential (solid line) and corrosion rate measurements (square symbols) versus time for the iron wool test (at 80°C pH 6.6 NaCl 2g/L CO<sub>2</sub> saturated aqueous solution). Stern-Geary coefficient used 27 mV/dec.

Both conditions display the sign of pseudo-passivation as reported in the literature [46]. The OCP shifts towards nobler potentials starts after 50 hours. However, with a 1.9 cm<sup>-1</sup> degree of confinement, the rise in potential is sharper. For both confinements, the transition toward a pseudo-passive state occurs after the same time, namely after five days of immersion time. The evolution of the corrosion rate with time is characterized by a progressive decrease, until a plateau is reached. This trend is consistent with the pseudo-passive transition. The value of the corrosion rate on the plateau is similar for both conditions and lasts several days until the end of the test. The final corrosion rate values are quite low in the order of 10<sup>-3</sup> mm/yr displaying a good level of protection.

Table 13 reports the mass losses that the corrosion coupons had during exposure into the solution. In this case, the corrosion rate calculated is slightly superior for the high confinement ratio test. However, they are both in the same order of magnitude. Moreover, the corrosion rate calculated from the LPR measurement and the Stern Geary equation is not dissimilar from the mass-loss measurements, the most part of the mass loss will be concentrated in the exposure time before pseudo-passivity, in this case the first two days. Anyhow integrated corrosion values from the LPR measurements underestimate the corrosion rates value being lower than the ones measured with the simple mass-loss method. However, the use of Stern-Geary relationship for determining the corrosion rate especially when the material is pseudo-passive reveals some critical points that are considered in section 3.4.

*Table 15 Comparison between corrosion rate measurements obtained from the mass loss experiments and determined from LPR measurements.*

Confinement ratio (cm <sup>-1</sup> )	Mass loss corrosion rate (μm/yr)	LPR corrosion rate B=27 mV/dec (μm/yr)
1.9	29.3	21.6
0.6	21.2	15.3

Figure 19 shows top-view backscattered SEM images of the weight loss corrosion samples at different confinement ratios. The micrographs show that for the higher confinement, small monodispersed crystals precipitate on the metal surface whereas a more dispersed size distribution can be observed for the other confinement ratio condition. Nevertheless, for both these conditions, the crystals form a compact film on the metallic surface covering the surface in any spot. The crystals have a clear polyhedral shape and they seem to have a more geometrical form in the higher confinement case. The crystal shape observed is associated with siderite, a crystalline form of iron carbonate. The difference in the dispersion of the crystal size can be related to a higher iron carbonate saturation: for the classical theory of nucleation, a high saturation encourages simultaneous nucleation of the crystals and, therefore, a coherent growth and low size dispersion.

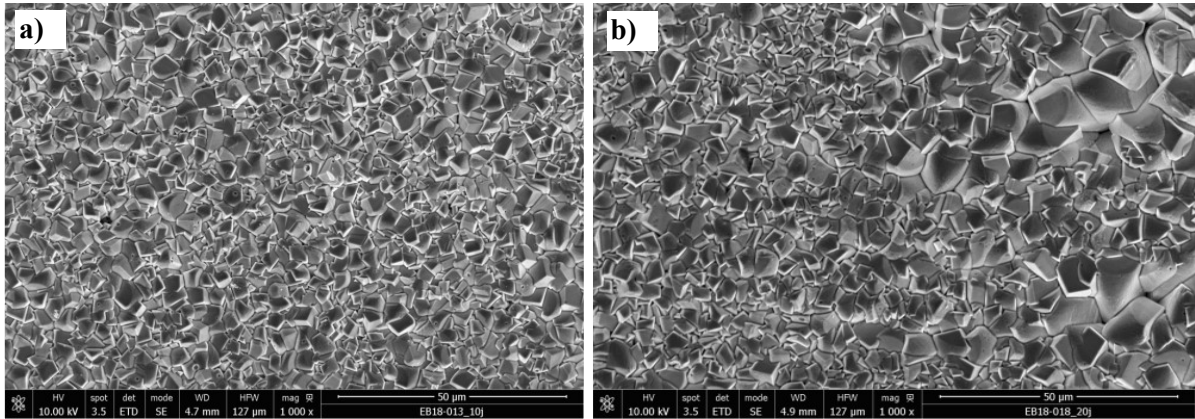


Figure 19 SEM micrographs for scales formed at 80°C pH 6.6 NaCl 2g/L CO<sub>2</sub> saturated aqueous solution at a) 1.9 cm<sup>-1</sup> and b) 0.6 cm<sup>-1</sup> of confinement ratio. The samples were taken at the end of the test in Figure 18.

Cross-section analysis is more adapted for evaluating important parameters such as thickness and the presence of eventual secondary phases. In order to evaluate the thickness and transversal composition of the scales, a cross-section SEM observation was performed (Figure 20). The micrographs show that in both confinement ratio conditions, the corrosion product layer thickness reaches about 10 μm. Moreover, right over the metal surface, there is a deposit of different grey shades (yellow circle) which represents a second phase. Considering previous results in similar condition that phase is probably magnetite Fe<sub>3</sub>O<sub>4</sub> [50]. No continuous secondary phase film is observed, only small scattered greyer spots are present. The microscopic observations highlight that some holes penetrating up to the metal surface, however it seems that iron carbonates have filled and stopped the cracks in the deposit.

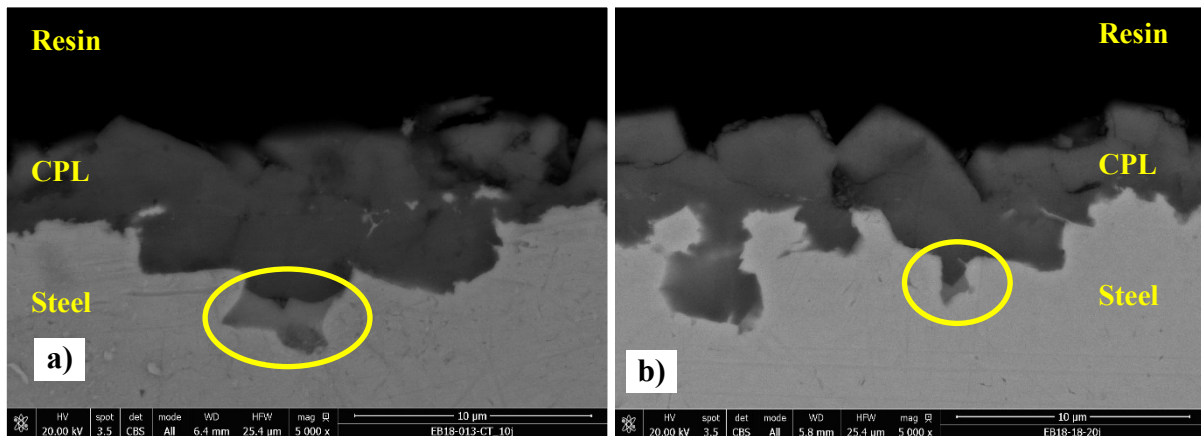


Figure 20 Cross-sections observations of scales formed at 80°C pH 6.6 NaCl 2g/L CO<sub>2</sub> saturated aqueous solution at a) 1.9 cm<sup>-1</sup> and b) 0.6 cm<sup>-1</sup> of confinement ratio. The samples were taken at the end of the test in Figure 18.

GXRD diffraction analysis was performed on the corrosion product layer of one of the corrosion coupons immersed into the electrochemical cell. Figure 21 shows that the only two crystallographic phases detected on the metal surface are iron and siderite in accordance with the SEM images (Figure 20). The traces of other phases that were detected with the back-scattered SEM between the siderite layer and metal substrate were not identified with XRD. This result supports the fact that siderite only

provides protection from the corrosive solution as the secondary phase does not form a continuous layer at the interface between the carbon steel and the siderite layer.

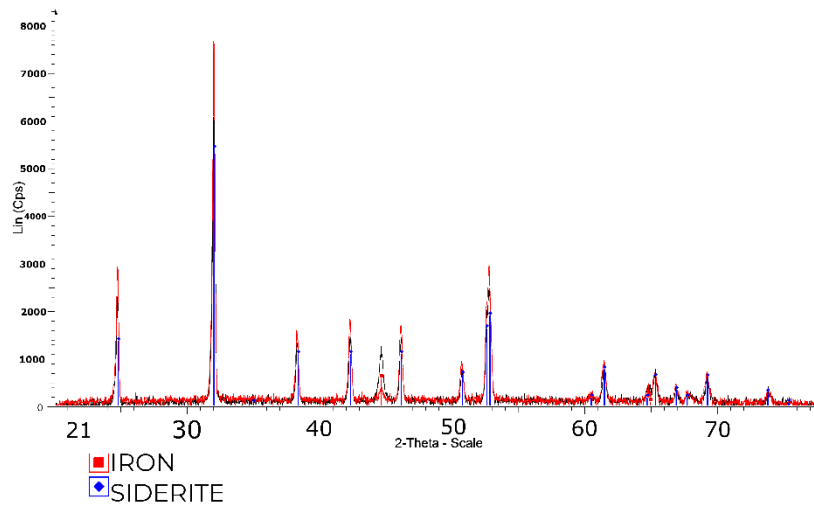


Figure 21 XRD analysis formed at 80°C pH 6.6 NaCl 2g/L at 1.9 cm<sup>-1</sup> (black) and 0.6 cm<sup>-1</sup> (red) of confinement ratio at the end of the test in Figure 18.

Figure 22 displays the Nyquist plots of the impedance spectra recorded as a function of the exposure time for the two confinement conditions. At the beginning of the experiment, the Nyquist diagrams evolve from a single semicircle (after 30 h) to a straight line (after 100 h). Bode diagrams display the evolution of the phase of the impedance as a function of the potential oscillation frequency (Figure 23). A unique time constant is observed, for example after 30 h. Afterward, a time constant appears in the low frequency part whereas the original time constant gradually shifts towards a higher frequency, for example after 120 h. The rise of the second time constant is concomitant at low frequency with the pseudo-passive transition pointing out that the two phenomena are correlated.

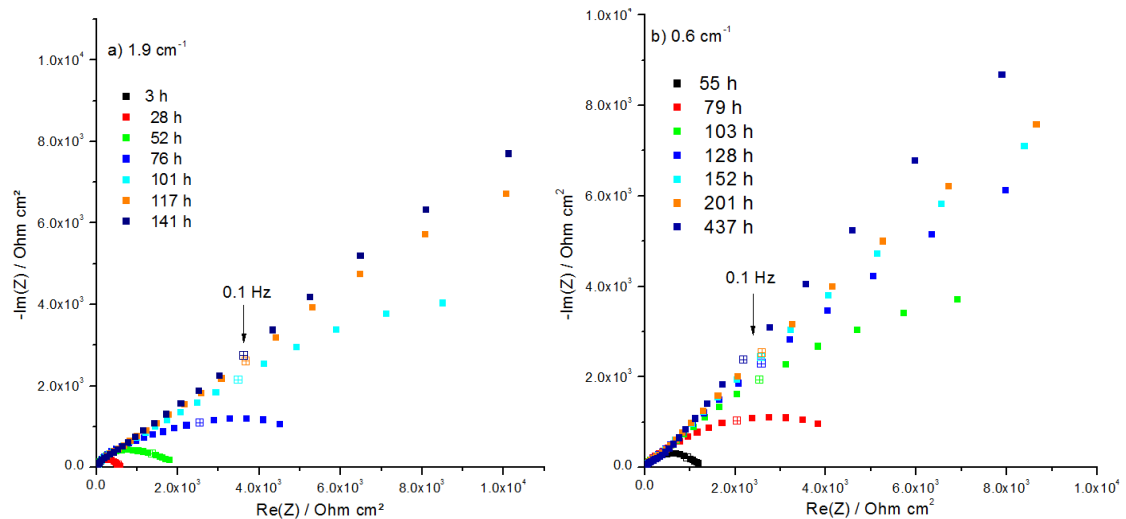


Figure 22 Nyquist plots of the impedance measurements during time at 80°C in the electrolyte (pH 6.6 NaCl 2g/L CO<sub>2</sub> saturated aqueous solution) for a) 1.9 cm<sup>-1</sup> and b) 0.6 cm<sup>-1</sup> confinement ratio.

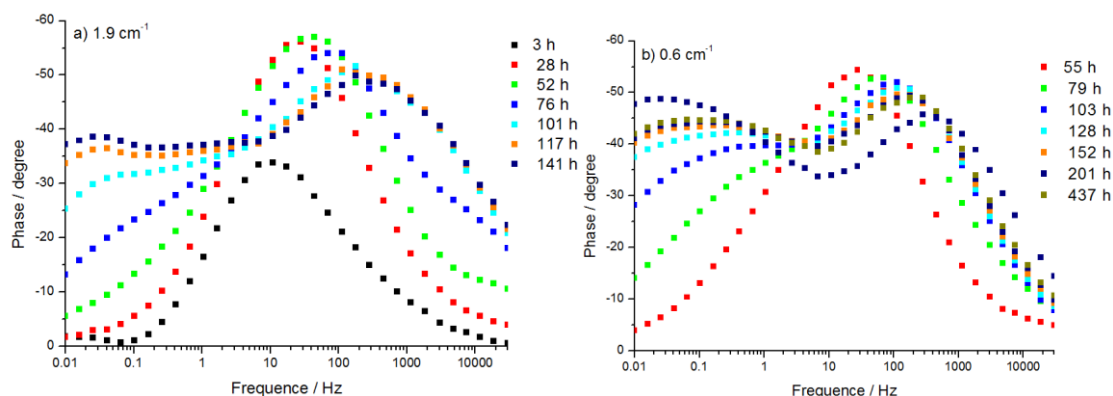


Figure 23 Bode impedance diagrams obtained at corrosion potential during time for the carbon steel in the saturated aqueous solution (pH 6.6 NaCl 2 g/L CO<sub>2</sub>, 80°C) for: a) 1.9 cm<sup>-1</sup> and b) 0.6 cm<sup>-1</sup> of confinement ratio.

The results presented so far on the iron buffering method for accelerating iron carbonate precipitation are promising. Both confinement ratio conditions presented a quick pseudo-passivation in a few days. The higher confinement ratio showed a sharper transition; therefore, this condition was selected for further experimentation.

In order to investigate the capability of this method to produce pseudo-passive scales in dynamic conditions, the cell A (Figure 12) with a rotating electrode was used. First, tests were performed in the static conditions. Afterwards flow conditions were tested applying a rotation rate to the working electrode (180 rpm and 600 rpm). In the following section of the chapter the results concerning dynamic conditions test will be reported.

### 3.1.2 Iron buffering method, dynamic conditions.

Once the two confinement ratios have been tested in static conditions, the same parameters were applied in cell A for the investigation in controlled flow conditions with a rotating electrode. The need for investigating dynamic condition arises from operative conditions of certain industrial plant part such as pipelines for geothermal water transport. This section will start with a first test without rotation to observe if pseudo-passivation is achieved even using a different cell with a smaller cell volume. Afterwards other tests were performed applying a rotation to the working electrode (180 rpm, 600 rpm).

Table 16 Summary of the experimental conditions, iron buffering method - dynamic conditions

Conditions	Values
Temperature	80°C
[NaCl]	2 g/L
pH	6.6
pCO <sub>2</sub>	0.54 bar
Confinement ratio	1.7 cm <sup>-1</sup>
Electrode rotation	0 rpm – 180 rpm – 600 rpm
Electrochemical cell	A

### 3.1.2.1 Experiments without rotation of the electrode.

The results of two tests at pH 6.6 with the rotating electrode electrochemical cell adding iron wool ( $1.7 \text{ cm}^{-1}$  confinement ratio) to the test solution and under static conditions are reported in Figure 24.

The confinement ratio depends on the solution volume introduced into the cell. The solution volume is controlled only approximately when the solution is transferred from the preparation bottle to the electrochemical cell. Consequently, the confinement ratio can be calculated only at the end of the test measuring the solution volume. This is the reason because the confinement ratio was  $1.7 \text{ cm}^{-1}$  and not  $1.9 \text{ cm}^{-1}$  in the previous test. The adopted experimental procedure can only set the confinement value approximately.

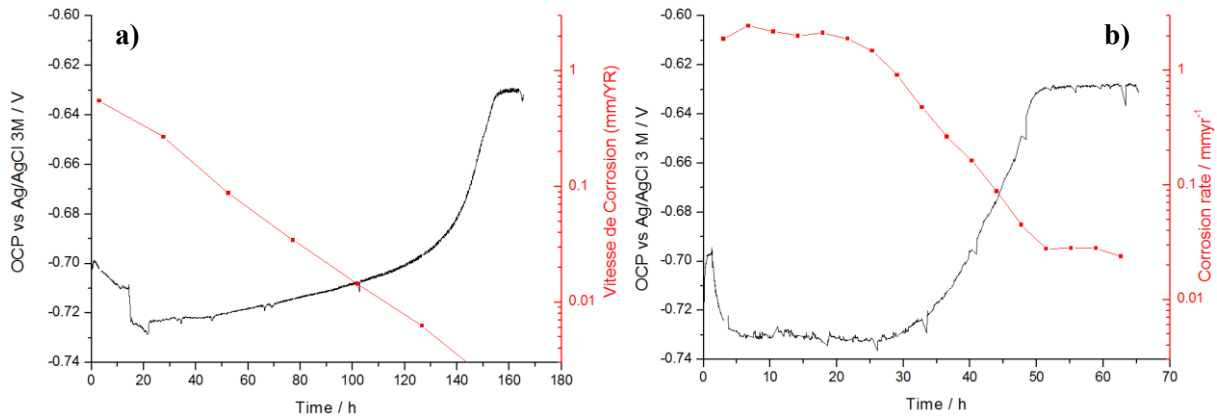


Figure 24 Open circuit potential and corrosion rate measurements of corrosion samples in a 2 g/L NaCl, pH 6.6,  $1.7 \text{ cm}^{-1}$   $\text{CO}_2$  saturated aqueous solution. Test conducted with the rotating cylinder electrochemical cell in static conditions. Two replicas are shown in a) and b).

A sudden rise of the OCP is observed after 48 or 140 hours. As previously reported, the rise in OCP is between 80 and 100 mV. The time needed for reaching the pseudo-passive state is five days in one case and two days in the second one. These results highlight that the time needed for reaching the pseudo-passive state is not constant even in the same conditions. Unfortunately, this effect makes it hard to foresee the moment when the surface becomes pseudo-passive even if the impedance, reported in Figure 25, can help in the observation of the evolution of the protectiveness of the scales.

Similar to the situation in Figure 22, in the first two days, the Nyquist plot shows multiple semi-circles that progressively increase their diameter (Figure 25 a) after 53 h for example). Subsequently, a strong imaginary contribution arises in concomitance with the rise in potential. This contribution makes Nyquist plot to become linear similarly to a Nyquist plot of a diffusion limitation reaction (Figure 25 b) after 151 h for example).

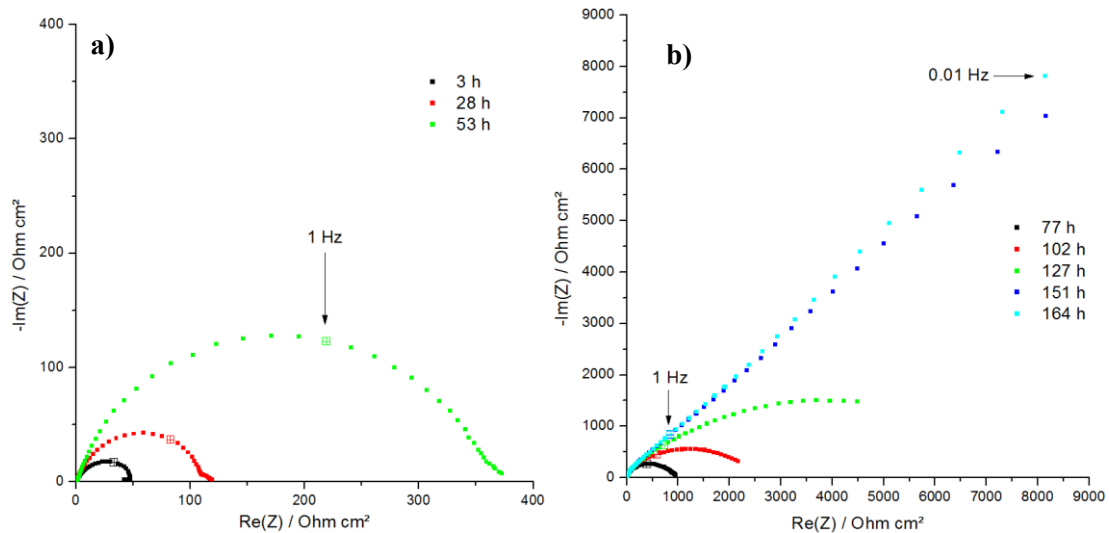


Figure 25 Nyquist plots collected for the rotating cylinder electrochemical cell in static conditions at 80°C pH 6.6 NaCl 2g/L 1.7 cm<sup>-1</sup> CO<sub>2</sub> saturated aqueous solution at a) short exposure time and b) long exposure time. The impedance measurements are referred to the test in Figure 24 b).

SEM images related to the first test at 0 rpm shows that the carbon steel surface is well covered by a corrosion product layer that protects the surface. However, the crystal size looks less monodispersed than the scales observed in the previous section (Figure 26).

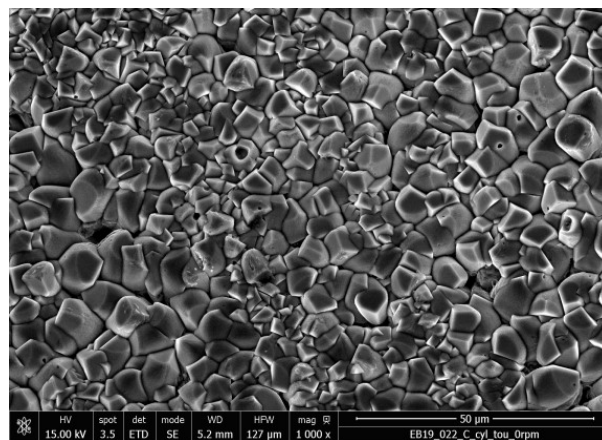


Figure 26 Corrosion product layer formed on the working electrode at pH 6.6, 80°C, confinement ratio 1.7 cm<sup>-1</sup> and salt concentration 2 g/L. Pictures taken at the end of test in Figure 24 a).

The results in this section show that pseudo-passivation is possible using a different electrochemical cell, with different volume and geometry, in static conditions. In fact, dynamic conditions mimic better operative conditions of certain industrial conditions. Moreover, a quick pseudo-passivation is needed for observing the effect of convection on the electrochemical reactions before and after pseudo-passivation. In the following sections, a rotation was applied to the electrode in the same conditions in order to investigate whether protective scales could precipitate in dynamic conditions with this set-up (cell A, Figure 12). Firstly, a 180 rpm rotation speed was applied, in a second test the rotation rate was increased to 600 rpm.

### 3.1.2.2 Experiments with 180 rpm rotation

Still, the OCP measurements displayed in Figure 27 show a 80 mV potential rise in open circuit potential conditions after around 300 h. This rise in OCP highlights the pseudo-passivation of the surface.

NB: on Figure 27 the usual LPR corrosion rate is missing due to data acquisition problems with the potentiostat.

Regarding impedance measurements, the rise of OCP that characterizes enhanced protection supplied by the scales, is still strongly connected to the appearance of a linear tail in the low frequency part of the impedance spectra as Figure 28 illustrates.

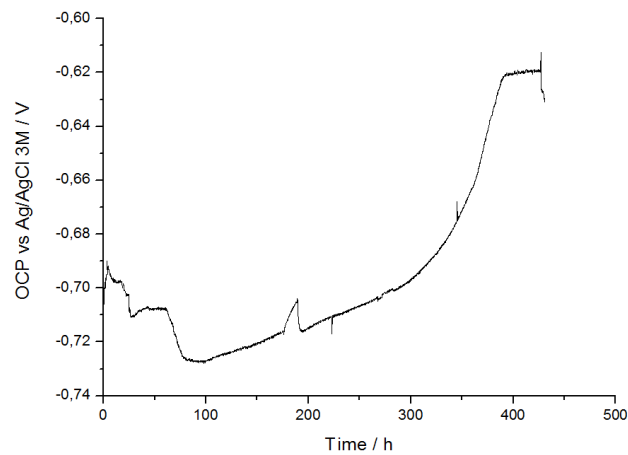


Figure 27 OCP evolution for the carbon steel rotating cylinder (180 rpm) versus time in the 80°C pH 6.6 NaCl 2g/L CO<sub>2</sub> saturated aqueous solution and for 1.7 cm<sup>-1</sup> confinement ratio.

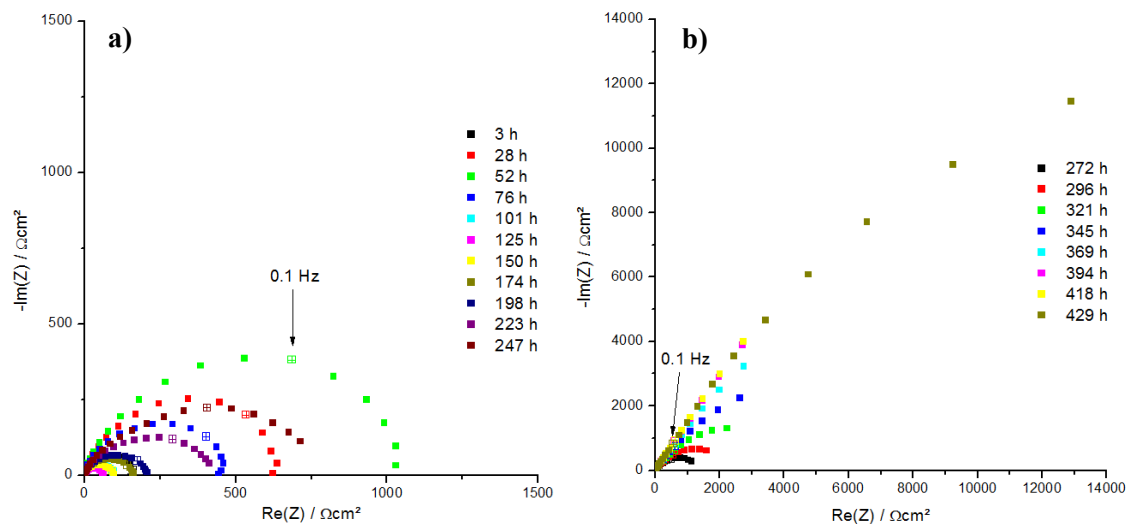


Figure 28 Nyquist plots collected for the rotating cylinder electrode during time at a pseudo-passive surface and in the 80°C pH 6.6 NaCl 2 g/L (confinement ratio 1.7 cm<sup>-1</sup>) CO<sub>2</sub> saturated aqueous solution at a) short exposure times and b) long exposure times.

The electrochemical impedance diagrams obtained for a rotation speed of 180 rpm tests are described by a first increase of the diameter of the Nyquist semicircle that later decreases after the fourth day probably because of an instability of the solution chemistry. Afterward, the diameter of the loop increases steadily throughout the test up to the moment where the low frequency part of the spectra is defined by a straight line. This new time constant becomes more evident starting about after 336 h of exposure time. In this case, a greater rotation rate seems to delay the moment when the corrosion product layer reaches a more protective state. Anyway, the features that are observed in static conditions are re-encountered in the same way at 180 rpm highlighting that pseudo-passivation is still possible in this condition.

Pseudo-passivation was reached even applying a 180 rpm however the time needed for getting pseudo-passive scales is very long taking more than two weeks of exposure time. The same solutions and electrochemical cell parameters were reused with a higher electrode rotation rate: 600 rpm.

### 3.1.2.3 Experiments with 600 rpm rotation

The results obtained when the working electrode rotates at 600 rpm behave similarly to the ones reported in the previous paragraph at 180 rpm. The results are reported in Figure 29 (OCP), Figure 30 and Figure 31 (EIS).

Figure 29 displays a pseudo-passive transition with a sharp increase of the potential of around 80 mV after two weeks of exposure to the corrosive solution.

NB: On Figure 29 the usual LPR corrosion rate is missing due to data acquisition problems with the potentiostat.

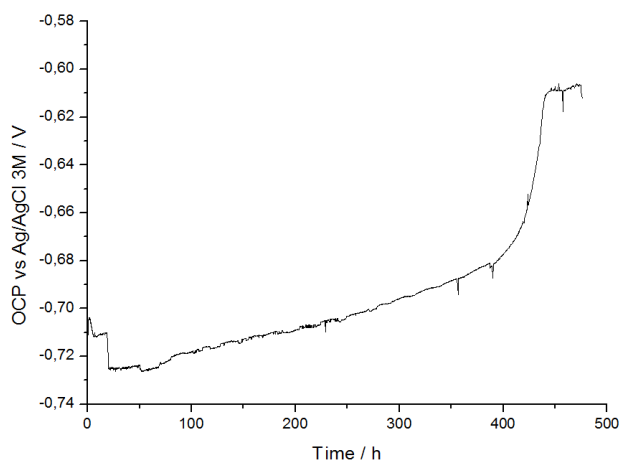


Figure 29 OCP evolution for the carbon steel rotating cylinder (600 rpm) versus time in the 80°C pH 6.6 NaCl 2g/L 1.7 cm<sup>-1</sup> CO<sub>2</sub> saturated aqueous solution.

At the same time, both the Nyquist plot and Bode plots show that a second time constant at low frequency appears with the time of immersion into the corrosive solution (Figure 30 and Figure 31). Particularly, the Nyquist plot shows that a linear tail is present just after the pseudo-passivation of the surface. The bode plot shows that at low immersion time, only one time constant at medium frequency is present. For higher immersion time, a new time constant at low frequency appears whereas the one at medium frequency slightly shifts towards higher frequencies.

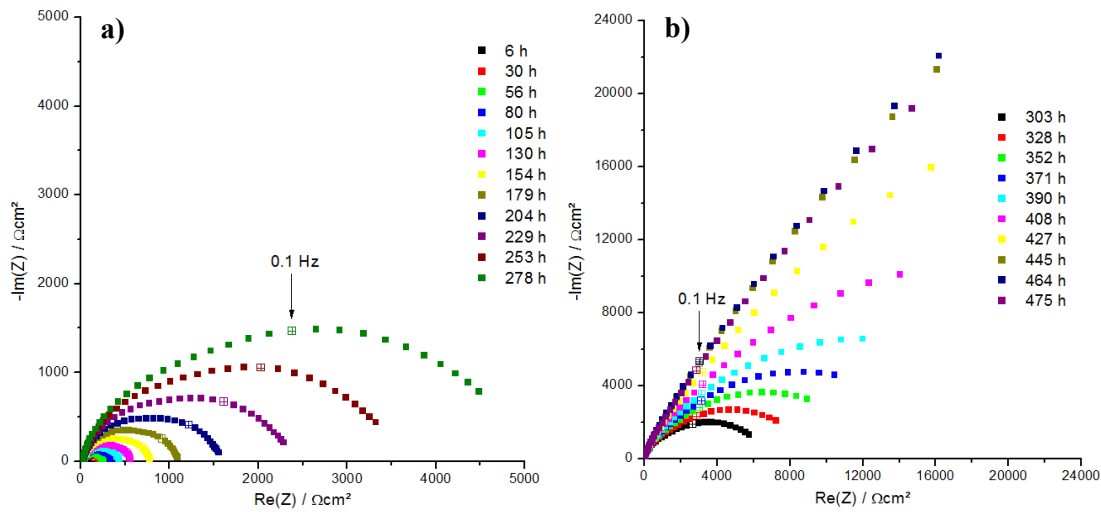


Figure 30 Nyquist plots collected for the carbon steel rotating cylinder at 600 rpm in the  $80^{\circ}\text{C}$  pH 6.6, NaCl 2 g/L,  $\text{CO}_2$  saturated aqueous solution and for a  $1.7\text{ cm}^{-1}$  confinement ratio: a) short exposure times and b) long exposure times.

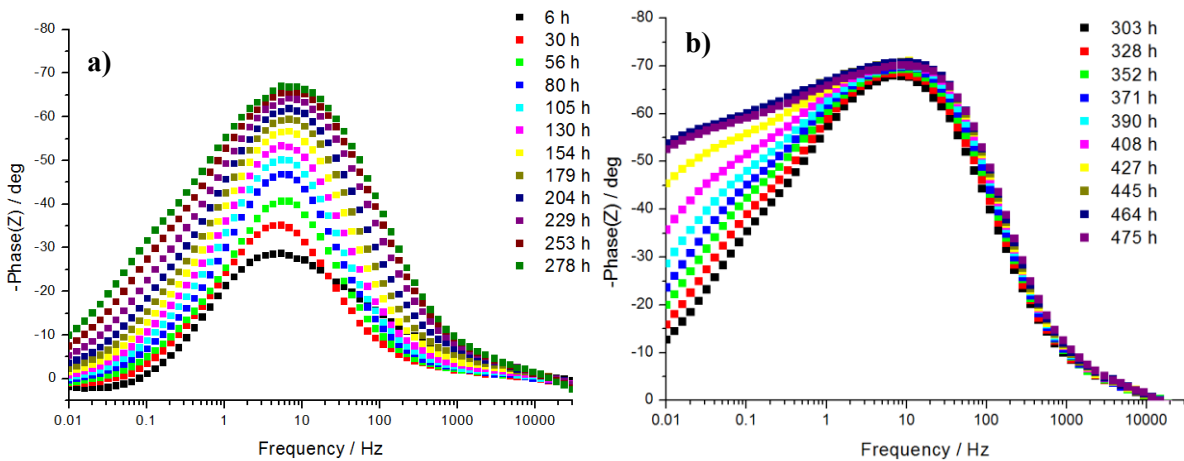


Figure 31 Bode plots collected for the carbon steel rotating cylinder at 600 rpm in the  $80^{\circ}\text{C}$  pH 6.6 NaCl 2g/L  $\text{CO}_2$  saturated aqueous solution and for a  $1.7\text{ cm}^{-1}$  confinement ratio: a) short exposure times and b) long exposure times.

Finally, it appears that the rotation rate has no effect on the nature of the phenomenon because the features of the electrochemical measurements look the same. The time needed for the pseudo-passivation of the system was longer at 600 rpm than at 180 rpm rotation. However, there is no sufficient evidence to claim a delaying effect of the convection over the pseudo-passivation of the surface. The time needed for the surface to reach a pseudo-passive state remains hard to estimate with the electrochemical techniques used in this section.

The objective was to find a condition that could result in pseudo-passive scales regularly and as quick as possible. This need is explained by the aim of investigating the protection mechanism being in the same protectiveness and system conditions. Pseudo-passivity was chosen as a starting point for

verifying the properties of protective scales because it is easy to detect and the corrosion rates are low and similar.

Pseudo-passivation was accelerated using iron wool in the cell in order to increase the iron carbonate precipitation rate. The tests in static conditions resulted in quick pseudo-passivation, therefore the same conditions were tried in dynamic conditions applying a rotation to the working electrode.

The result reveals that in dynamic conditions pseudo-passivation is achieved too slowly. Moreover, the system conditions cannot be controlled continuously as the iron wool presence could interfere in the presence of oxygen making the interpretation of the contamination results ambiguous. Therefore, the iron buffering method for increasing iron carbonate precipitation rate was discarded.

In order to accelerate iron carbonate precipitation, a new method was tested where no iron wool was present in the electrochemical cell. The acceleration of iron carbonate precipitation rate and thus pseudo-passivation was achieved raising the pH to 6.8 so to increase the equilibrium concentration of the dissolved carbonate ions.

### 3.2 Experiments at pH=6.8, static electrode

Because of the unsatisfactory results with the iron wool inside the electrochemical cell, a different strategy for ensuring the solution supersaturation was adopted. Namely, the pH was raised to 6.8 to increase the carbonate ion speciation in the solution. In this section the results with these parameters in dynamic conditions are omitted. They are reported in section 4.2 because they are more pertinent for the understanding of the pseudo-passive protection mechanism.

Reference conditions are used with different cells. In this section the results were obtained with cell A.

Table 17 Summary of experimental conditions – higher pH conditions

Experimental parameters	Values
Temperature	80°C
[NaCl]	2 g/L
pH	6.8
pCO <sub>2</sub>	0.54 bar

Figure 32 reports an example of the pseudo-passivation results obtained during exposure to a pH=6.8 CO<sub>2</sub> saturated water solution at 80°C with a 2 % dissolved NaCl without any iron wool addition.

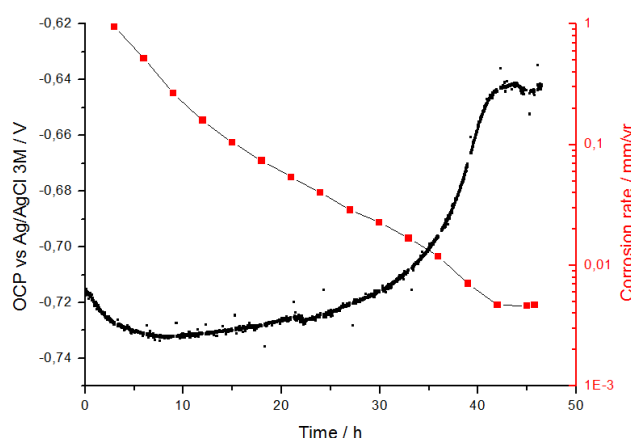


Figure 32 Evolution of OCP and corrosion rate for the carbon steel in the 80°C pH 6.8 NaCl 2 g/L CO<sub>2</sub> saturated aqueous solution, static conditions.

The results show that a pseudo-passive state is reached quite rapidly as the OCP rise between 35 and 45 hours of exposure to the corrosive solution. Similarly, the LPR corrosion rate decreases almost exponentially until pseudo-passivation occurs. After the transition (at around 40 h of immersion) the measured corrosion current reaches a plateau of 5 μm/yr. The pseudo-passivation is also observable in the impedance diagram in Figure 33 and Figure 34. In fact, once more, a second time constant develops at low frequency particularly after the pseudo-passivation of the surface. These results are in line with those observed in adding iron wool into the electrochemical cell.

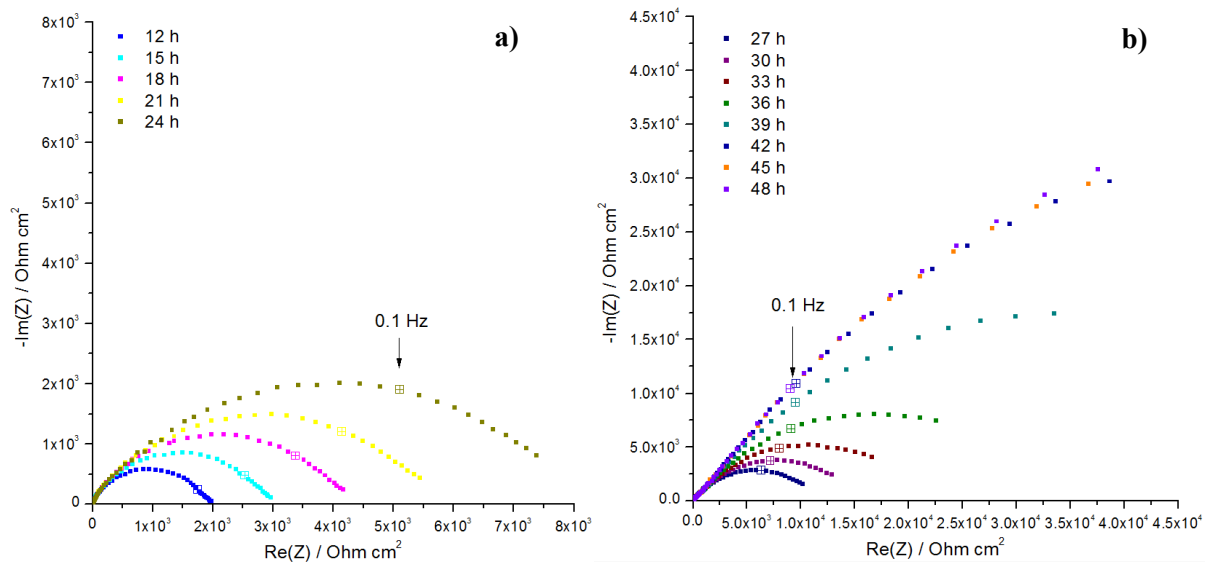


Figure 33 Nyquist impedance diagrams obtained for the carbon steel during time in 80°C pH 6.8 NaCl 2g/L CO<sub>2</sub> saturated aqueous solution in static conditions and without iron wool: a) short exposure times and b) long exposure times.

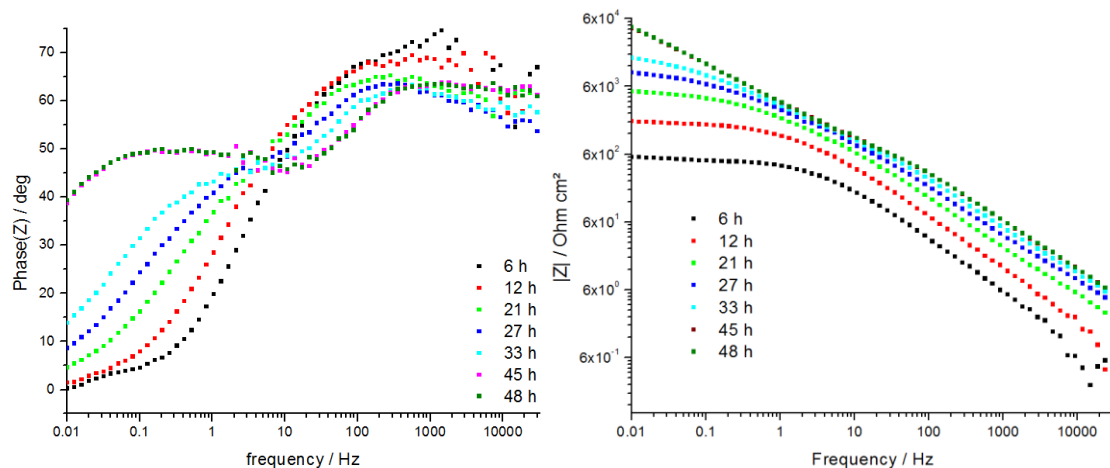


Figure 34 Adjusted impedance measurements from electrolyte resistance, obtained for the carbon steel during immersion time in 80°C pH 6.8 NaCl 2g/L CO<sub>2</sub> saturated aqueous solution, static conditions. Bode representation (phase in the left and impedance modulus in the right, as a function of the frequency).

These conditions result in pseudo-passivity after a reasonable amount of time keeping a continuous control of the corrosive solution. However, as already reported before in the previous cases, there is some variability in the time needed to reach pseudo-passivation (namely a time frame ranging from two to ten days). Anyhow, those conditions result regularly in pseudo-passivation. These satisfactory results at pH 6.8 allow to adopt them for further investigations on the nature of the corrosion product layer and on their protection mechanism on a pseudo-passive state.

### 3.3 *The onset of pseudo-passivation*

In this section the electrochemical parameters that identify the onset of pseudo-passivation will be discussed. Furthermore, the impact of pseudo-passivation on the assumption of the used electrochemical techniques will be discussed.

Considering the onset of pseudo-passivation, the all the tests behave similarly. In fact, a sudden rise in potential occurs in all the tested conditions. Moreover, the gap between initial and final potential is in the order of 100 mV. Similarly, the corrosion rate obtained through the linear polarization resistance and the Stern-Geary relationship keeps decreasing until it reaches a plateau when the material is in a pseudo-passive state. Considering the Nyquist impedance diagram, a progressive increase of the diameter of the capacity loop is observed probably due to the crystals physically blocking the metal surface thus decreasing the surface-active area. Finally, the impedance evolved into two-time constants with the appearance of a low frequency time constant. This characteristic evolution of the Nyquist diagrams is typical of the evolution of the scales because all our experiments that will be reported in the following chapters show the same progression of impedance spectra and the appearance of a low frequency time constant at the same time than the rise of the open circuit potential. A mechanism trying to explain, before and after pseudo-passivation, the evolution of the impedance measurements and the impedance results will be proposed in the section “4.4 Modeling scales protectiveness before and after pseudo-passivation”.

The appearance of the second time constant proves that the reaction at the surface is not a simple mono electronic charge transfer mechanism, therefore the assumption of the Stern-Geary relation no longer applies (Figure 22). This aspect is quite critical for the determination of the corrosion rate. In fact, the polarization resistance measured by LPR technique can be assimilated to the faradic impedance when the frequency tends to 0 Hz.

Considering the Nyquist diagrams in pseudo-passive states and in the transition zone, the impedance points at low frequency display a non-negligible imaginary part. Assuming that the second time constant represents a diffusion phenomenon occurring at the metal surface, the polarization resistance includes both the charge transfer and the diffusion resistance taking into account the whole corrosion process rate. Anyhow the LPR technique and the related Stern-Geary relation may be used to estimate the corrosion rate. However, even in the case of estimation of this parameter, the Stern-Geary coefficient must be taken into account in order to determine the actual corrosion rate. The coefficient depends on the Tafel slopes of the anodic and cathodic reactions involved in the corrosion process. Those values are expected to change during the formation of the corrosion product layer, as suggested by the EIS results, thus affecting the evaluation of the corrosion rate which can yield incorrect results especially in the transition region between a partially covered surface and a mass-limited process. When the scales have a coverage effect, a normal potentiodynamic polarization would reveal the anodic and cathodic Tafel slopes. Contrarily, for the steel in a pseudo-passive state, a correct evaluation of the Stern Geary coefficient would be impossible since the extent of the active surface is unknown.

### 3.4 *The choice for a reference condition*

In this section the experimental conditions used for obtaining a protective corrosion product layer will be discussed. The objective is to select a reference condition to be used for investigating both pseudo-passivation mechanism and the effect of an oxygen contamination in the system.

The static series of experiments aimed to verify the implementation of iron wool into the electrochemical cell in order to accelerate the formation of the corrosion product layer and pseudo-passivation through a high dissolved  $\text{Fe}^{2+}$  and thus iron carbonate supersaturation.

First of all, the experimental conditions in which the iron wool is used have to be discussed. Concerning the quantity of iron wool inside the cell, the surface to mass ratio was determined for each iron wool batch measuring the diameter of several wires that form the iron wool. A cylindrical shape was assumed for each cylinder in order to calculate the surface to mass ratio. The dispersion of diameter measure of iron wool is low, 3  $\mu\text{m}$  on an average diameter of 42  $\mu\text{m}$ . Therefore, good reproducibility of surface to mass ratio is assured. The iron wool was well immersed into the electrolyte both for the classical (cell B, Figure 13) and rotating electrode electrochemical cells (cell A, Figure 12). There was no control of the  $\text{Fe}^{2+}$  released into the solution by the iron wool because it did not undergo any electrochemical measurement. Therefore, the supersaturation value may not have been constant during the whole test. Moreover, the presence of free iron ions in the solution leads to the precipitation of iron carbonates directly inside the bulk solution as well as on the corroding surface.

Considering the tests carried out in dynamical conditions at 180 rpm and 600 rpm, the open circuit potential (Figure 27 and Figure 29) rises linearly for more or less 300-400 hours then once again a sudden rise in OCP occurs which is concomitant with the appearance of a second time constant in the same way of the static test (Figure 28). Under the dynamic conditions, the iron wool does not give satisfactory results because the time needed for pseudo-passivating is too long.

Finally, the use of iron wool was questioned in relation to the addition of oxygen as a contaminant in the gas atmosphere. In fact, a great corroding surface into the electrochemical cell may give rise to relevant system perturbation such as an uncontrolled consumption of oxygen in the cathodic reaction. The buffering effect of the carbonic acid/sodium bicarbonate is probably perturbed by the reactions due to the presence of iron wool because of the great confinement ratio that produces iron carbonate precipitation in the solution. In fact, the pH had to be adjusted with the corrective solutions several times. These observations related to uncontrolled solution chemistry supported the exclusion of this method for accelerating iron carbonate precipitation. An incomplete control of the solutions parameters would make the result with any contaminations (oxygen in this case) more ambiguous.

Accelerating iron carbonate precipitation using iron wool inside the cell proved to be a complex mechanism. Furthermore, pseudo-passivation was not achieved quickly especially when a rotation was applied to the electrode. Another method for accelerating iron carbonate precipitation was then sought. A simpler solution involving an increase of the bulk pH (6.8) was selected in order to attain a greater supersaturation, thus more favorable conditions for a protective corrosion product layer. These conditions resulted in a quick pseudo-passivation keeping the system simple and the solution chemistry well controlled throughout the entire duration of the test. A confrontation summary between the different conditions is reported below.

Table 18 Summary of the advantages (pros) and disadvantages (cons) of the experimental methods

pH 6.6 iron wool pros	pH 6.6 iron wool cons	pH 6.8 pros	pH 6.8 cons
Quick pseudo passivation in static conditions	Slow pseudo-passivation in dynamic conditions	Quick pseudo-passivation in static and dynamic conditions	Pseudo-passivation time fluctuates
Sharp transition to pseudo-passivity	Confinement ratio is hard to set	Constant solution chemistry, easy to predict	

Therefore, the conditions that are re-reported for the sake of explanation in the table below were adopted as reference conditions. Starting from these parameters the protectiveness mechanism of pseudo-passivation was investigated varying the electrode potential, the flow conditions and the solution chemistry with the addition of oxygen.

Table 19 Selected reference conditions.

Experimental aparameters	Values
Temperature	80°C
[NaCl]	2 g/L
pH	6.8
pCO <sub>2</sub>	0.54 bar

Unfortunately, pseudo-passivation fluctuates between 2 and 10 days even with these conditions.

The results of this chapter are necessary to the achievement of the following ones. The next chapter will deal with the protectiveness mechanism of pseudo-passivation and its modeling.

## 4 Studying the “pseudo-passivation” protection mechanism

This chapter deals with the protectiveness of the pseudo-passive state. Particularly the evolution of the corrosion scales that leads to pseudo-passivity and the probable reasons explaining why pseudo-passivity is so protective is discussed. This evolution was detected with OCP and electrochemical impedance measurements throughout the exposure time to the CO<sub>2</sub> aqueous solutions. The effect of the potential and the solution flow velocity was evaluated in the active and pseudo-passive states for understanding the key electrochemical features of the anodic and cathodic reactions.

The conditions for which these investigations were carried out are limited to the ones that are needed to reach a quick pseudo-passivation of the surface. The reference conditions that were identified in the previous chapter were used for the investigations in this chapter (pH=6.8 and T=80°C), therefore no iron wool was used for this experiment simplifying the system. Changing flow conditions and electrode overpotential is motivated by the need of experimental observations to model the change in electrochemical reactions before and after pseudo-passivity. The change in potential aims to observe the kinetics of the reaction particularly whether they still are controlled by activation. Flowing conditions were applied to determine if higher diffusion rate of reagents to/from the electrode impact pseudo-passivity and general scales protectiveness.

Thus, the chapter is divided into three sections. In the first one, different applied overpotentials are used in order to investigate the properties of a pseudo-passive corrosion product layer (in static conditions) whereas the second part concerns the flow conditions variations on the pseudo-passivity. Finally, a model explaining why the surface becomes pseudo-passive is proposed based on the results of the previous section.

### *Summary of the experimental conditions*

*Table 20 Experimental conditions for the potentiodynamic polarization test*

Conditions	Values
Temperature	80°C
[NaCl]	2 g/L
pH	6.8
pCO <sub>2</sub>	0.54 bar
Start of polarization	5 hours
Electrochemical Cell	B

*Table 21 Experimental conditions for investigating the effect of potential*

Conditions	Values
Temperature	80°C
[NaCl]	2 g/L
pH	6.8
pCO <sub>2</sub>	0.54 bar
Starting time for experimental sequence	24 h / pseudo-passivity
Applied overpotential during EIS	± 40 mV ± 80 mV ± 120 mV vs OCP
Electrochemical cell	A

### Experimental sequence

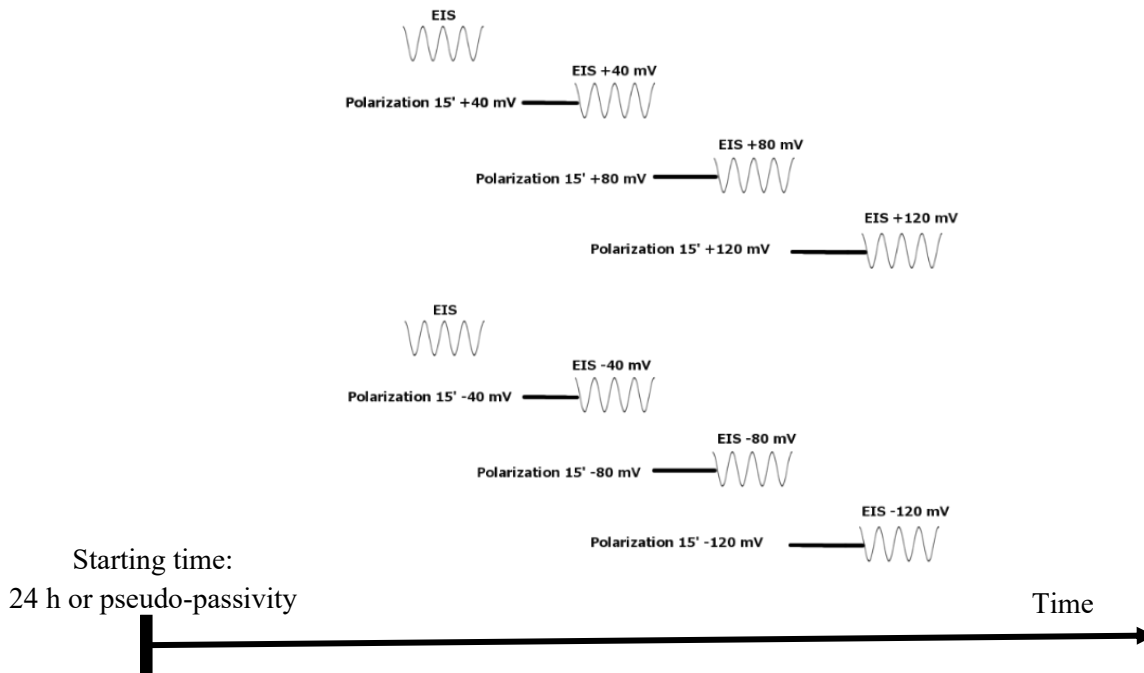
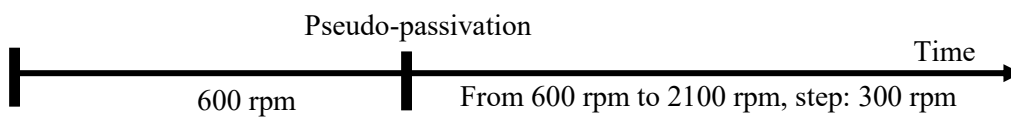


Table 22 Experimental conditions for investigating the effect of convection

Conditions	Values
Temperature	80°C
[NaCl]	2 g/L
pH	6.8
pCO <sub>2</sub>	0.54 bar
Applied electrode rotation	600 rpm
Change of electrode rotation in pseudo-passive state	From 600 rpm to 2100 rpm with a 300 rpm step
Electrochemical cell	A

### Experimental sequence



## 4.1 The effect of an applied potential to the electrode

### 4.1.1 Potentiodynamic polarization

Figure 35 shows the anodic polarization curve of the carbon steel working electrode when it is in the active state, *i.e.* for a short exposure time at open circuit potential, before pseudo-passivation. The current-potential dependency shows that the anodic reaction is controlled by the charge transfer step. A small linear potential range is present, the calculated Tafel coefficient is 71 mV/dec. Equally the cathodic reaction is limited by charge transfer although the Tafel coefficient is higher: 234 mV/dec. In active state the electrochemical reactions are limited by charge transfer. This fact is further supported by the impedance diagram, obtained at the start of the test, reported in Figure 36.

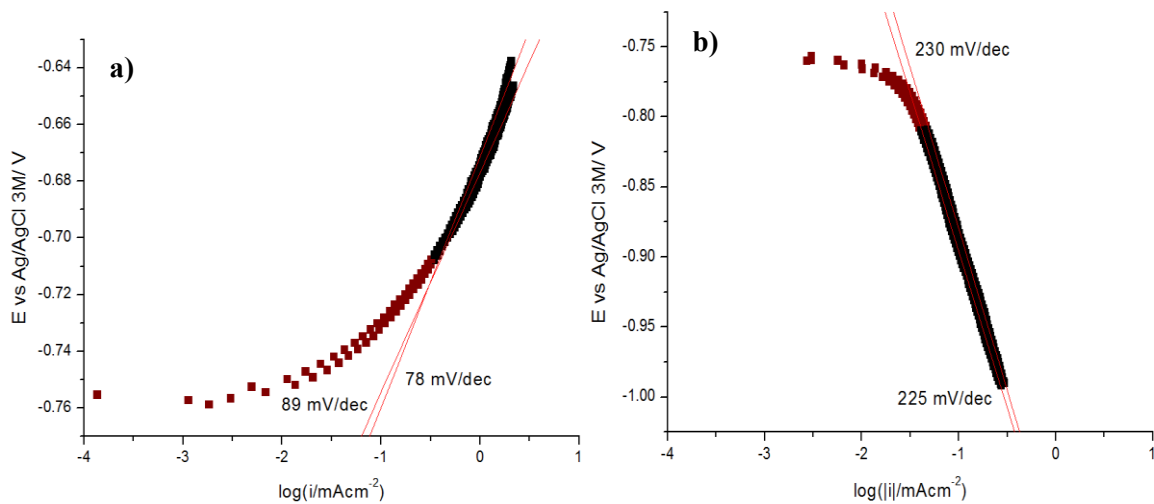


Figure 35 Polarization curves obtained in active state after 5 hours of immersion for the carbon steel in the pH 6.8, 2 g/L NaCl, 80°C carbon dioxide saturated aqueous solution (scan rate: 0.250 mV/s): a) anodic and b) cathodic branches.

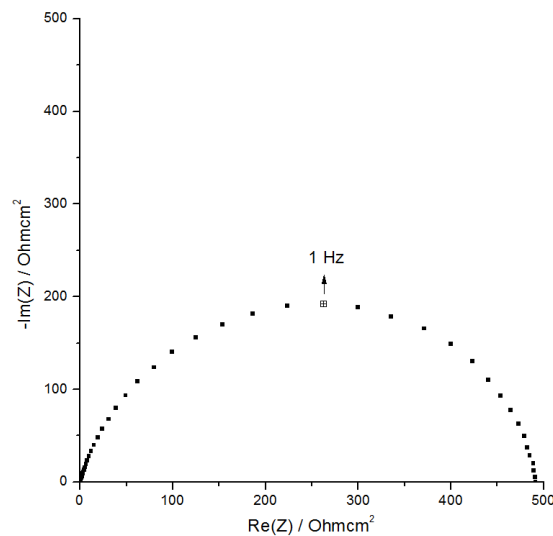


Figure 36 Nyquist impedance diagram obtained after 5 hours of immersion for the API X65 carbon steel in a 2g/L NaCl CO<sub>2</sub> saturated solution (pH = 6.8) at 80°C.

A further test is carried out in order to investigate the anodic polarization curve when the material is in pseudo-passive state. The result is reported in Figure 37, and for the first 100 mV anodic range: the potential versus the logarithm of the current density shows a quasi-linear relationship. Unfortunately, since the extent of the active surface is unknown the anodic Tafel slope in the pseudo-passive range cannot be calculated. In Figure 37 the polarization started after the pseudo-passivation of the surface. Even in this case, the passivation plateau is not observed, a constant current is measured at high overpotential but the current density is too high to be deemed as a passive plateau. Interestingly, a current peak is observed around -500 mV vs reference electrode. This peak was already observed by Keddam *et al.* when polarizing carbon steel in a slightly acid solution (pH 5) and it was attributed to the carbon steel pre-passivation [12,13].

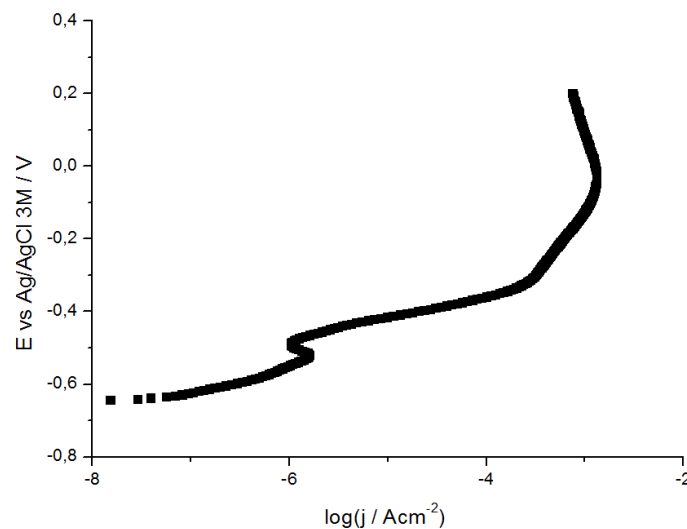


Figure 37 Anodic polarization curve obtained from the "pseudo-passive" state after exposure to an 80°C 2g/L NaCl CO<sub>2</sub> saturated aqueous solution at pH 6.8.

#### 4.1.2 Electrochemical characterization of the scales before pseudo-passivation (active scales)

Figure 38 displays the evolution of the open circuit potential during the first 24 h exposure for the carbon steel to the corrosive environment (pre-pseudo passivation conditions). After a quick decrease of the open circuit potential for reaching the stationary conditions, the OCP rises continuously and slowly without leading to a plateau that will indicate the formation of a pseudo-passive corrosion product layer. For this short time exposure situation, the electrochemical reactions on a surface where the corrosion product layer has partially precipitated are investigated to compare them with the ones that were obtained after a longer immersion time leading to a much more compact and protective film.

Concerning the impedance measurements related to the first 24 h of exposure (Figure 39), for the OCP test conditions, the Nyquist plots show a single time constant related to capacitive behavior whose diameter increases with the exposure time in the corrosive solution. These observations are in agreement with the potentiodynamic polarization curves that were presented in the previous section (Figure 33).

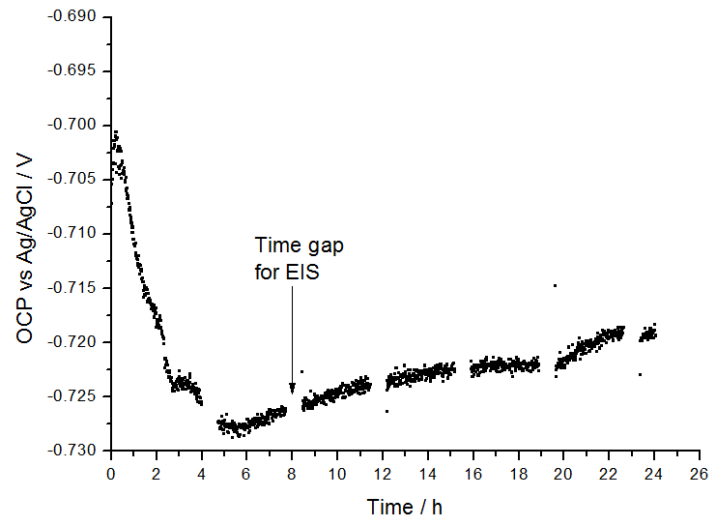


Figure 38 Evolution of the open circuit potential with time for the carbon steel exposed to the 80°C 2 g/L NaCl CO<sub>2</sub> saturated aqueous solution at pH 6.8.

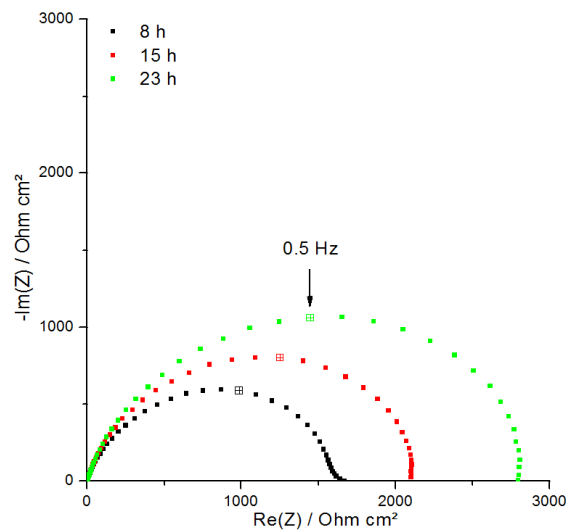


Figure 39 Electrochemical impedance diagrams, in Nyquist plot, obtained at corrosion potential during time, for carbon steel in immersion in an 80°C 2 g/L NaCl CO<sub>2</sub> saturated aqueous solution at pH 6.8.

The observed increase of the charge transfer resistance cannot be attributed to a change in the reaction mechanism, such as surface-adsorbed intermediates, as otherwise a change in the value of the time constants would have been observed (Figure 39). The mechanism of the reaction is still under activation control. Furthermore, no OCP change is observed thus the decrease in the rate of both the anodic and cathodic reaction is proportional. Considering these results, a simple decrease of the active surface should explain the increase of the charge transfer resistance.

Comparing the results of the two replica tests, the diameter of the impedance spectra before the anodic polarization is different in the two cases (Figure 40). The coverage difference among the two replicas is intrinsic to the heterogeneous nucleation which is a stochastic process depending on the concentration of the nucleation sites over the substrate (carbon steel in our case). Therefore, both the contributions of the surface and the solution with its ionic activity that leads to the carbonates saturation factor, are relevant in the precipitation of the corrosion product layer. Small differences in the conditions at the start of the test, such as the time needed for the solution to reach the proper temperature, may also alter the initial condition of nucleation and the following growth of the iron carbonate crystals.

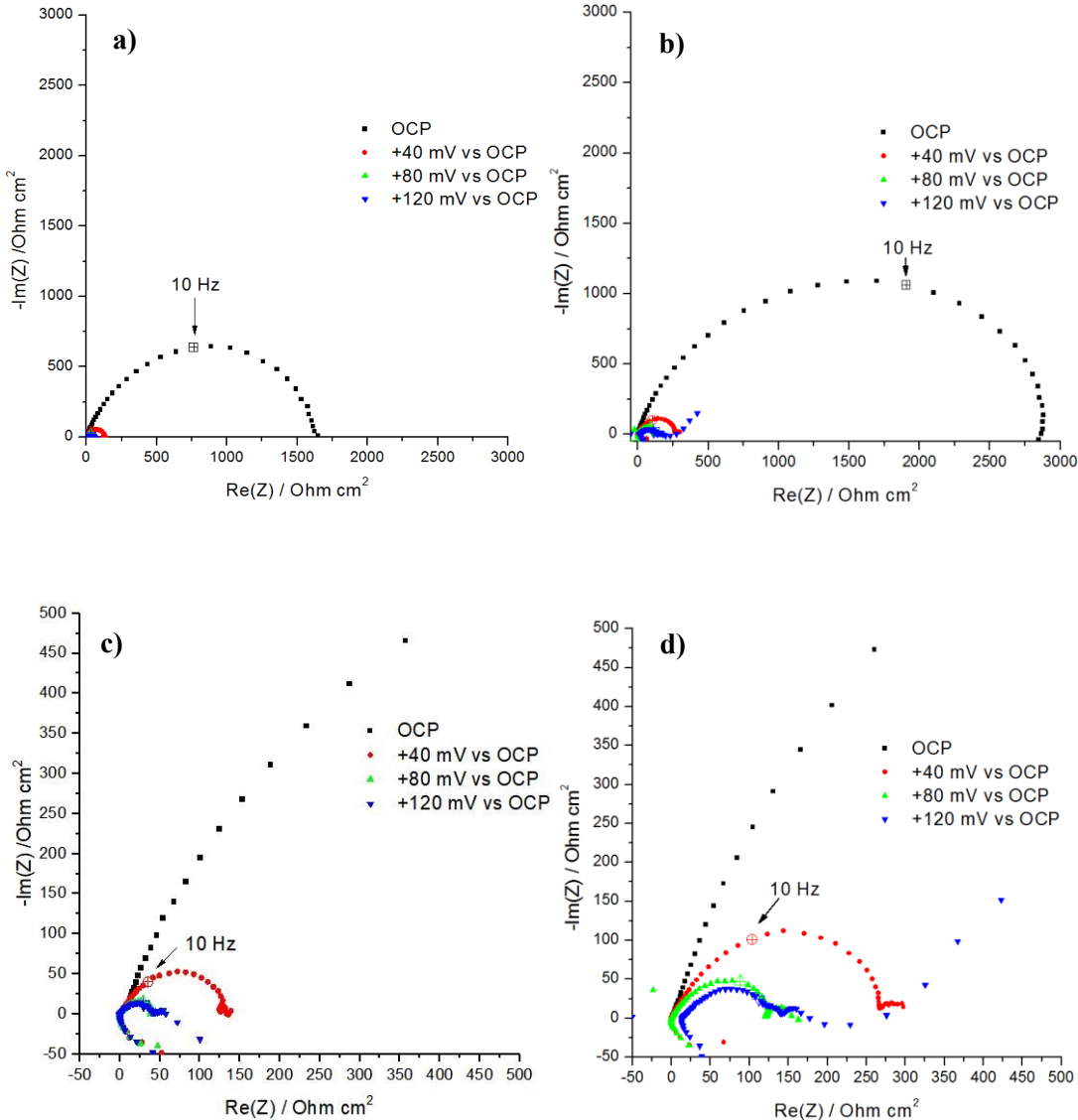


Figure 40 Electrochemical impedance diagrams obtained at different anodic potentials after 24 h of exposure time at OCP for the carbon steel in the 80°C 2g/L NaCl CO<sub>2</sub> saturated aqueous solution at pH 6.8. a) and b) both replicas are shown. c), d) zoom of the high frequency part of a) and b), respectively.

The results of the current density recorded during the different steps of polarization are reported in Figure 41. In the case of the first two anodic polarization steps (+ 40 and + 80 mV), the current density

reaches a stable value whereas for the last step at +120 mV vs OCP, a stable current density is not reached in 15 minutes (Figure 41 a). Figure 41 b) shows the current density registered for the experiment with the same steps towards the cathodic direction. In this case, the registered current density reaches a stable value during the polarization period although there are more significant noises around the mean current, probably due to the lower current density values.

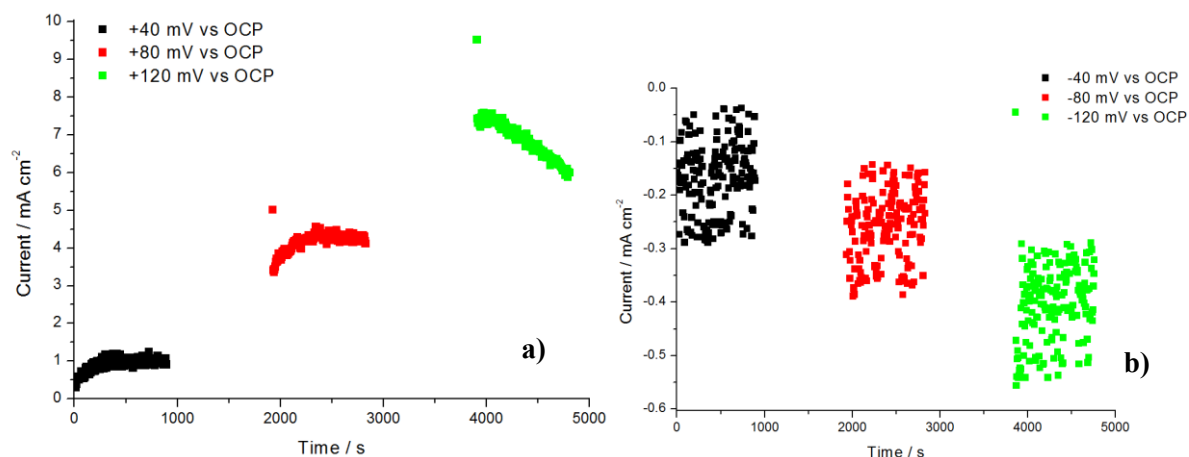


Figure 41 Evolution of the current density for each (a) anodic and (b) cathodic overvoltage, applied after 24 h of exposure time of carbon steel to the 80°C 2 g/L NaCl CO<sub>2</sub> saturated aqueous solution at pH 6.8.

In order to overcome the different coverage degrees that can occur in the early stages of the test and to compare the different results regardless of their initial charge transfer resistance, the adimensional Nyquist plot is used for analyzing the anodic overpotential effect (Figure 42). Normalization of the Nyquist plot is obtained with respect to the highest charge transfer resistance value of the impedance diagram at OCP.

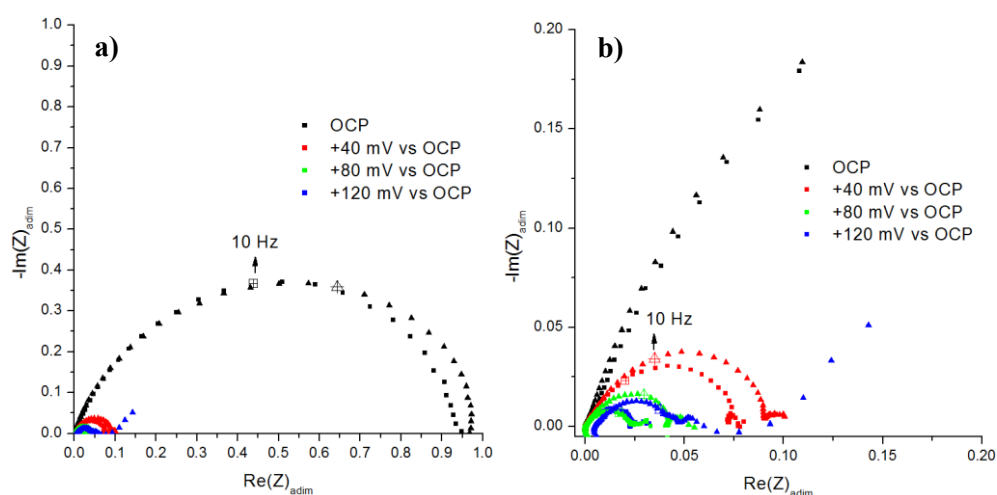


Figure 42 Adimensional Nyquist diagrams for both replicas from Figure 40, a) full frequency range and b) detail in high frequency range.

When comparing the diameter of the capacitive loops at the OCP and at +40 mV, a reduction down to 10% of the total diameter is observed. Moreover, the shape of the impedance diagram changes from a single time constant to a three-time constants involving an inductive loop. By increasing the polarization value to 80 mV and 120 mV vs the OCP, the diameter of the capacitive loop reduces down to 5% with respect to the initial diameter. The impedance results are coherent both with the potentiostatic polarization in Figure 41 and with those obtained during the potentiodynamic polarization in an aqueous solution saturated by pure CO<sub>2</sub> (Figure 35). All the three polarized tests display a three time constants plot similar to the impedance plots reported by Keddam *et al.* for an active surface in a slightly acid environment (pH 5) where an additional inductive and capacitive loop have been reported [12,13].

On the other side, the cathodic polarizations after 24 h result in an increase in the diameter of the capacitive loop with respect to the one measured at OCP (Figure 43). However, the diameter of the single time constant monotonously decreases going from the lowest to the highest overpotential. Furthermore, the impedance spectra obtained under the cathodic polarization have the same shape and number of time constant of those collected perturbing the system around the OCP.

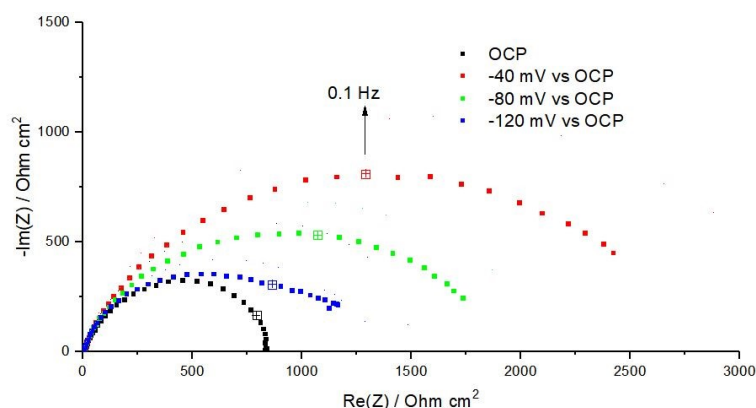


Figure 43 Nyquist impedance diagrams obtained for the carbon steel at different cathodic potentials after 24 h of exposure time to the 80°C 2g/L NaCl CO<sub>2</sub> saturated aqueous solution at pH 6.8.

### 4.1.3 Electrochemical characterization of pseudo-passive scales

In this section, the same electrochemical characterizations have been performed after reaching the pseudo-passive state.

As Figure 32 shows, the OCP of the working electrode remains constant and suddenly rises to a more anodic potential, a clear sign of pseudo-passivation. The evolution of the LPR corrosion rate indicated a decrease until a plateau corresponding to pseudo-passive corrosion scales was reached (Figure 32). These evolutions are supported by the impedance spectra obtained during time where a low frequency time constant appears after the pseudo-passivation of the surface (Figure 33).

Figure 44 reports the current density measured on the electrode during the polarization performed at the end of the pseudo passivation test. The current density values are normalized for the entire surface of the electrode even if the scales coverage reduces the active area.

The current density values show a constant mean value centered around zero for the anodic polarization whereas for cathodic overpotentials steady current slightly decreases. For the anodic polarization cathodic current density measurements are observed, the opposite occurs for cathodic overpotentials. In any case the current density values are very small. Signal noise is observed both in the cathodic and the anodic direction, the perturbation is in the order of  $10^{-5}$  A cm<sup>-2</sup>.

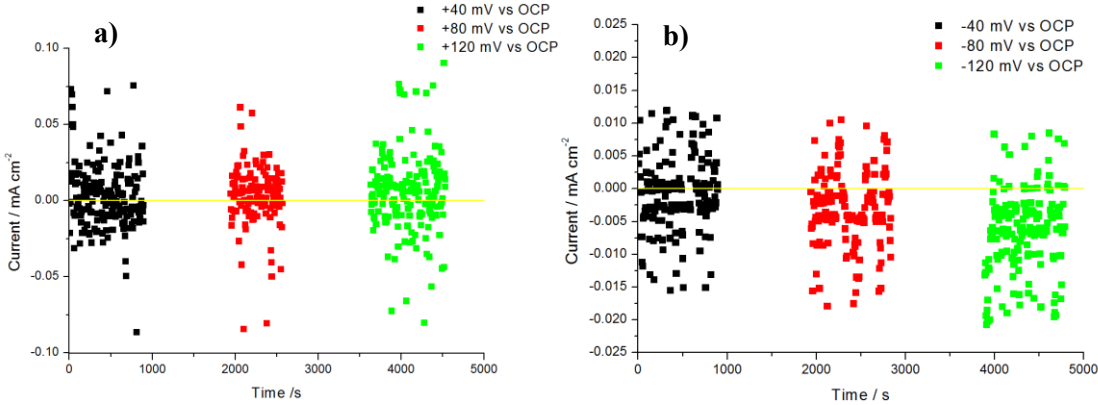


Figure 44 Current density variations corresponding to different potentiostatic conditions for the carbon steel after 2 days exposure to the 80°C 2 g/L NaCl CO<sub>2</sub> saturated aqueous solution at pH 6.8 (pseudo-passive scales): a) anodic polarization and b) cathodic polarization.

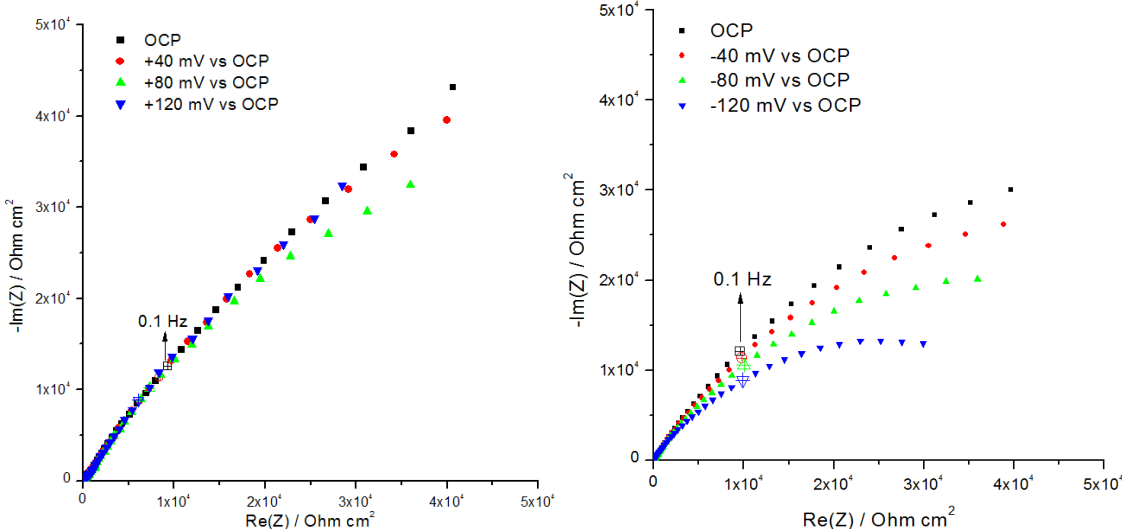


Figure 45 Electrochemical impedance diagrams (in Nyquist representation) obtained for different overpotentials from the OCP in pseudo-passive state after exposure to the 80°C 2 g/L NaCl CO<sub>2</sub> saturated aqueous solution at pH 6.8: a) anodic overpotentials and b) cathodic overpotentials.

The impedance measurements with increasing potential steps are reported in Figure 45. The Nyquist plot does not show any difference between the diagrams at increasing potentials when the working electrode is polarized anodically. The same procedure applying a cathodic overpotential shows that contrarily to the anodic overpotential, the impedance spectra measured during the cathodic polarization tests have both a decrease of the impedance modulus and a transformation of the capacity behavior at low frequency (LF) where the original semicircle changes into a straight line (Figure 42 b).

The magnitude of the impedance modulus at low frequency decreases monotonously with the higher cathodic overpotential applied (Figure 46).

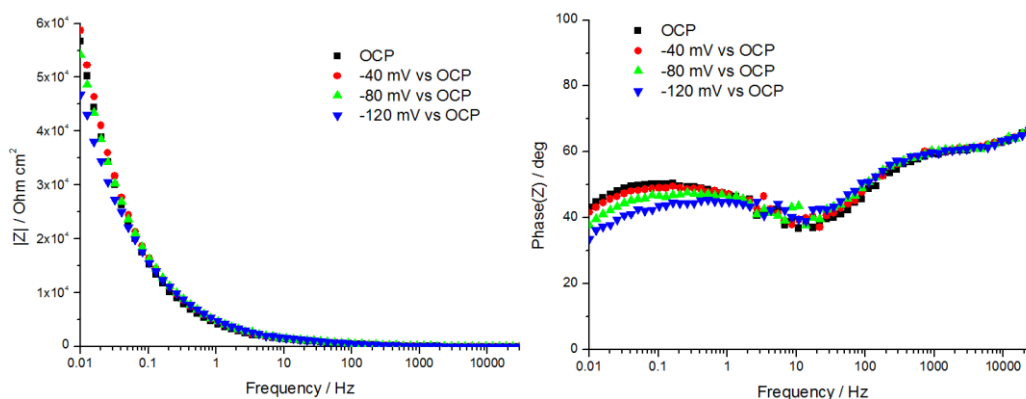


Figure 46 Impedance measurements at different cathodic potentials from the OCP in pseudo-passive state after exposure to an 80°C 2 g/L NaCl CO<sub>2</sub> saturated aqueous solution at pH 6.8. Bode representation (impedance modulus in left and phase in right as a function of frequency).

These results disagree with the potentiodynamic polarization results that were reported in the homonymous section of this chapter. In that case the electrochemical reactions were dependent from the potential even in the pseudo-passive state whereas the impedance measurements show the opposite. This is probably due to a modification of the scales caused by the high polarization potential applied during the measurement

SEM images of the corrosion samples inserted at the free potential into the electrochemical cell display the structure of the corrosion product layer. As the corrosion samples do not undergo any electrochemical polarization, the surface analysis presented hereafter is valid for the same experimental conditions *i.e.* pH 6.8 2 g/L NaCl and 80°C. SEM cross-sectional analysis is reported in Figure 47. Mechanical polishing of the corrosion product layer results in a scarce resolution of the crystals of the surface. The procedure risks damaging the corrosion product layer. A better image of the pseudo-passive film can be obtained with ion polishing (Gatan Ilion ion polisher) reported in Figure 47 b). The micrograph shows a clear and compact crystalline layer covering entirely the surface with a 7 μm thickness.

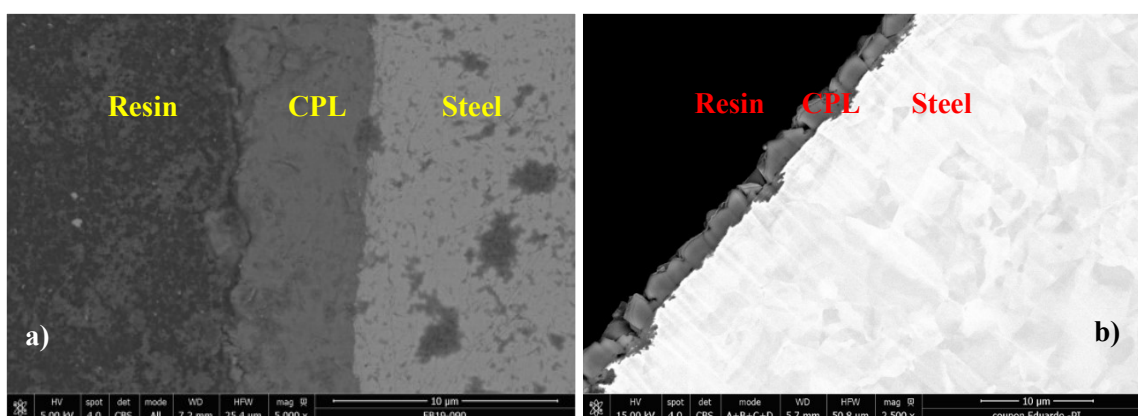


Figure 47 Cross section SEM micrographs of a carbon steel sample in pseudo-passive state after exposure to the 80°C 2 g/L NaCl CO<sub>2</sub> saturated aqueous solution at pH 6.8: a) mechanical cross-section and b) ion polishing.

Grazing X-ray diffraction analysis (GXRD) confirms that the CPL is formed by siderite crystals (Figure 48). Moreover, no other phases were identified although the technique is not optimal for detecting spots of other phases underneath the film.

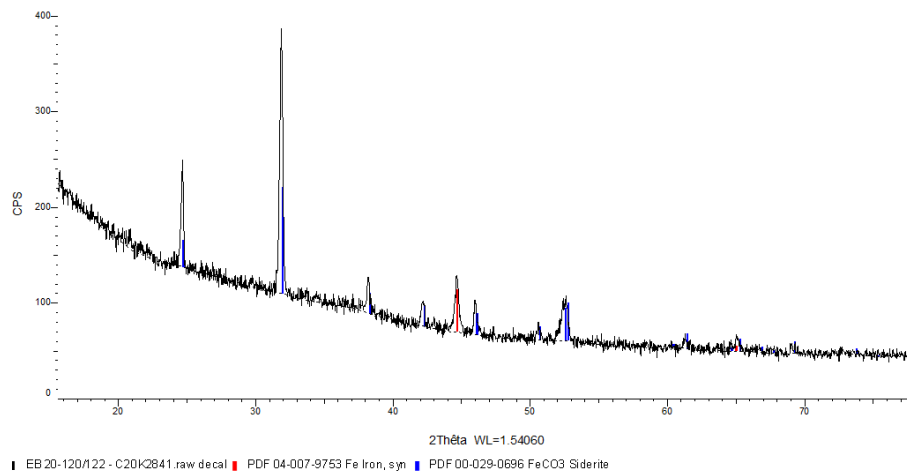


Figure 48 Grazing X-ray diffractogram of the pseudo-passive corrosion product layer precipitated in an aqueous solution with a 2 g/L concentration electrolyte, pH 6.8 and 80°C, saturated by CO<sub>2</sub>.

Furthermore unlike the observations of Han *et al.*, our grazing X-ray analysis and SEM cross-section observation does not indicate the presence of other phases between the siderite and the metal surface [49].

The crystals formed on top of the metal surface are in the order of dozens of micrometers. Considering the top-view images of Figure 49, the shape of the crystals suggests that the main phase is siderite. Siderite crystals have not a monodispersed size but they are a mixture of bigger and smaller crystals that range from 2.5 μm to 10 μm. This broad size distribution allows the surface to be well covered by the siderite crystals: no naked surface is visible from a top-view analysis. The crystals have not evident defects, even if the crystals are not completely formed because the interconnection between two growing crystals produces distorted geometries.

Figure 49 b) shows a step-like structure on the sides of the crystals highlighting the growth planes of the crystals that intersect with each other.

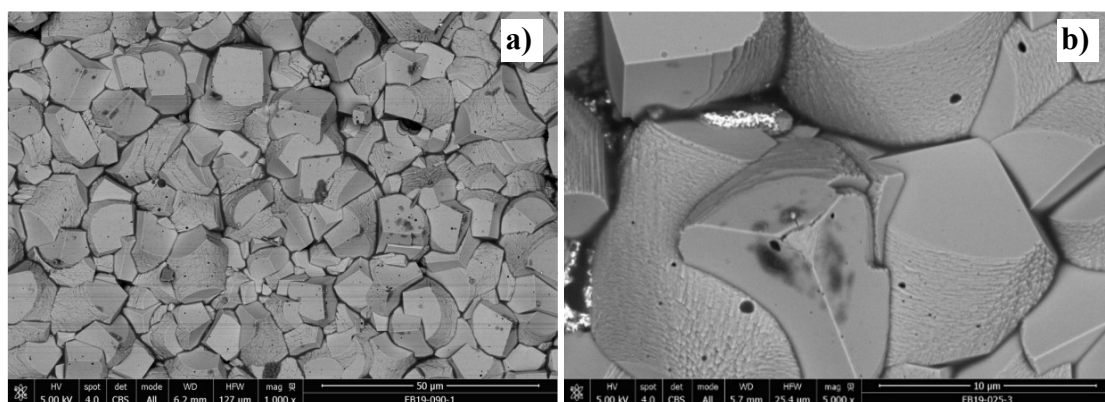


Figure 49 Top-view SEM images of a carbon steel sample in pseudo-passive state after exposure to an 80°C 2g/L NaCl CO<sub>2</sub> saturated aqueous solution at pH 6.8.

#### 4.1.4 Analysis of the results on the influence of potential

The electrochemical impedance spectroscopy measurements that were performed at different potentials can give information related to the kinetics of the electrochemical reactions occurring at the working electrode. Furthermore, those data can also be integrated with the steady state current density that was measured right before the impedance measurements.

##### *Before pseudo-passivation*

Firstly, the impedance diagrams obtained at OCP should be considered. The charge transfer resistances of the spectra after 24 h differ from each other (Figure 40). The constant OCP value measured in the first 24 hours (Figure 38) suggests that the deceleration of the anodic and cathodic reaction rate is similar for both processes. Moreover, the single time constant observed on the impedance diagrams highlights an activation control electrochemical reaction. For these reasons it is expected that the corrosion product layer has only a covering effect, where the scales precipitating on the surface reduce the active surface area. As mentioned earlier, since the charge transfer resistance is not the same in the first 24 h ( $1600 \Omega\text{cm}^2$  in the first case and  $2700 \Omega\text{cm}^2$  in the second case), it can be deduced that the nucleation and growth kinetics can change in the first instants even if the conditions are the same. In fact, heterogeneous nucleation is a stochastic phenomenon.

Normalizing the spectra allows the comparison between the results of the impedance spectroscopy at a more anodic overpotential. The spectra obtained when the working electrode was anodically polarized result in a diminution of the capacitive loop diameter with the appearance of an additional inductive and capacitive time constant at low frequency.

The charge transfer resistance is reduced to 10 % of the initial value when it was polarized to +40 mV vs OCP. On the other side the impedance spectra, when polarized in the cathodic direction, shows a greater charge transfer resistance with respect to EIS diagrams at OCP (Figure 43). Therefore, the charge transfer resistance of the cathodic reactions occurring at the surface are greater than the one of the iron dissolution reaction. For this reason, impedance measurements centered around the OCP are mainly characterized by the evolution of the charge transfer resistance of the anodic process, that is the iron dissolution reaction. Furthermore, the presence of a single time constant and its shape indicate an activation-controlled reaction before pseudo-passivation.

These observations can be explained if the corrosion product layer acts as an insulating coating separating the metal surface from the corrosive solution thus reducing the active surface area. The reduction of the active surface exposed to the corrosive solution leads to the progressive increase of the charge transfer resistance as the diameter of the semicircle of the Nyquist plot highlights.

The results of the steady-current density ( $i$ ) in potentiostatic testing are in line with the impedance measurements. The current density rises progressively the more the potential is moved away from the open circuit potential for the anodic polarization (Figure 41). In the case of cathodic polarization, the same behavior occurs.

Furthermore, the cathodic current density is lower than the anodic one for the same absolute value of overpotential pointing out a greater charge transfer resistance for the cathodic processes since the reaction is controlled by activation. Once the cathodic polarization of the working electrode reaches a high overpotential, the cathodic charge transfer resistance lowers down as expected for an activation-controlled electrochemical reaction (Figure 43).

### *After pseudo-passivation*

The electrochemical behavior of the carbon steel changes when the pseudo-passive state is reached. The steady-state current density measured at the three different anodic potential steps remains constant (Figure 44). The current density values oscillate both in the cathodic and anodic current density domains even at high anodic overpotentials. The first observation seems to suggest a limiting current density that is independent of the potential value. The second observation remarks that the cathodic reaction current density in those conditions has the same order of magnitude as the reactions originating from the iron dissolution process. On the contrary, a polarization towards the cathodic side does not result in a constant current density: a small variation can be detected that highlights the absence of a limiting cathodic current density (Figure 44). Nevertheless, the charge transfer resistance seems to be higher for the cathodic processes in pseudo-passive state with respect to active state.

The impedance spectra obtained during the anodic polarization in pseudo-passive state show the same linear low frequency (LF) tail which could be correlated to a diffusion limitation (Figure 45). On the contrary, the impedance spectra obtained applying a cathodic overpotential result in the transformation of the LF linear tail into a semi-circle similarly to the Nyquist diagrams in active state (Figure 46). Therefore, the results suggest that diffusion limitation of the anodic reaction is induced by the corrosion product layer whereas the cathodic reaction remains an activation-controlled process. Finally, the sudden OCP rise is consistent with a slowdown of the anodic reaction: a simple continuation of the scales coverage would result in an equal decline of the cathodic and anodic reaction rate and, consequently, a constant OCP.

The potentiodynamic polarization in Figure 37 shows that the current density does not remain constant in the anodic region, unlike the potentiostatic experiment (Figure 44). Therefore, the potentiodynamic results are in contrast with the hypothesis of a diffusion limitation linked to the anodic reaction because no passivation plateau was detected.

Unfortunately, the polarization curve cannot provide any reliable values of Tafel coefficients because the formation of the corrosion product layer precipitation changes the extent of the active area. The observed polarization curve is similar to the one reported by Keddani in a pH 5 aqueous solutions where two current maxima are detected, the first one related to surface saturation of Fe(I) and Fe(II) and the second one to the passive section of the polarization curve [12,13]. Therefore, the polarization curve reported in Figure 37 could suggest that, even in a pseudo-passive state, the corrosion product layer has no effect on the reactions occurring on the working electrode. This hypothesis seems unlikely because of the observed changes of open circuit potential, impedance and potentiostatic measurements before and after pseudo-passivation. Another explication for this inconsistency between the techniques can be the undermining effect that occurs between the metal and the scales, provoking a detachment of the film thus leading to exposure to the corrosive environment of an active surface. The origin of the diffusion limitation should be related to the scales grown on the metal surface since a significant evolution of the impedance before and after pseudo-passivation occurs. Indeed, a siderite compact layer completely covers the surface, the metal underneath is, for the great part, beyond the reach of the corrosive solution (Figure 47). No other phase than siderite has been detected. Thus, siderite can be deemed to be responsible for the protection of the corrosion samples acting as a diffusion barrier. No continuous magnetite layer was observed (Figure 47). Therefore, the identification of a magnetite film as the responsible agent for the pseudo-passivation of the corrosion product layer has not found any evidence in this study. This result is in contrast with Han *et al* that indicated magnetite could be responsible for the protectiveness of the pseudo-passive state [49]. The step-like structure on the side of the crystals can be attributed to the growth planes of siderite crystals

(Figure 49 b). Besides, the SEM micrograph images suggests that the growth process has not been completed to well-shaped crystals. Other crystals are still in formation. However, the pseudo-passive state is reached even in the absence of full-grown crystals so that partially grown crystals seem to effectively protect the surface.

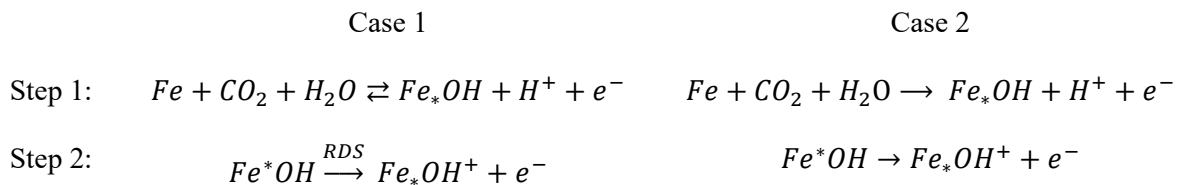
#### 4.1.5 Discussion on a possible mechanism

##### *Anodic reactions*

In order to explain the evolution of the impedance measurements as a function of the exposure time, a mechanism of the electrochemical reaction is proposed. The key point is to find a mechanism that can both explain an activation control when the metal is directly exposed thus behaving as an active surface and a diffusion limitation when iron carbonate forms a compact non-porous coating on top of the metal. However, considering the observations on the mechanism of the previous paragraph, a diffusion limitation of the iron dissolution reaction does not seem likely because the reactant, iron, is the surface itself. Nevertheless, it could be explained by assuming that an adsorbed intermediate participates in the rate determining step. This adsorbate could be formed by the combination of iron and a carbonated species in the solution or the dissolved carbon dioxide itself.

The literature provides some example of that, such as the mechanism proposed by Nescic *et al.* involving the direct reaction of iron and carbon dioxide leading to an adsorbed intermediate complex Fe-CO<sub>2</sub> [17].

Carbon dioxide, chlorides or any other carbonate species should intervene in one or more steps (not adsorbing directly on the surface as pointed out by Almeida *et al.* [23]) of the charge transfer reaction in order to explain the diffusion limitation observed during the impedance measurements. Hereafter two similar mechanisms are proposed considering the adsorption of CO<sub>2</sub>. The kinetic relationship would be the same even in the case of other adsorbate: it suffices to substitute CO<sub>2</sub> with the responsible adsorbed chemical species.



##### *Reaction 10*

$Fe^*$  represents a carbonated intermediate complex adsorbed on the surface (Reaction 10). The nature of this intermediate is unknown, but it should be formed with the species present in the electrolyte such as carbonic acid, bicarbonate or chloride ions. Case 1 and case 2 are based on two different assumptions regarding the first step. In the first situation, step 1 is a pseudo-equilibrium whose forward reaction has a rate directly proportional to the carbon dioxide concentration. Considering quasi neutral pH, the concentration of adsorbed OH<sup>-</sup> is constant. This point of the mechanism involving the adsorption of an intermediate depends strongly on the nature of the intermediate itself. The Langmuir relationship should be evaluated according to the chemical species in the solution that interacts with the surface leading to the adsorbed product of step 1.

In the second case, step 2 is considered faster than the first one which is irreversible. For these reasons, steady-state approximation can be applied. Both the mechanisms can have an anodic current

directly proportional to the concentration of the carbonate species. Moreover the empirical dependence on OH<sup>-</sup> concentration and carbon dioxide partial pressure respects the empirical observations reported by Nesic *et al.* at different pH and carbon dioxide partial pressures [17].

The equation of the kinetic of the anodic current densities obtained from the above-mentioned mechanisms are reported hereafter where  $F$  is the Faraday constant,  $R$  the gas constant and  $E$  is the electrode potential (Equation 7):

$$i_a = k[CO_2]e^{\frac{3FE}{2RT}} \text{ for case one} \qquad i_a = k[CO_2]e^{\frac{1FE}{2RT}} \text{ for case two}$$

Equation 7

They give a Tafel slope of 40 mV/dec and 120 mV/dec (from the exponent in Equation 7), respectively. The diffusional limitation of the anodic electrochemical reaction comes from the first step where the iron combines with carbon dioxide, a carbonated species or chlorides.

The hypothesis of a slow Fe<sup>2+</sup> evacuation from the surface towards the bulk of the solution (as suggested by Crolet *et al.* [97]) can be also considered. This hypothesis suggests that the accumulation of Fe<sup>2+</sup> ions in the metal/solution interface slows down the anodic reaction. Nevertheless, iron ions do not adsorb on the metal surface nor their contribution is derived from any electrochemical rate-determining step kinetic relationship since they are the product of the electrochemical reaction and never the reagent. For this reason, this kind of behavior cannot be observed with electrochemical impedance spectroscopy whose current signal depends on a potential-concentration-current relationship. Since the pseudo-passivation of the surface and the evolution of the scales towards pseudo-passivity can be followed and determined using EIS, the hypothesis of an “overconcentration” of iron ions at the surface slowing down the anodic reaction has to be excluded.

### *Cathodic reactions*

The previous paragraphs were focused on the anodic reactions, for a complete picture cathodic processes should be considered as well. In fact, the cathodic process is central in understanding the corrosion process. Moreover, the proton reduction at the surface modifies the surface pH value which should be slightly higher than within the bulk. The results of the impedance measurement performed at increasing cathodic overpotential show that the cathodic reaction is controlled by activation both in the active and the pseudo-passive state, so a careful analysis of the electrochemical reactions involved in the cathodic processes should be done. According to the literature, the higher corrosion rate for a CO<sub>2</sub> saturated solution with respect to an aqueous solution at the same pH is explained by the intervention of carbonated species in the electrochemical reactions (Reaction 8). However, their role as oxidizing agents is still debated. In fact, two mechanisms are proposed in which H<sub>2</sub>CO<sub>3</sub> reacts either by direct reaction or acid dissociation that provides an additional source of protons to be reduced (Reaction 8).

Nevertheless, because of the high pH conditions in which the tests were carried out which is even higher at the electrode/electrolyte interface because of proton reduction, the water reduction reaction cannot be disregarded. In the previous section, the hypothesis of a carbonated species gradient determining the rate of the anodic reaction was proposed. Because the impedance measurements show that the cathodic reaction is charge transfer-limited both when the surface was active and pseudo-passive, the proposed carbonated species gradient should not play a role.

Obviously, mass-transfer limitation does not hold for water and water reduction would still be charge transfer limited both in the active and pseudo-passive state. In fact, water is ubiquitous in the permeable pathways that formed in the corrosion product layer and that make the contact between the solution and the metal. Therefore, water reduction is proposed as the main cathodic process. This process could explain why the cathodic reaction is controlled by activation in pseudo-passive state whereas the anodic is limited by the mass transfer of carbonated species to the metal surface. This model will be used to obtain quantitative impedance parameters and will be discussed at the end of this chapter.

## 4.2 The effect of convection on the pseudo passivity

In this part, the results related to the effect of the rotation of the working electrode are reported. During all tests the electrode rotated at 600 rpm, the speed was then increased after pseudo-passivation until 2100 rpm with progressive steps of 300 rpm.

Figure 50 shows the evolution of the open circuit potential during the experiment. As in the previous cases, the OCP has a small but steady increase until 280 h of exposure time where it suddenly rises of about 100 mV. The corrosion rate measured with the LPR technique shows one order of magnitude decrease in the first two days, then the corrosion rate drops exponentially until pseudo-passivation where a further drop of one order of magnitude occurs. The LPR measurement points out once more that high protective status is reached once pseudo-passivation occurs.

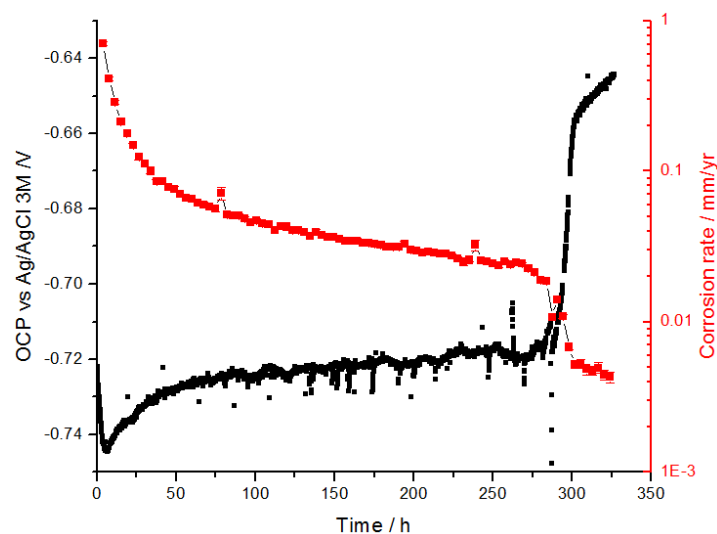


Figure 50 Open circuit potential of the carbon steel during exposure to the 80°C 2 g/L NaCl CO<sub>2</sub> saturated aqueous solution at pH 6.8. The working electrode rotated at 600 rpm.

Furthermore, impedance measurements show a significant difference between the diagrams before and after pseudo-passivation. The capacitive behavior displayed before pseudo-passivation is substituted by a linear plot in the Nyquist representation. Therefore, the results of the impedance spectra confirm that pseudo-passivation is reached with a significant change in the capacitive behavior (Figure 51).

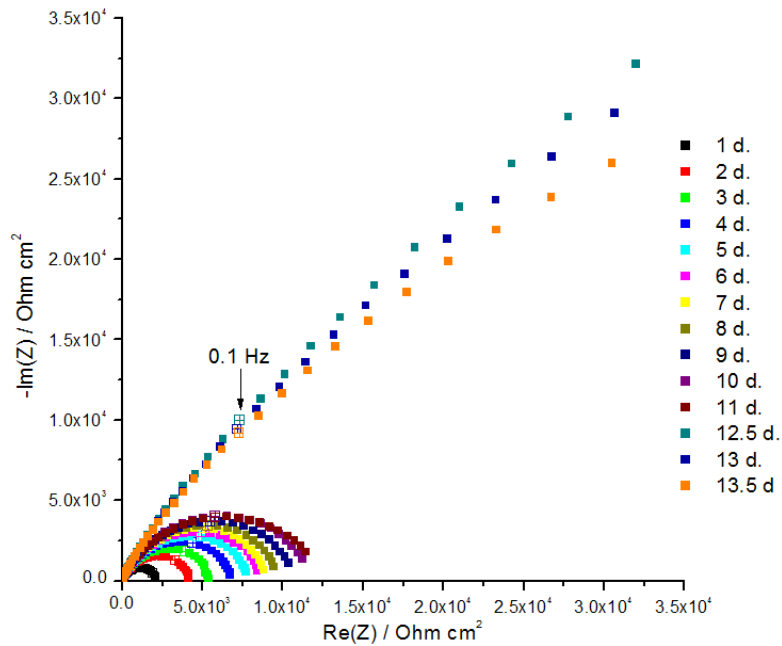


Figure 51 Nyquist impedance diagrams collected during exposure to an 80°C 2 g/L NaCl CO<sub>2</sub> saturated aqueous solution at pH 6.8. The working electrode rotated at 600 rpm.

Figure 52 shows the impedance diagrams obtained for the working electrode in pseudo-passive state rotating at different rotation rates. All the spectra registered from 600 rpm to 2100 rpm do not show any sign of change with respect to the rotation rate of the working electrode. Therefore, the rotation rate change does not have any effect on the reactions in a pseudo-passive state for the studied flow conditions and the electrolyte conditions.

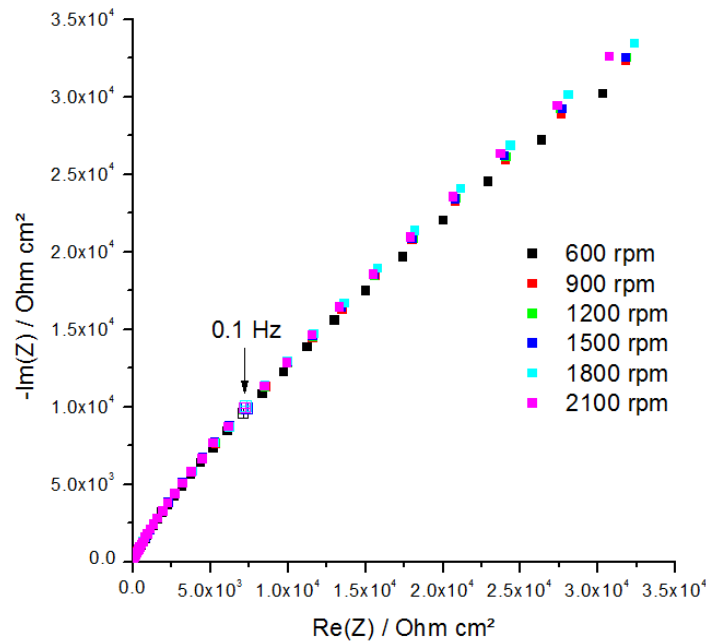


Figure 52 Nyquist impedance diagrams collected at different rotation rates in pseudo-passive state after exposure to an 80°C 2g/L NaCl CO<sub>2</sub> saturated aqueous solution at pH 6.8.

The third series of experiments aimed to investigate the effect of a controlled flow regime on the electrochemical reactions particularly when the samples reach pseudo-passive state.

The impedance spectra obtained for different rotation rates are reported in Figure 52. The pseudo-passive state is reached even in dynamic conditions. Assuming that our observations in the subchapter on the effect of potentials are correct (so that a mass-limited anodic reaction occurs), the flow conditions (600 rpm) adopted in this experiment do not prevent the corrosion product layer to develop a mass-transfer limiting process and so to become pseudo-passive. Our hypothesis seems reasonable based on the impedance response when the pseudo-passive steel is polarized anodically. Moreover, the impedance measured at OCP shows that the anodic reaction is predominant, meaning that the impedance measured at OCP will be represented mainly by the anodic process.

An increase in the rotation rate diminishes the thickness of the Nernst layer, the exact dependency is influenced by the geometry of the working electrode. A reduction of the Nernst layer thickness results in an increase of the diffusion gradient of any electrochemical species thus accelerating the mass-limited reaction. Because of that, the low frequency part of the modulus of the impedance spectra should decrease when the working electrode rotation rate is higher.

Nevertheless, the impedance measurements do not show any change especially in the low frequency range. A hypothesis to explain the phenomenon is proposed: the carbon dioxide concentration gradient is supposed to be into the corrosion product layer. In this scenario the carbonate crystals act as a shelter for the solution situated between the permeable pathways, therefore the electrode rotation rate has no influence on the solution situated inside the carbonate scales. As a consequence, the concentration gradient located in the corrosion product layer is not affected by the rotation rate thus, the impedance spectra do not change with the increasing rotation rate.

This experiment proves that the diffusion limitation does not depend on the depletion of the reactant at the surface because of the ongoing electrochemical reaction. In fact, the continuous rotation would provide a steady flux to the surface and, as a consequence, of the corrosion product layer.

### 4.3 *Conclusions on the investigations of the pseudo-passive state protection mechanism*

In this chapter, the evolution of the behavior of the electrochemical reactions through the growth of the corrosion product layer was investigated. The analysis of the impedance data for different overpotential and flow conditions were the means used for this purpose.

The investigation on the effect of the potential revealed that:

- At OCP the impedance diagrams characterize the anodic process.
- The anodic reaction is controlled by activation after 24 hours of exposure to the corrosive solution and the same rate-determining step applies for the cathodic one.
- Once pseudo-passivation is reached, the impedance diagram shows the appearance of LF time constant and the OCP rises of around 100 mV. A compact layer of siderite crystals forms the corrosion product layer.
- Potentiostatic polarization curves show that a plateau of the anodic current density is attained for all the applied overpotential. Cathodic polarization displayed a decrease in the current density.
- The evolution of the electrochemical impedance diagrams obtained for anodic overpotential is in agreement with the OCP evolutions, whereas a diminution of the impedance modulus at low frequency is observed when applying a cathodic overpotential.
- Potentiodynamic polarization curves do not show the constant current density plateau observed with the potentiostatic technique in any of the investigated potential ranges. According to these results, the corrosion product layer has no significant effect on the electrochemical reaction mechanism. This result is in contrast even with the impedance results obtained at different overpotentials.

Whereas the investigation on the effect of convection displayed that:

- Pseudo-passive state is reached even when a rotation of the working electrode of 600 rpm is applied.
- Increasing progressively the rate of the working cylinder electrode rotation does not affect the impedance of a pseudo-passive corrosion product layer.

#### 4.4 Modeling scales protectiveness before and after pseudo-passivation

In the last part of the chapter a model concerning pseudo-passive protectiveness will be detailed. The model tries to explain the evolution of the scales protectiveness as a function of time and the change in reaction mechanism before and after pseudo-passivation. The approach of the model is to treat impedance data using the electrical equivalent circuit (EEC). This tool is commonly used for obtaining quantitative parameters such as capacity and charge transfer resistance. The extrapolated values of physico-chemical properties will be used in order to verify whether the model is coherent with previous experimental observations.

Unfortunately, in the experimental conditions used in this study, chosen for the good scaling properties, the impedance spectra during the formation of pseudo-passive scales are characterized by two-time constants that are very close. Although it can be observed the rise of a second time constant at low frequency but its proximity to the original one makes it hard to analyze quantitatively the results. For this reason, the extrapolation of the electrochemical parameters such as the charge transfer resistance or the capacity of the electrode/electrolyte interface would result in a confidence interval too wide. The incertitude would produce an analysis whose results would not allow to confront them meaningfully with previous experimental results.

Therefore, the impedance analysis was performed on a set of data obtained previously by De Motte [50]. Cell B was used for the test although only one working electrode was immersed in the testing solution. Two pH conditions were investigated the first at pH 6 and the second at pH 6.6 at the same temperature of 80°C and salt concentration (0.2 % wt.). Both the solutions were saturated with carbon dioxide and the total pressure was 1 bar. Only the higher pH led to pseudo-passive scales. The different results concerning electrochemical impedance diagrams are probably due to the different experimental conditions that were used.

In the previous sections several observations related to the behavior of the electrochemical reactions throughout the test were obtained. The proposed model has to be coherent with them.

The results presented up to this point confirm that pseudo-passivation results in good corrosion protection against uniform corrosion mitigating the corrosive action of the CO<sub>2</sub> aqueous solution. However, unlike Han *et al.* no continuous film of magnetite is observed that could explain the rise in open circuit potential and the corrosion product layer protectiveness [49]. Other authors proposed a simple surface coverage that reduces the metal active surface [57,58]. This kind of behavior can be assimilated to a simplified Randles circuit (Figure 53). However, this explanation is not able to take into account both a change in the corrosion potential and the unchanged impedance spectra at anodic overpotential reported in Figure 45.

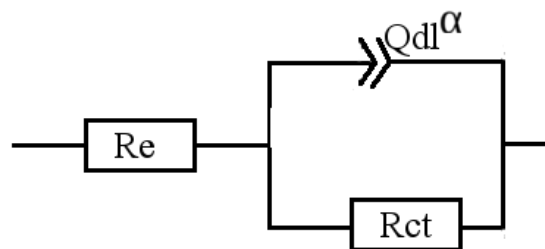


Figure 53 Simplified Randles circuit diagram.  $R_e$  is the electrolyte resistance,  $R_{ct}$  is the charge transfer resistance and  $Q_{dl}^{\alpha}$  represents the CPE.

The proposed electrochemical equivalent circuits are based on two steps. The first one explains the corrosion product layer behavior before pseudo-passivation whereas the second step deals with pseudo-passivity. In the first step the scales protect the surface with a simple coverage effect that reduces the active surface. The second step involves a diffusion limitation of the reaction that strongly lowers the corrosion rate.

A detailed explanation of the adopted model and its parameters will be done in the following section of this chapter. A published article of our work is included, the results of the study show that a simple reduction of the active surface due to scaling occurs before pseudo-passivation whereas the layer acts as a diffusion barrier after pseudo-passivation. Some magnetite islets were identified between the iron carbonate layer and the metal substrate, however no continuous layer was observed. Therefore, magnetite could not be responsible of a generalized protection of the surface. Its formation was attributed to a high surface pH in the last stages of film formation.

#### *4.5 Conclusion on modeling pseudo-passivity*

The second part of the chapter was focused on the investigation of the properties of a corrosion product layer in pseudo-passive state. In order to do that, the effect of the potential and the convection on the system impedance were considered. Those observations were particularly useful for modeling the behavior of carbon steel after the growth of the scales and in pseudo passive conditions. Besides those observations, other spectra from a previous work were analyzed quantitatively in order to extract physico-chemical parameters supporting the model claims. The main results of this part are summarized hereafter:

- Impedance diagrams evolve during the exposure to the corrosive solution following the precipitation of the scale. A significant shift from a capacitive behavior to a diffusion limited one at low frequency is observed particularly after the pseudo-passive transition.
- Before pseudo-passivation of the surface, the reactions are charge transfer limited. The corrosion rate is limited by the scales covering up the surface and reducing the active surface. This effect is supported by the constant value of the product between the charge transfer resistance and the double layer capacity when the surface is not pseudo-passive. Therefore, the reaction can be modeled through a simple activation-controlled mechanism.
- In pseudo-passive state the anodic reaction is mass-transfer limited. This is due to the scales blocking a chemical species that is adsorbed on the surface and through which iron dissolution takes place. It is supported by the observation of the effect of the potential and the convection in pseudo-passive state. Therefore, the reaction after pseudo-passive state can be modeled through an equivalent circuit that involves a Warburg component for the diffusion limitation.
- No magnetite or other phase covered significantly the metal/CPL interface. The observed magnetite is in the form of spots at the CPL/metal interface never forming a continuous layer. On the contrary, siderite was the only phase with a continuous layer over the metal substrate. The protection is given by the compact layer of siderite crystals that acts as diffusion barrier slowing down the anodic reaction.

## 5 Oxygen contamination

This chapter is related to the contamination of oxygen in a CO<sub>2</sub> aqueous solution. The contaminations were in the order of the hundreds of ppb. The investigated concentration is one order of magnitude less than the concentrations used in the literature (section 1.5.3 Effect of oxygen). At first, the contamination is introduced since the beginning of the test at various concentrations. Subsequently, different concentrations of oxygen were tested at a lower temperature in non-scaling conditions. Oxygen was introduced with a fixed concentration to the electrochemical cell inside which a pseudo-passive corrosion product layer had precipitated on carbon steel. Surface analysis of the corrosion product layer were carried out to understand the implications of this new species inside the solution. In the end, the initiation and propagation of the localized corrosion due to oxygen contaminating the solution was related to a model already proposed in the literature.

*Summary of the experimental conditions*

*Potentiodynamic polarization*

*Table 23 Experimental conditions for the potentiodynamic polarization test.*

Conditions	Values
Temperature	80°C
[NaCl]	2 g/L
pH	6.8
pCO <sub>2</sub>	0.54 bar
Start of polarization (active)	4 h CO <sub>2</sub> + 1 h O <sub>2</sub> contamination
Start of polarization (pseudo-passive)	Pseudo-passivity + 2 h O <sub>2</sub> contamination
Electrochemical cell	B

*Table 24 Experimental conditions for the oxygen contamination test introduced at t<sub>0</sub> = 0*

Conditions	Values
Temperature	78°C (60°C)
[NaCl]	2 g/L
pH	6.8
pCO <sub>2</sub>	0.54 bar
Exposure time	5 d
Dissolved O <sub>2</sub> contamination	No added O <sub>2</sub> , 90 ppb, 171 ppb, 257 ppb
Electrochemical cell	A

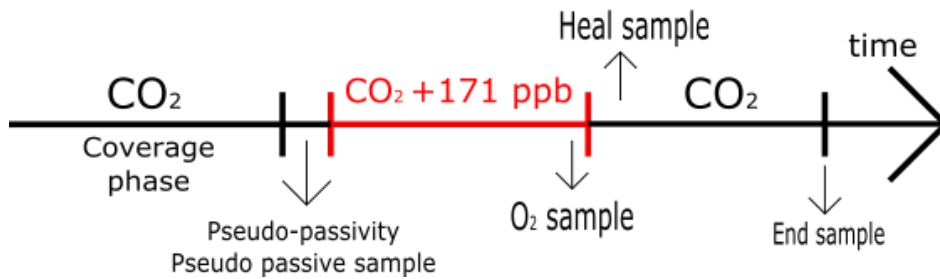
Table 25 Experimental conditions for the oxygen contamination test introduced in pseudo-passive state

Conditions	Values
Temperature	78°C (60°C)
[NaCl]	2 g/L
pH	6.8
pCO <sub>2</sub>	0.54 bar
O <sub>2</sub> introduction time	Pseudo-passivity
Dissolved O <sub>2</sub> contamination	171 ppb
Electrochemical cell	B

Table 26 Experimental conditions for the pit healing test

Conditions	Values
Temperature	78°C (60°C)
[NaCl]	2 g/L
pH	6.8
pCO <sub>2</sub>	0.54 bar
O <sub>2</sub> introduction time	Pseudo-passivity
O <sub>2</sub> feed stop time	3 days
Dissolved O <sub>2</sub> contamination	171 ppb
Electrochemical cell	B

Experimental sequence



## 5.1 Potentiodynamic polarization

Polarization curves were obtained after 4 hours of exposure of carbon steel to the reference conditions and one hour with a dissolved oxygen concentration of 171 ppb. They are reported in Figure 54.

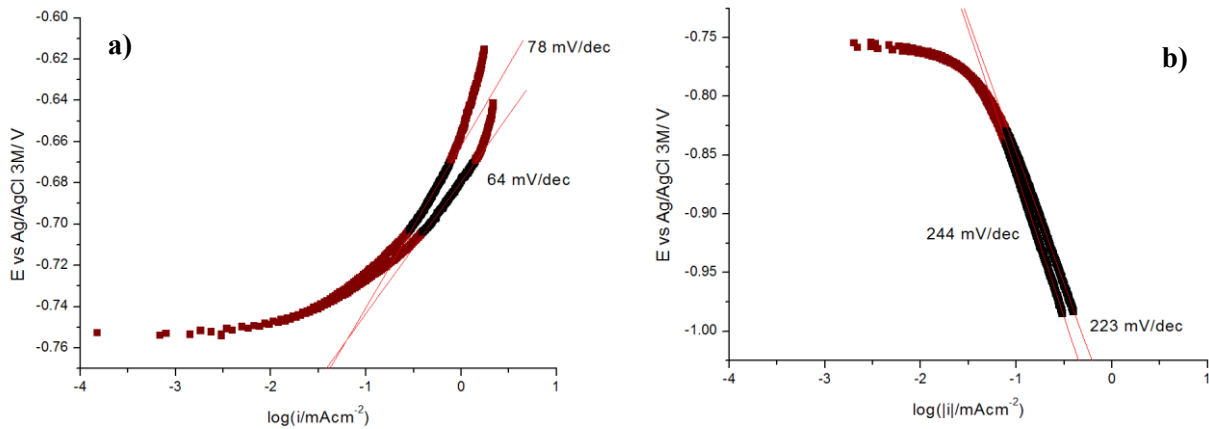


Figure 54 Anodic (a) and cathodic (b) branches of polarization curve obtained for the carbon steel in active state at pH 6.8, 2 g/L NaCl, 80°C, 171 ppb dissolved O<sub>2</sub>, in a carbon dioxide saturated aqueous solution. Four hours exposure to CO<sub>2</sub> only and one hour more to the oxygen contamination. Scan rate: 0.250 mV/s. (two replicas are shown for each case).

By comparison with a deaerated medium, the introduction of oxygen in the initial moments of the test does not change the nature of the electrochemical reaction since the processes are still charge-transfer limited. Thus, the determined Tafel slopes are 84 mV/dec and a 228 mV/dec for the anodic and cathodic reaction, respectively. The Tafel coefficients were calculated as mean value between the two replicas.

The cathodic polarization curve obtained in pseudo-passive state is presented in Figure 55 and shows a significant difference by comparison with that obtained for the active state (

Figure 54 b). Figure 55 shows that a limiting current density is attained when the sample is cathodically polarized in pseudo-passive state when O<sub>2</sub> is present even at a low concentration. This result highlights a change in the rate determining step of the oxygen reduction reaction that shifts from a charge transfer control to a diffusion limited control.

A current density limit in the pseudo-passive state in presence of 171 ppb of O<sub>2</sub> highlights the fact that pseudo-passive state is particularly protective.

For this case, the calculation of the Stern-Geary coefficient by extrapolation of the Tafel slopes of the polarization curve cannot be done since the extent of the active surface is unknown. Nevertheless, they can be approximated with the anodic Tafel coefficient of the active surface experiment and an infinite Tafel coefficient for the cathodic reaction since the cathodic reaction is limited by diffusion as the presence of a current density limit in Figure 55 suggests. Therefore, when O<sub>2</sub> is present, the values for the Stern-Geary coefficients are 24 mV/dec and 31 mV/dec before and after pseudo-passivation, respectively. Those values have been used throughout this study for evaluating the corrosion rate from the polarization resistance values given by the linear polarization resistance technique.

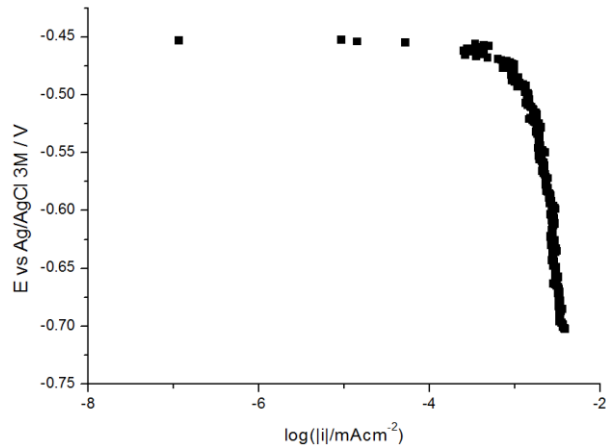


Figure 55 Cathodic potentiodynamic polarization in a pH 6.8, 2 g/L 80°C carbon dioxide saturated solution after the introduction of 171 ppb dissolved oxygen contamination in pseudo-passive state. Scan rate: 0.250 mV/s.

## 5.2 Oxygen contamination test introduced at $t_0=0$

### Without added oxygen

The method used in this part was to examine the protectiveness of the scales keeping constant the amount of time during which they precipitate. The protectiveness was then compared at the end of this testing period between several oxygen contamination values. Therefore, a base case was re-examined for a deaerated medium evaluating the system for five days. The results in Figure 56 show that the surface reached pseudo-passivation in both cases quite rapidly in a few days. The characteristic features of pseudo-passivation namely the OCP anodic shift and the decrease of the corrosion rates are stark. This situation is similar to the other tests observed before. The corrosion samples are uniformly corroded. The corrosion product layer is mainly formed by siderite, the crystals cover completely the surface offering a good degree of protection. The scales are compact and adherent to the surface.

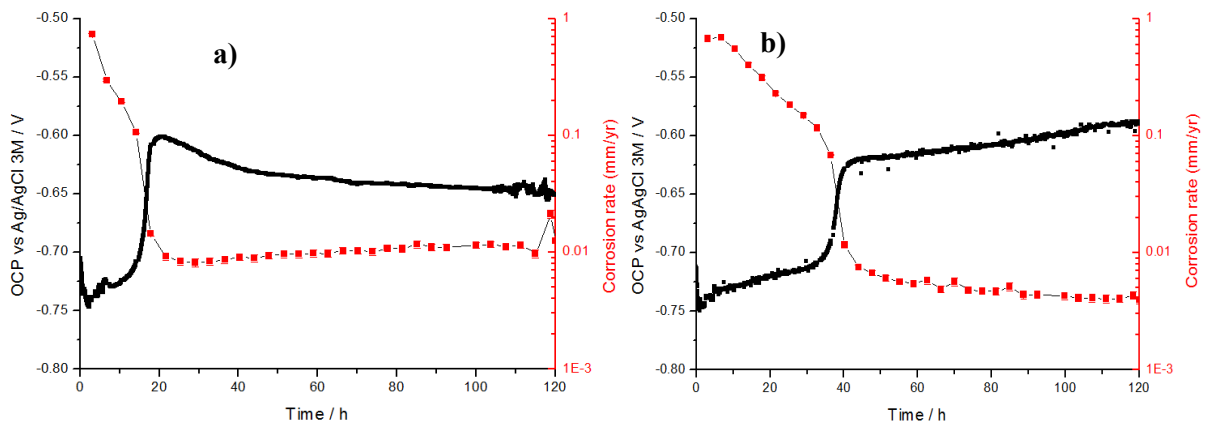


Figure 56 OCP and corrosion rate measurements for the API X65 carbon steel exposed for 5 days to a  $\text{CO}_2$  saturated aqueous solution (pH 6.8, 80°C, 2g/L NaCl). Two replicas are shown in a) and b).

The short time needed for pseudo-passivation confirms the efficiency of the reference conditions for reaching the pseudo-passive state.

### With 90 ppb of added O<sub>2</sub> contamination

The test was repeated exposing the sample to a 90 ppb oxygen contamination in the solution starting from the beginning of the test. The electrochemical measurements displayed in Figure 57 show a stark difference between the results of the corrosion process.

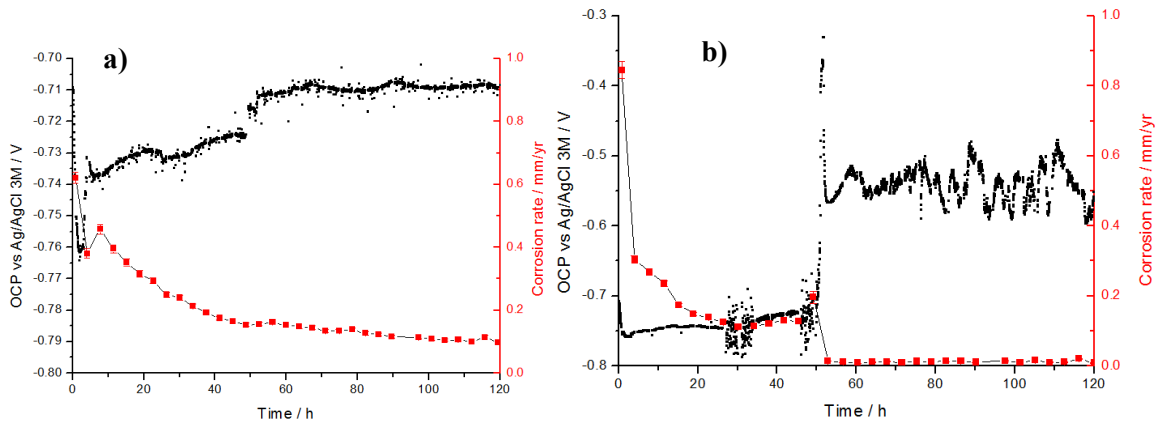


Figure 57 OCP and corrosion rate measurements for the API X65 carbon steel exposed for 5 days to a CO<sub>2</sub> saturated solution (pH 6.8, 80°C, 2g/L NaCl) and containing a 90 ppb O<sub>2</sub> contamination. Two replicas are shown in a) and b).

The results presented in Figure 57 a) show that the potential remain constant throughout the test, at the same time a slight reduction of the corrosion rate was observed always remaining in the hundreds of micrometers per year range. The sample did not passivate after five days of exposure time in the corrosive solution and that the final corrosion rate is one order of magnitude greater than the one measured when no contamination is present (Figure 56).

On the contrary, the second test (Figure 57 b) shows a 400 mV potential increase after two days since the beginning of the experiment. Afterward, the OCP value drops by more than 200 mV, a considerably higher shift than the one due to the pseudo-passivation. The OCP fluctuates significantly after this shift whereas it remains constant when no oxygen is present. Finally, the LPR corrosion rate decreases after 50 h of immersion, marked by the OCP transition.

However, the cylindrical working electrode, in this case, presents evident forms of localized corrosion (Figure 58). After the removal of the corrosion product layer, the pit-like features are quite big and can be seen by the naked eye. Moreover, they are equally distributed all over the surface.

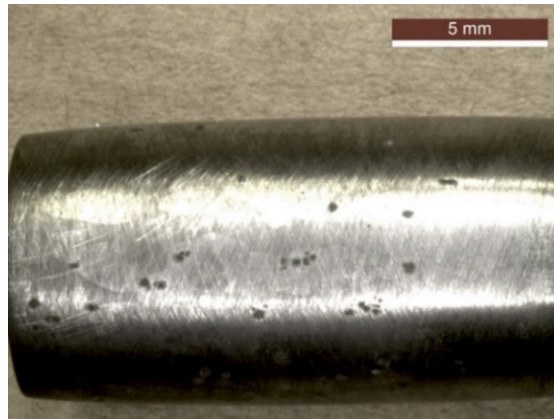


Figure 58 Picture of the cylindrical carbon steel electrode after 120 h of immersion at corrosion potential in the solution containing 91 ppb of oxygen, corresponding to the result presented in Figure 57 b).

#### With 171 ppb of added O<sub>2</sub> contamination

The concentration of dissolved oxygen in the solution was then risen to 171 ppb. As previously, two replicas are reported in Figure 59. The first test shows that the potential remains stable for 5 days and the corrosion rate reaches a constant value of 200  $\mu\text{m}/\text{yr}$  (Figure 59 a). In this case, the surface does not reach pseudo-passivation nor adequate protection is given to the material. Nevertheless, the working electrode is corroded uniformly, the pickling of the surface confirmed that no pits were present.

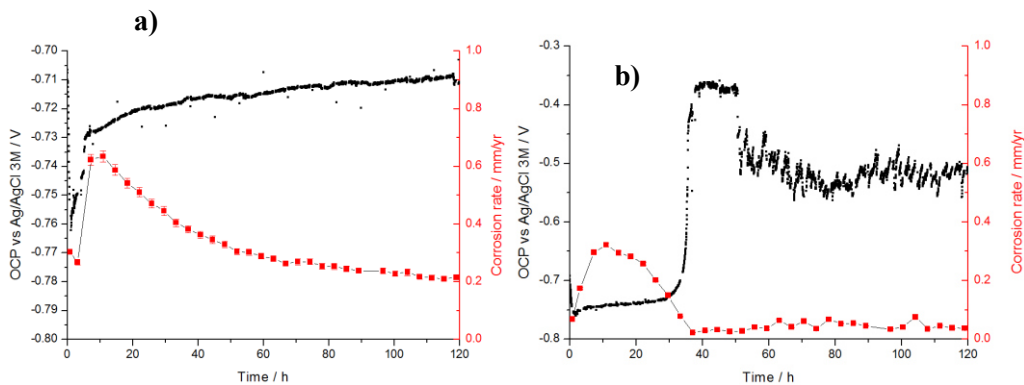


Figure 59 Electrochemical measurements (OCP, LPR) on API 5L X65 carbon steel exposed for 5 days to a saturated CO<sub>2</sub> aqueous solution at pH 6.8, 2g/L NaCl, 80°C. Oxygen contamination = 171 ppb. Two replicas are shown in a) and b).

On the contrary, the second replica test (Figure 59 b) shows a situation more similar to the one reported for an oxygen contamination corresponding to 90 ppb (Figure 57 b). Namely, the OCP raises by 400 mV after one day of exposure time. Then the potential decreases to a +250 mV vs the early OCP value. Moreover, likewise the previous test with a lower content of oxygen, the potential value fluctuates right after the shift. The measured LPR corrosion rate drops as per a pseudo-passivation following the transition of the potential. However once again the working electrode presented several localized corrosion attacks over the surface. Instead of having a full protective pseudo-passive CPL,

the scales did not provide reliable protection against localized corrosion because of the pit-like feature that appeared on the surface. It seems that the iron carbonate pseudo-passive layer cannot resist the presence of  $O_2$  even in small quantities.

Figure 60 shows the effect of localized corrosion on the working electrode in the experimental conditions. The localized corrosion features are large and equally distributed. Evident corrosion products surround the pits.

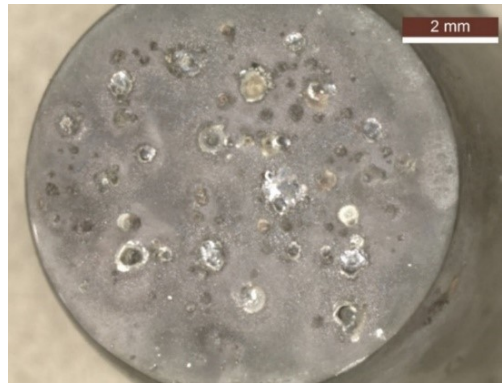


Figure 60 Picture of the carbon steel surface after immersion corresponding to the result presented in Figure 59 b).

#### With 257 ppb of added $O_2$ contamination

The concentration of dissolved oxygen was then set to 257 ppb. Both replica tests have the same characteristic features: a remarkable potential shift occurs after 1-2 days since the beginning of the experiment and the LPR corrosion rate decreases immediately after the OCP transition to higher potentials (Figure 61). The OCP value is not stable and several sudden jumps of OCP are observed after this transition. Both samples present localized corrosion features similar to the ones reported in the previous 90 and 171 ppm tests. These features are uniformly scattered around the surface and are visible to the naked eye.

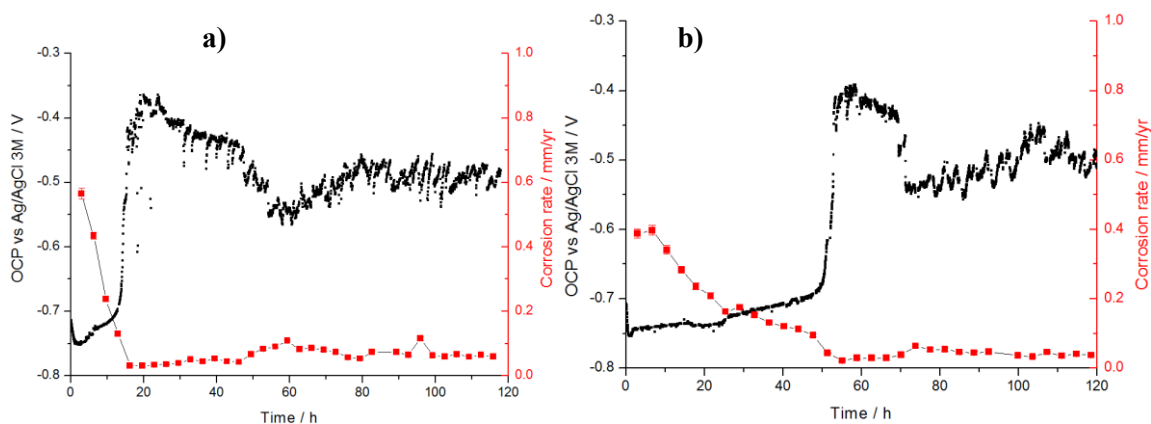


Figure 61 API X65 carbon steel electrochemical measurements (OCP and LPR). The material was immersed into a carbon dioxide saturated solution at pH 6.8, 80°C, 2g/L NaCl. A 257 ppb  $O_2$  contamination was introduced since the start of the test. Two replicas are shown in a) and b).

Figure 62 shows two SEM images of the localized corrosion features that were observed on top of the working electrode exposed to a CO<sub>2</sub> saturated 2 g/L NaCl solution at pH 6.8 and 80°C with the addition of 257 ppb dissolved oxygen. The electrode was exposed for 5 days to this environment and the solution was saturated before the test with the proper amount of O<sub>2</sub>. The images show large localized corrosion structures where a hole occupies the central area whereas a large and thick crown of corrosion products surrounds the center. The dimensions of these features are striking since the inner part has a 100 μm diameter though considering the corrosion products around a global diameter of 300 μm is attained. Far from the localized corrosion features, the corrosion product layer has the same aspect as the one that precipitated without any contamination. Indeed, siderite crystals cover entirely the surface, isolating the metal underneath from the corrosive solution. However, the corrosion products that form the pit-like, particularly the crown around the center, are a mixture of small facet-shaped crystals.

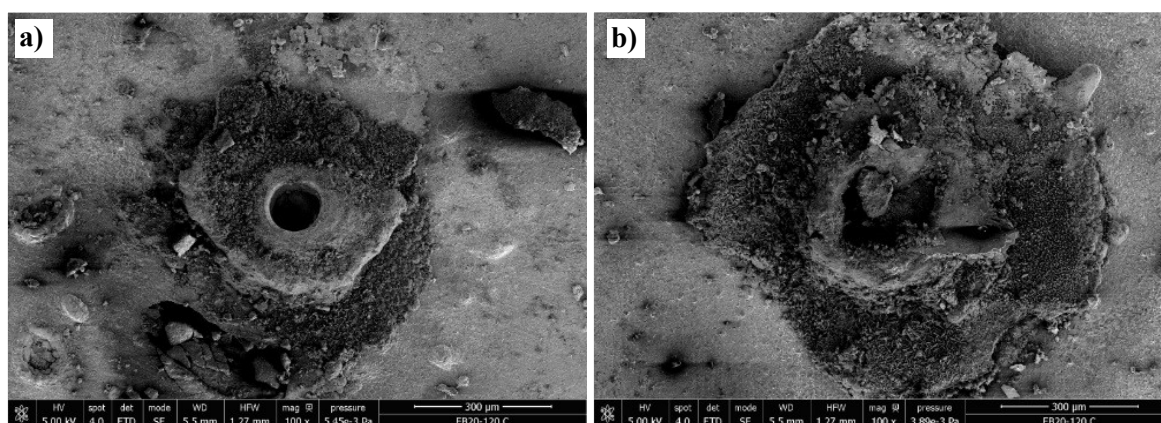


Figure 62 SEM micrographs of the API 5L X65 carbon steel immersed in the reference solution with the addition of 257 ppb of dissolved oxygen, showing corrosion product layer around localized corrosion features. Two localized corrosion features are shown.

Raman analysis performed on the corrosion product crown around the structure reported in Figure 62 a) reveals the presence of goethite, chukanovite, whereas the Raman analysis of the rest of the surface far from the localized corrosion features results in the identification of siderite only [98,99] (Figure 63). However, goethite is probably due to ex-situ oxidation of chukanovite [45]. Anyhow the phases that are present in the corrosion product crown around the pit belong to the hydroxycarbonates and oxides family.

Introducing oxygen into the cell produced significant alterations to the corrosion behavior of the carbon steel in the CO<sub>2</sub>, aqueous solution. When no oxygen was present the samples managed to pseudo-passivate quite rapidly and a good corrosion protection was delivered. However, no sample that was exposed to the contamination managed to have a protective corrosion product layer: either the corrosion rates measured after 5 days of exposure time are too high, or the localized corrosion occurs as suggests the abundance of pit-like formations scattered uniformly over the surface. Particularly for the samples that corrode uniformly, the measured LPR corrosion rate is in the order of magnitude of hundreds of micrometers per year whereas the protection of the CPL in the case without oxygen results in a corrosion rate close to 10 μm/yr.

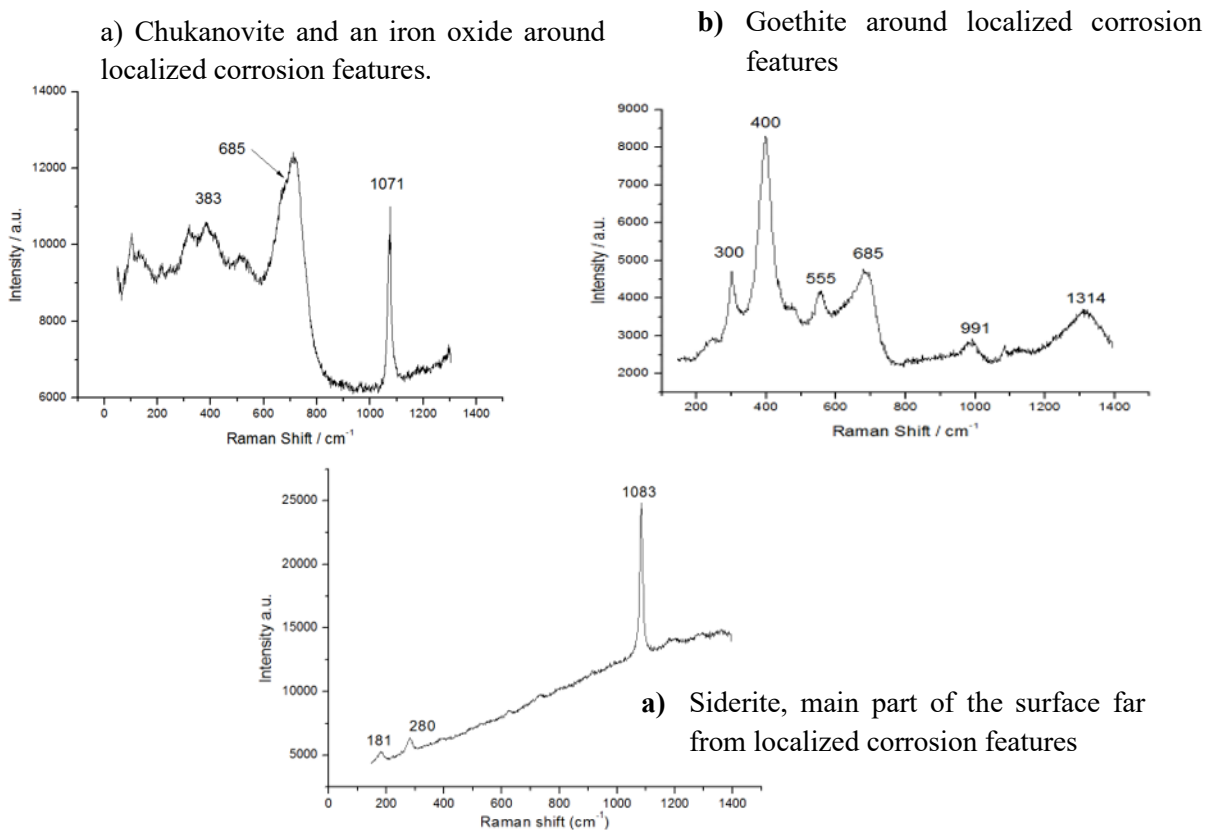


Figure 63 Raman spectra of the corrosion product layer of API 5L X65 immersed in the reference solution with the addition of 257 ppb of dissolved oxygen.

Mass loss tests show an increase in the corrosion rate when the oxygen concentration is increased (Figure 64). This behavior agrees with the rising corrosivity of the media: the dispersion of the results and the deviation at high oxygen concentration can be attributed to the localized corrosion morphology.

The products around the localized corrosion features are oxides-hydroxycarbonates that were never observed when no oxygen contamination was present. These species are only present in the area where localized corrosion occurs whereas the rest of the surface remains covered by siderite. The observed chukanovite is metastable with respect to siderite which is the thermodynamic stable precipitate in these conditions [52,45]. Moreover, siderite is more effective in protecting the metal, reducing the uniform corrosion rate, than chukanovite [100]. As these metastable phases are not equally distributed over the surface but are present only around the pit-like features, their formation cannot be attributed to a thermodynamic transformation from siderite to chukanovite. Their formation is probably due to the local chemistry occurring in the localized corrosion area. Local chemistry of course is influenced by the products of the electrochemical reactions. In fact, iron dissolution and oxygen reduction lowers and rises the pH, respectively. As a result, different values of ions supersaturation than the rest of the surface, trigger a kinetically-driven precipitation of those secondary phases [101]. This hypothesis implies that chukanovite precipitates because of a favorable kinetic relationship and ion concentration ratio in the solution close to the pit-like feature.

Goethite is a  $\text{Fe}^{3+}$  phase, its presence in the system is not due to the oxidation of chukanovite inside the cell because the solution potential is not enough oxidative. A post-test oxidation to the atmosphere should result in the formation of this phase.

From the tests carried in this section, because of a localized corrosion, the pseudo-passivation seems not possible whenever oxygen is present in the corrosive solution: a satisfactory level of protection is not reached. Although the decreased protectiveness of the corrosion product layer can be attributed to the presence of oxygen inside the solution, its impact on the formation of localized corrosion features over the surface cannot be affirmed certainly.

However, a close relationship is observed between the rise of OCP in the anodic direction and the localized corrosion of the samples. The instability of the open circuit potential after the transition can be attributed to the lack of stationary conditions due to the electrochemical reactions and the solution chemistry involved in the localized corrosion process.

Of course, the reference case where no contamination was added into the system is not completely oxygen free, as no experimental set-up will guarantee no oxygen conditions. In fact, the oxygen concentration is close to 10 ppb when CO<sub>2</sub> alone is bubbled in the cell. However, with the investigated medium conditions, Figure 57 b) shows that when the concentration of oxygen reaches 90 ppb the protection is not guaranteed as it is when no oxygen is added. Therefore, considering this specific experimental situation (pH 6.8, 80°C) a threshold concentration seems to exist where the effects related to the presence of oxygen becomes relevant for the corrosion behavior of the carbon steel.

### *Mass loss of corrosion coupons*

The mass loss corrosion coupons that were immersed in the corrosive solution were stripped with inhibited acid following ASTM G1 procedure [102]. The goal of these mass loss measures was to find any correlation between the concentration of dissolved O<sub>2</sub> and the mass loss of the samples. Figure 64 shows the mass loss as a function of oxygen concentration, orange points represent the tests where localized corrosion occurred. The results show that the corrosion rates increase with the dissolved oxygen content, a positive correlation occurs between these parameters (Figure 64). The highest O<sub>2</sub> concentration shows a decrease in the corrosion rate that may be due to the change in corrosion morphology towards more localized corrosion.

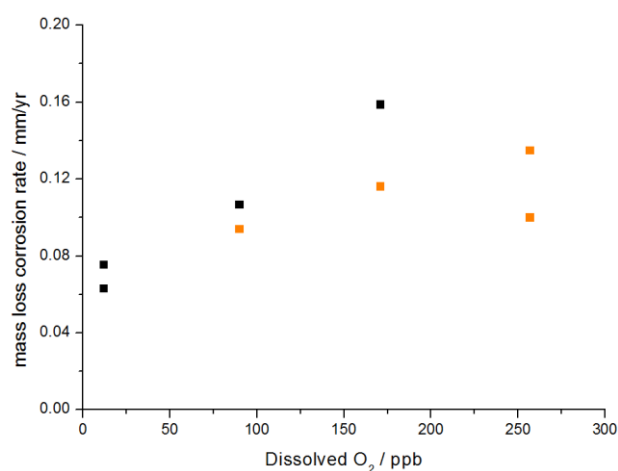


*Figure 64 Mass-loss corrosion rates measured at an increasing level of oxygen concentration in a CO<sub>2</sub> saturated aqueous solution at 80°C, pH 6.8, NaCl 2g/L. Orange represents pitted samples, black ones uniform corrosion samples.*

### 5.3 Contamination test at a lower temperature

The literature review presented in a previous chapter reported that temperature is a key parameter for the precipitation of protective scales. A temperature of 80°C was widely adopted in the previous study for the investigation of the protectiveness of the corrosion product.

Anyhow, the effect of oxygen contamination was investigated at 60°C leaving the other conditions unchanged. This temperature is not high enough to get good protection of the material. Because of the difference in temperature and Henry's law coefficients, the concentration of dissolved oxygen is higher than for the tests at a higher temperature. The dissolved oxygen content of 116 ppb and 348 ppb of dissolved oxygen were tested.

Figure 65 shows the evolutions of the open circuit potential and the corrosion rate versus time. For the both oxygen concentrations, the OCP values remain stable throughout the test and the LPR corrosion rates are considered as stable around 0.05 mm/yr and 0.25 mm/yr for 116 ppb and 348 ppb of dissolved oxygen, respectively.

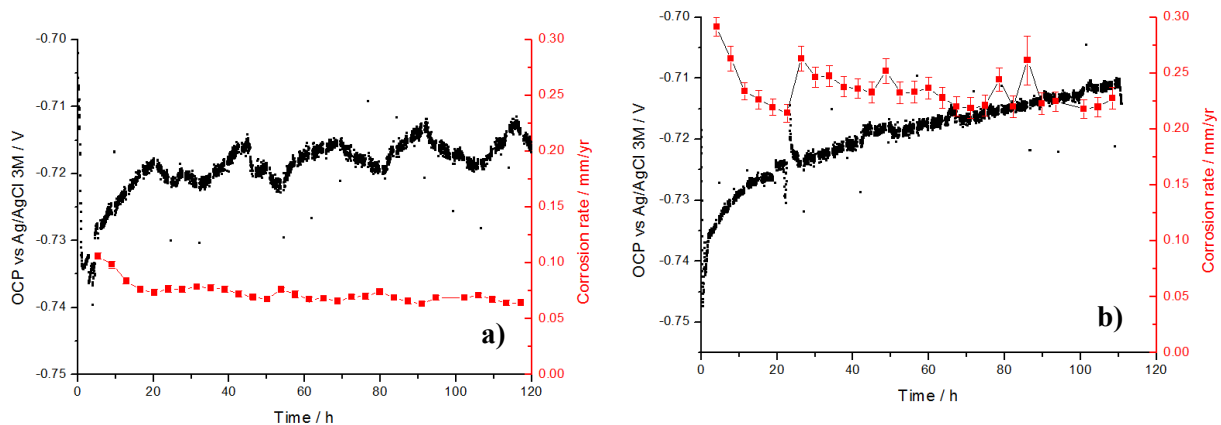


Figure 65 OCP and corrosion rate evolutions versus time for the API X65 carbon steel immersed in the carbon dioxide saturated solution at pH 6.8, 60°C, 2g/L NaCl for: a) 116 ppb and b) 348 ppb of dissolved oxygen.

The electrochemical impedance was measured during time for these new conditions. All impedance diagrams obtained until 5 days are characterized by a single time constant (Figure 66). The charge transfer resistance represented by the diameter of the semicircle on the Nyquist plot increases slowly with time pointing out a gentle diminution of the corrosion rate throughout the exposure time.

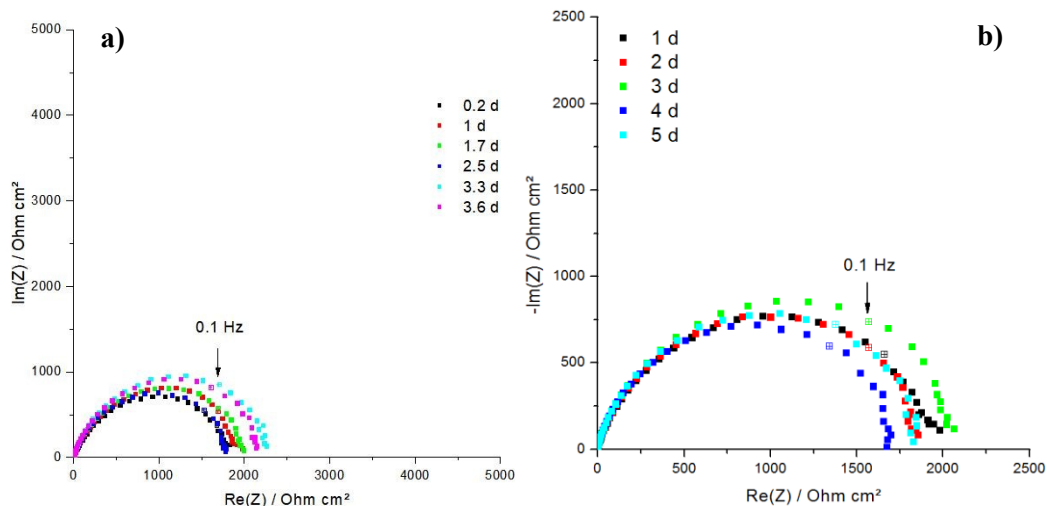


Figure 66 Nyquist impedance diagrams obtained during immersion time for the API 5L X65 carbon steel immersed in a carbon dioxide saturated solution at pH 6.8, 60°C, 2g/L NaCl for: a) 116 ppb and b) 348 ppb of dissolved oxygen.

The corrosion rate for the 116 ppb test has a mean value of  $(1.2 \pm 4) \cdot 10^2 \mu\text{m}/\text{yr}$  whereas at 348 ppb of  $\text{O}_2$ , the rate is  $(2.5 \pm 5) \cdot 10^2 \mu\text{m}/\text{yr}$  (Figure 65). In any case, the corrosion rate value is one order of magnitude greater than when no oxygen is present, pointing out a more aggressive solution. These results are in agreement with the mass loss experiment carried out for the same solution at 80°C (Figure 64). In fact, a higher oxygen concentration results in higher corrosion rates. Moreover, the impedance diagrams do not point out to a second time constant therefore pseudo-passivation is unlikely in these conditions. Nevertheless, the lack of pseudo-passive state cannot be attributed to the dissolved oxygen only. Temperature also plays a major role in the precipitation kinetics and thus in the lack of protectiveness [103].

The results show that the corrosion rate is higher for higher oxygen concentration. It is expected especially at 60°C, a temperature that does not allow optimal development of protective scales [34,40,104].

The lack of pseudo-passivity is mainly due to the lower temperature conditions. The impedance diagrams are characterized by a single time constant (Figure 66) highlighting that the system is charge transfer controlled.

Anyhow the combination of the temperature and content in the dissolved oxygen does not produce protective scales in any of the two situations: the corrosion rate values are one order of magnitude higher than those measured in pseudo-passive state at 80°C. Interestingly the OCP value for both tests was similar and independent from the dissolved  $\text{O}_2$  into the solution.

## 5.4 Introduction of $O_2$ in pseudo-passive state

When oxygen was introduced at the start of the test the electrochemical results show that pseudo-passivation has never been reached. Moreover, localized corrosion occurred in some cases. In those situations, the OCP potential raised two/three times more than the potential increase during pseudo-passivation (around 200/300 mV). Furthermore, the potential after the shift was not stable but several discontinuities occur.

In order to attribute directly this behavior to  $O_2$  and to verify the protectiveness of pseudo-passive scales towards other chemicals, the contamination was introduced at a later stage when the surface was already pseudo-passive. For reaching pseudo-passive state reference conditions were used. Thus, oxygen feed flux was adjusted to have 171 ppb of  $O_2$  dissolved into the solution. The contamination was introduced into the cell rightly after pseudo-passivity (10 hours of pseudo-passivity). Immediately after the introduction of  $O_2$ , marked by a red line in Figure 67, the OCP shifts towards anodic potentials: around + 250/300 mV higher than pseudo-passive potential. Moreover, the measured potential does not remain stable after the transition, the potential falls back and recovers rapidly several times throughout the exposure to the contaminated solution. On the other side, the LPR measurements show that the corrosion rate decreases sharply after the pseudo-passivation only to increase again slightly after the introduction of oxygen.

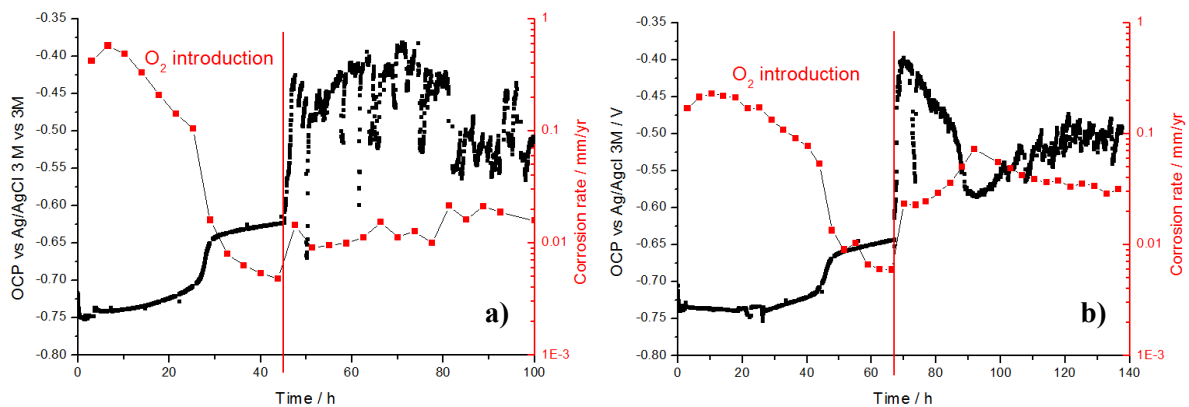


Figure 67 OCP and corrosion rates measured versus time for the carbon steel in immersion in the 2g/L NaCl solution at pH 6.8 and at 80°C and saturated by carbon dioxide. 171 ppb of oxygen was introduced in the pseudo-passivation domain, marked in red. Two replicas are shown in a) and b).

Figure 68 reports SEM images of the localized corrosion features that grew on the corrosion product layer after exposure to an  $O_2$  contaminated solution. The images show large pits with a diameter ranging from 50  $\mu\text{m}$  to several hundreds of  $\mu\text{m}$ . The corrosion products that precipitated in the localized corrosion area have different crystal aspects; their appearance is completely different than siderite that covers the rest of the surface.

Two morphologies of localized corrosion were observed on the surface. The first one is formed by a tubercular siderite structure with some other phases present in the inner part of the pit-like structure (Figure 68 a and b). The diameter of this pit-like structure is around 50  $\mu\text{m}$ . The other morphology is characterized by a disordered conglomerate of different phases. In this last case, no siderite is present at the surface of the corrosion product layer, however the dimensions of these localized defects are bigger with diameters going up to 200  $\mu\text{m}$  (Figure 68 c).

As it was explained in the previous sections, the pseudo-passivation of the surface can occur after different exposure times. Sometimes it is slower and it does not occur in a week of exposure. This fact can explain different morphologies. Nevertheless, these experiments are useful because they can give an insight into the behavior of the corrosion process and the corrosion product layer when oxygen is introduced at a later stage but the surface is still active.

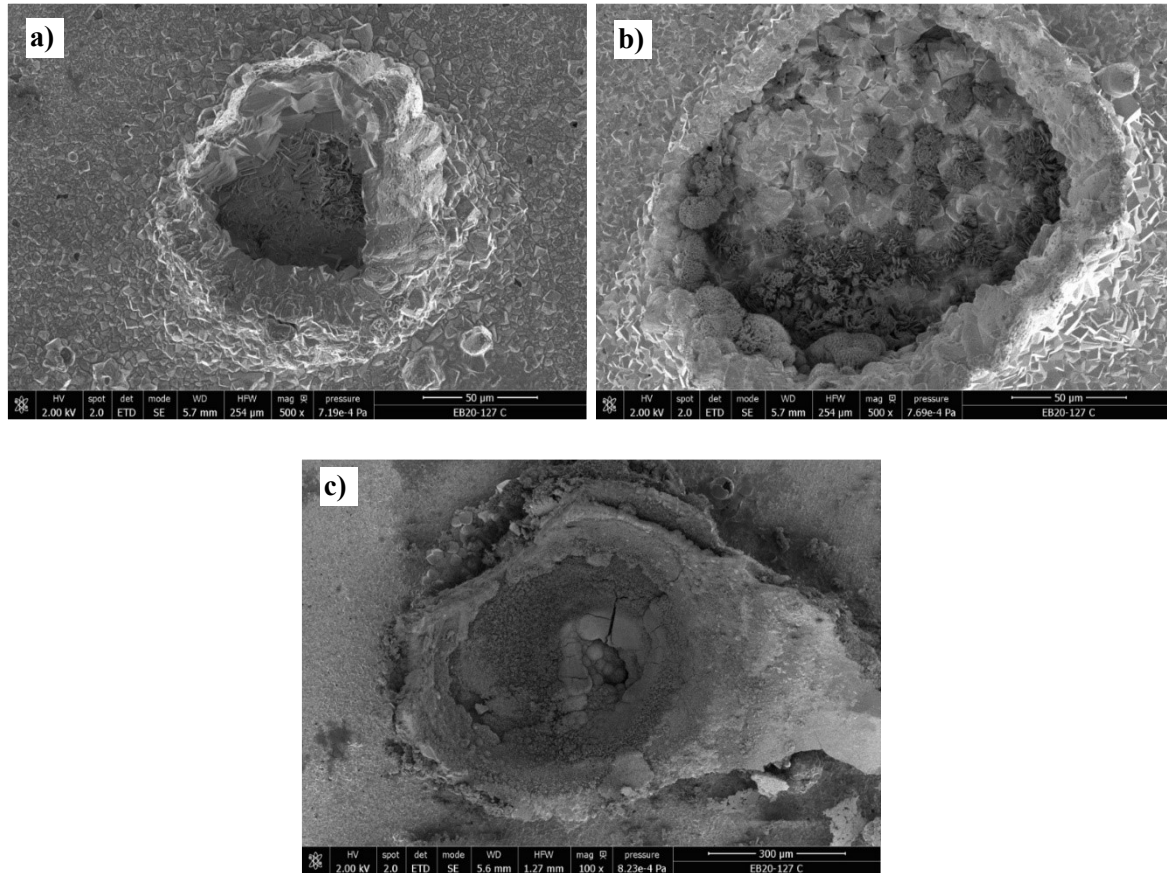


Figure 68 SEM images of the localized corrosion features formed after the introduction of 171 ppb of  $O_2$  contamination in the 2 g/L aqueous solution saturated by  $CO_2$  at pH = 6.8 and at  $80^\circ C$ . Three pit-like features are shown in a), b) and c).

Figure 69 shows the evolutions versus time of the open circuit potential and the corrosion rates of the carbon steel exposed to the pH 6.8 chloride solution saturated in  $CO_2$ , at  $80^\circ C$  with the introduction of 171 ppb oxygen solution before the pseudo passivation (marked by a red line). The data are recorded during one week of exposure to the environment.

The OCP anodic shift does not occur immediately after the introduction of oxygen as in Figure 67 when  $O_2$  was introduced in the pseudo-passive state. Nonetheless, the shift occurs with the same characteristic described before, namely a 200/300 mV rise leading to an increase of the corrosion rate and instability of the OCP value after the transition. Exactly as in the previous cases, the working electrode shows evident signs of localized corrosion as for the other tests performed when the introduction of oxygen was done at initially time  $t_0$  or when the surface was in pseudo-passive state.

The introduction of  $O_2$  in pseudo-passive state produces relevant effects on the electrochemical parameters of carbon steel. Further confirmation was needed in order to check if restoring the initial conditions would result in a return to the pseudo-passive state or if the contamination of oxygen has permanent effects on the system.

Figure 70 shows the results of corrosion tests where oxygen was introduced in pseudo-passive state and then removed after 24 hours of contamination. The OCP evolution follows the behavior described previously: after an initial anodic shift due to pseudo-passivation, a second shift occurs right after the introduction of O<sub>2</sub> into the system. After the introduction of oxygen, the potential remains quite stable by comparison with the previous experiment. The oxygen was removed after 24 hours and the open circuit potential value falls back immediately close to the pseudo-passive potential. The corrosion rate behaves similarly, the introduction of O<sub>2</sub> rises the corrosion rate that drops again once the contamination is suddenly stopped.

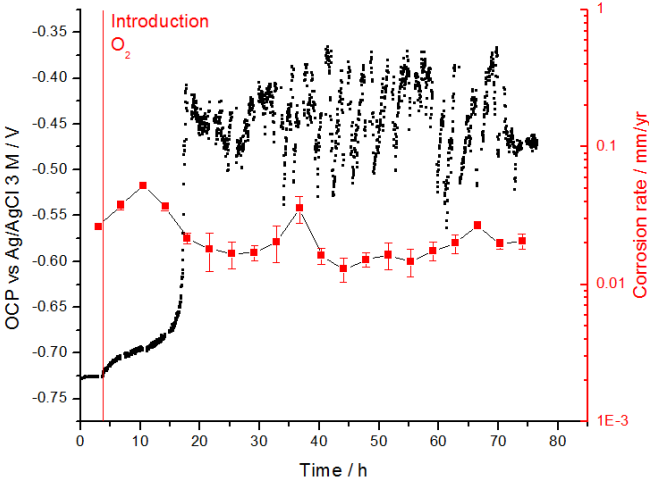


Figure 69 OCP and corrosion rates evolution versus time for the carbon steel immersed in the saturated in CO<sub>2</sub> chloride solution (pH = 6.8, 80°C). O<sub>2</sub> contamination of 171 ppb was introduced inside the electrochemical cell before the pseudo-passivation state of the sample, marked by a red line.

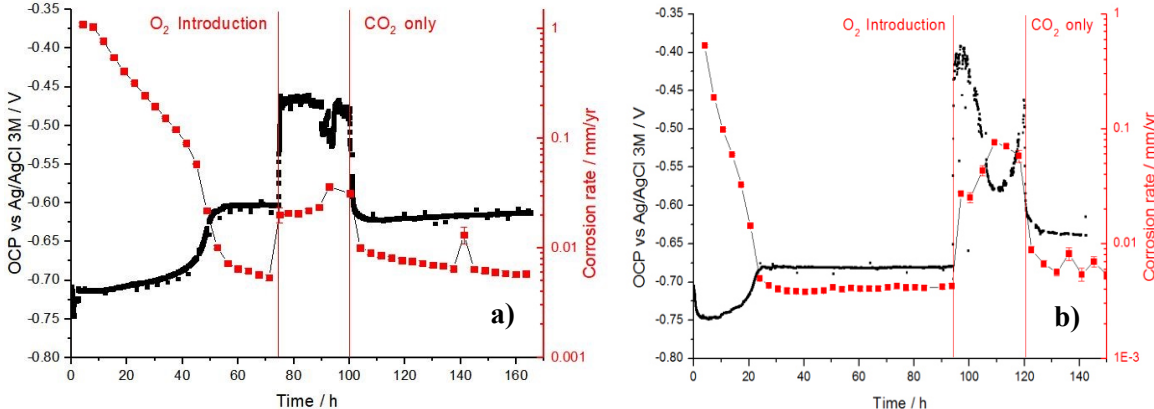


Figure 70 OCP and corrosion rates evolutions versus time for the carbon steel immersed in the saturated in CO<sub>2</sub> chloride solution (pH = 6.8, 80°C). 171 ppb of oxygen was introduced in the electrochemical cell at a moment corresponding to the pseudo-passive state. After 24 hours oxygen was removed from the cell. Two replicas are shown in a) and b).

Although the experiment has been done for a short time period, the introduction of O<sub>2</sub> results in localized corrosion with evident features present on the surface of the sample. The microscopic observation of the carbon steel surface shows the surface far from localized corrosion is fully covered

a)

by protective siderite crystals that do not present any defects and that full coverage of the surface is guaranteed (

Figure 71 a). SEM images in

Figure 71 b and-c show the structure of the pit-like morphologies observed at the end of the test (165 h – 140 of exposure time). Unlike the previous test where no recovery phase (returning to pure CO<sub>2</sub> bubbling) was planned, no secondary phases are observed in this case. Nevertheless, a tubercular structure filled with siderite appears on top of the CPL. As

Figure 71 b and c show, the tubercular structures that formed may be open or close, i.e. completely covered by siderite which is known to be the phase that protect the most from uniform corrosion among the carbonate phases that could precipitate. The dimension of the tubercles is quite big with a 50 µm diameter.

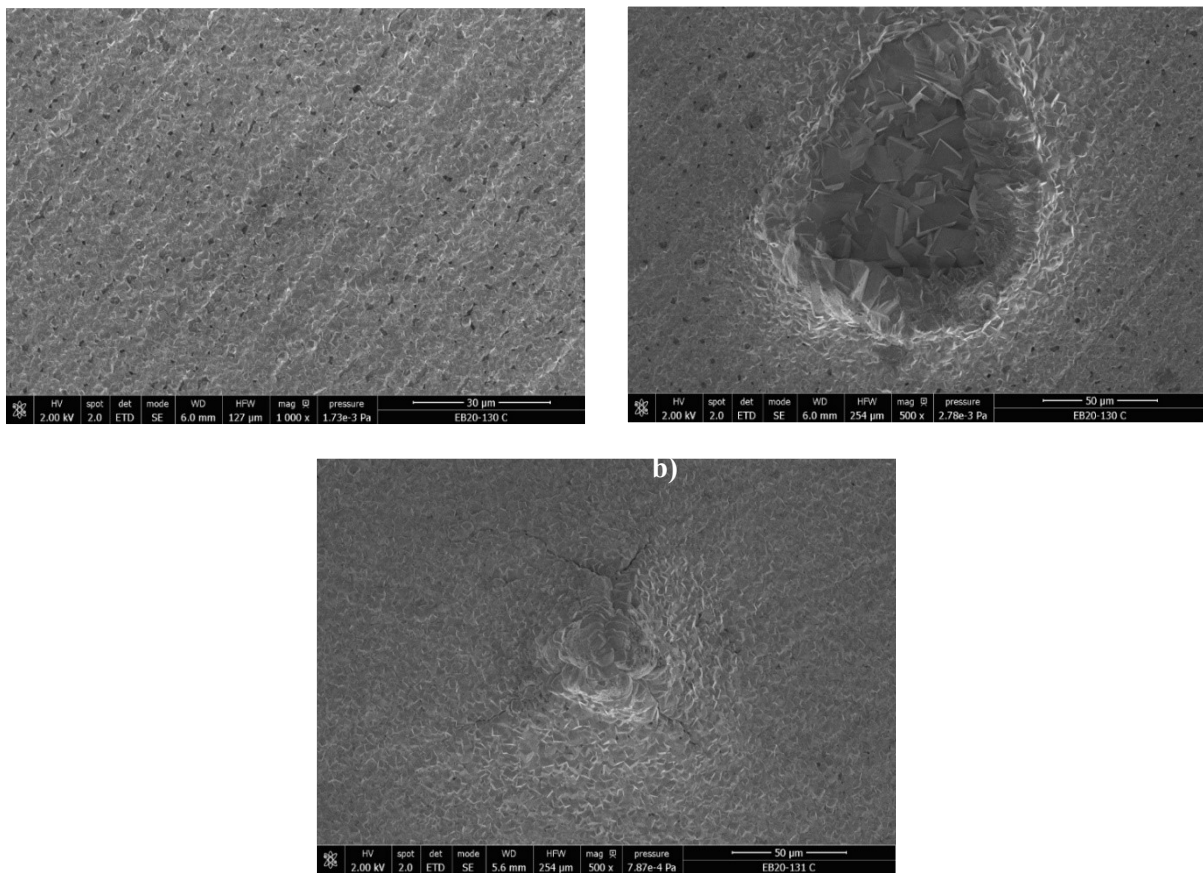


Figure 71 a) corrosion product layer, b) open localized corrosion feature and c) closed localized corrosion feature SEM images of the corrosion product layer formed after exposure to a 171 ppb oxygen contamination introduced in pseudo-passive state for 24 hours. Pseudo-passivation was reached in two days. After 24 hours of exposure to the contamination, the O<sub>2</sub> feed was stopped.

The introduction of oxygen in pseudo-passive state results in a reproducible and immediate rise of the OCP value of 250-300 mV. This effect does not occur when the surface is not at a pseudo-passive state as Figure 69 shows, although in this case, the introduction of O<sub>2</sub> also leads to the formation of pit-like features. These results point out that the localized corrosion morphology is related to the protectiveness of the corrosion product layer. Especially, particular protective scales such as those encountered in pseudo-passive state are exposed to the risk of localized corrosion when oxygen

dissolves into the solution even at low concentrations. In fact, as in the case when O<sub>2</sub> was introduced since the start of the test, the rise in potential value is strongly connected to the localized corrosion of the sample.

Figure 70 shows that restoring the uncontaminated environment results in a return to the electrochemical parameters of the pseudo-passive state since both OCP and corrosion rate values drop to the situation previous to the O<sub>2</sub> introduction into the cell. From the electrochemical results and the SEM observations, it is suggested that the coverage of the localized corrosion feature by siderite stops the propagation of the pits. However, no strong evidence confirms this claim so far, an evaluation of the pit depth as a function of exposure time and contamination will be performed in the following sections in order to support this interpretation.

## 5.5 Recovery test

The introduction of oxygen at the pseudo-passive state results in localized corrosion. The pits that grow on the surface are quite big and clearly visible even to the naked eye. SEM images reveal the presence of other phases around the pit-like features. Those phases are not as protective as siderite; therefore, a question arose whether the pits would continue to grow despite the absence of oxygen. Anyhow at the moment, no evidence was found on the matter, as the surface analysis and electrochemical measurements carried out so far were unfit for detecting pit propagation.

Therefore, a specific test was set up in order to measure the pit depth at different exposure times. The analyzed samples came from specific test moments: namely a pseudo-passive specimen, a pseudo-passive specimen with 3 days of O<sub>2</sub> contamination, one pseudo-passive sample with 3 days of contamination and 24 hours of recovery and one pseudo-passive sample with 3 days of contamination and 96 hours of recovery. ASTM G46 procedure was used in order to determine the pit depth. This standard procedure consists of pickling the surface with an inhibited acid solution in order to expose the metal surface underneath the corrosion product layer [96]. After this treatment, the pit depths were measured with a profilometer Hirox RX-100. Following ASTM G46 the depth of the ten most deep pits is considered for evaluating the propagation of the pits on the specimens. By confronting the samples removed from the electrochemical cell at different exposure times, it is possible to evaluate whether the propagation continued after the initiation of the pit or not.

The electrochemical results of this test are reported in Figure 72 and are in agreement with the ones observed in Figure 67 (2 g/L NaCl solution, pH 6.8, 80°C, 171 ppb O<sub>2</sub> contamination). After the first rise of OCP due to pseudo-passivation a second occurs when O<sub>2</sub> enters the cell. Similarly, the corrosion rate measured obtained from LPR measurements rises after the introduction of oxygen. When O<sub>2</sub> feed stops, the values of OCP and LPR corrosion rate return back to values close to those of pseudo-passivation.

Surface analysis of the pseudo-passive sample confirmed the previous observations and analysis. The layer is compact and covers all the surfaces isolating the metal from the corrosive environment. Most part of the film that grows on the samples exposed to oxygen has the same composition and morphology as the pseudo-passive one. However, several localized corrosion features are present in the film. Figure 73 shows some examples of these tubercular structures. Most of them are composed of two parts: in the inner part, several secondary phases precipitate inside (circled in Figure 73 a and b). Their crystal aspect is completely different from the rhomboedral shape typical of siderite crystals. These secondary phases are found inside the pit-like features only. The outer part of the layer is composed of a siderite tubercle which rises over the corrosion product film. Observing the base of

these tubercular structures, Figure 73 c displays numerous punctual defects where small circular cavities are present on the siderite crystals. These defects were also observed by Rosli *et al* [94]. Another observed morphology of pit like features is reported in Figure 73 d. A corrosion product mountain is present on the film and it is completely covered by the siderite.

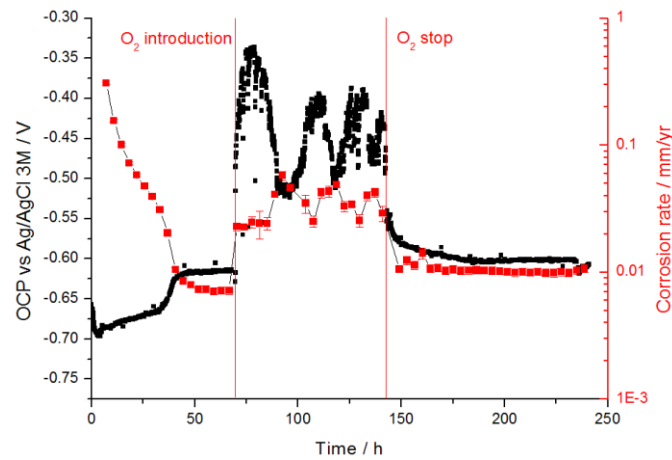


Figure 72 OCP and corrosion rate trends during the time for the API X65 carbon steel in the neutral chloride solution, saturated by  $\text{CO}_2$  ( $\text{pH} = 6.8$ ,  $80^\circ\text{C}$  and containing 171 ppb of  $\text{O}_2$ ). The oxygen feed was turned on and stopped at the moments marked in the figure.

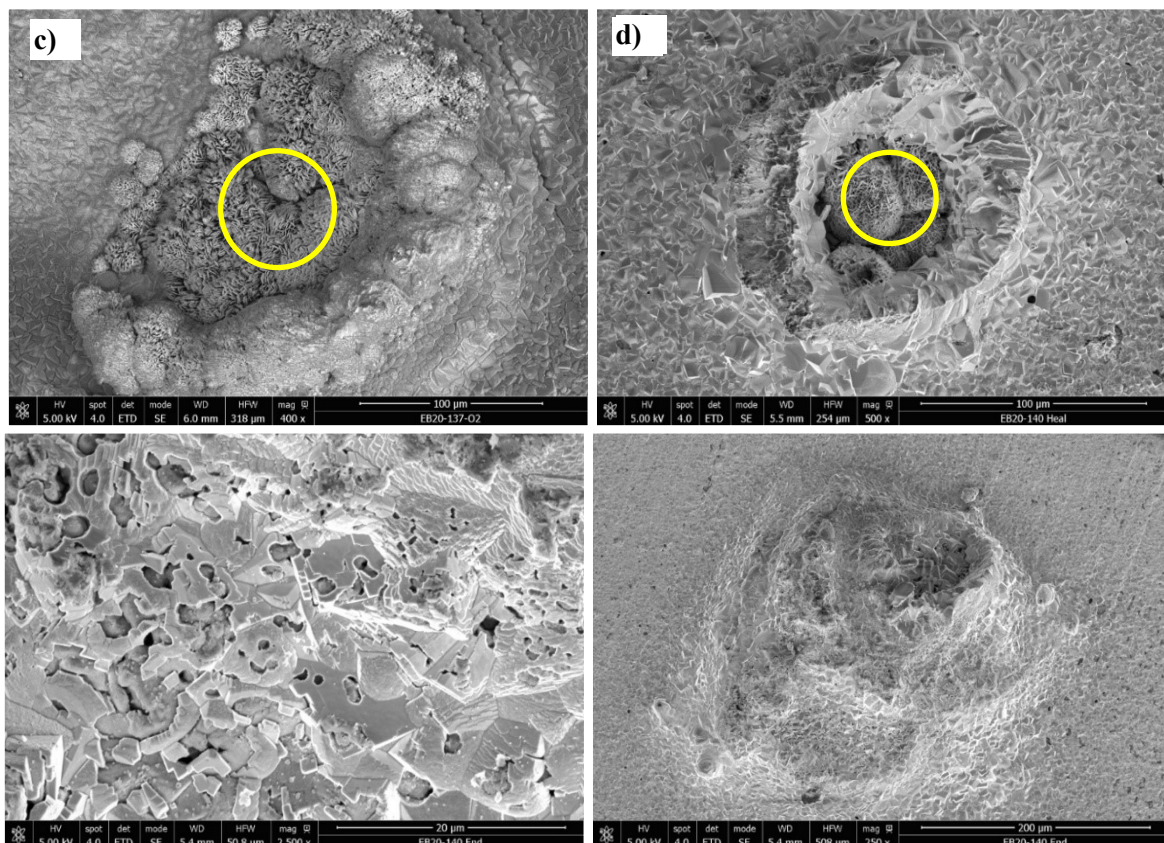
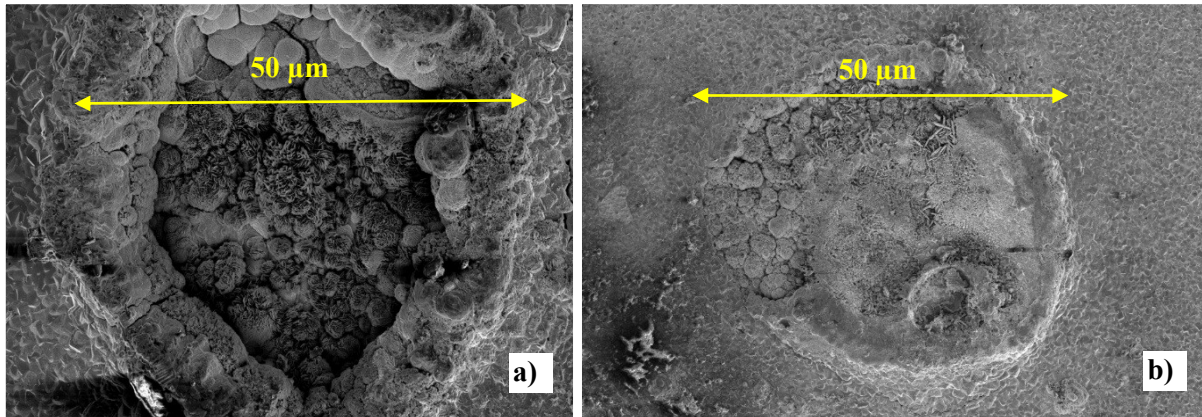


Figure 73 SEM images showing the localized corrosion feature in the testing solution with 171 ppb dissolved  $\text{O}_2$  content: a) “ $\text{O}_2$  sample”, b) “Heal sample”, c) Crystal defects at the base of the tubercular structure composing the pit and d) “End sample”.

In order to determine the composition of the phases in the inner part of the localized corrosion features, surface analysis were performed on samples just before the oxygen feed stop. Figure 74 shows that different phases are present inside the pit-like features. Some facet-like crystals were evident whereas the phases in the inner part of did not have a distinct crystal shape as shown in Figure 74 a and b, respectively.



*Figure 74 SEM micrographs of the localized corrosion features immersed in a CO<sub>2</sub> saturated solution at pH 6.8, 80°C, 2 g/L NaCl. A 171 ppb of dissolved O<sub>2</sub> was introduced in the cell for 3 days after pseudo-passivation.*

Micro Raman analysis was used for the determination of the phases' composition in the inner part of Figure 74. The spectrum shows that those crystals are chukanovite. Chukanovite characteristic peaks are 1070 cm<sup>-1</sup>, 726 cm<sup>-1</sup>, 685 cm<sup>-1</sup>, 383 cm<sup>-1</sup> whereas for magnetite they are 663 cm<sup>-1</sup>, 528 cm<sup>-1</sup>, 311 cm<sup>-1</sup>. The inner part of the tubercular structures in Figure 74 was also analyzed with Raman spectroscopy. The spectra reveal the presence of magnetite (Figure 75 b). It must be highlighted that the precipitation of these phases is limited in the inner part of the pit whereas the composition of the remaining part of the surface is siderite. Raman analysis confirms that siderite is the main component of the corrosion product layer besides the pit-like feature (Figure 75 c).

Figure 76 shows the metal substrate of the samples removed during the test after pickling. The small orange dots that are widespread all over the surface are the result of the pickling procedure and should be disregarded in the consideration of the images. Besides that, the surface states are characterized by a uniform corroded surface, no irregularities or pits are present over the surface. Conversely, all the samples that have endured a period of contamination to oxygen show evident pits and localized corrosion features. The surface observations show that the switch from a generalized corrosion morphology to a localized corrosion one is due to the introduction of oxygen. Furthermore, the diameter of the pits is quite large with a diameter of several hundreds of micrometers.

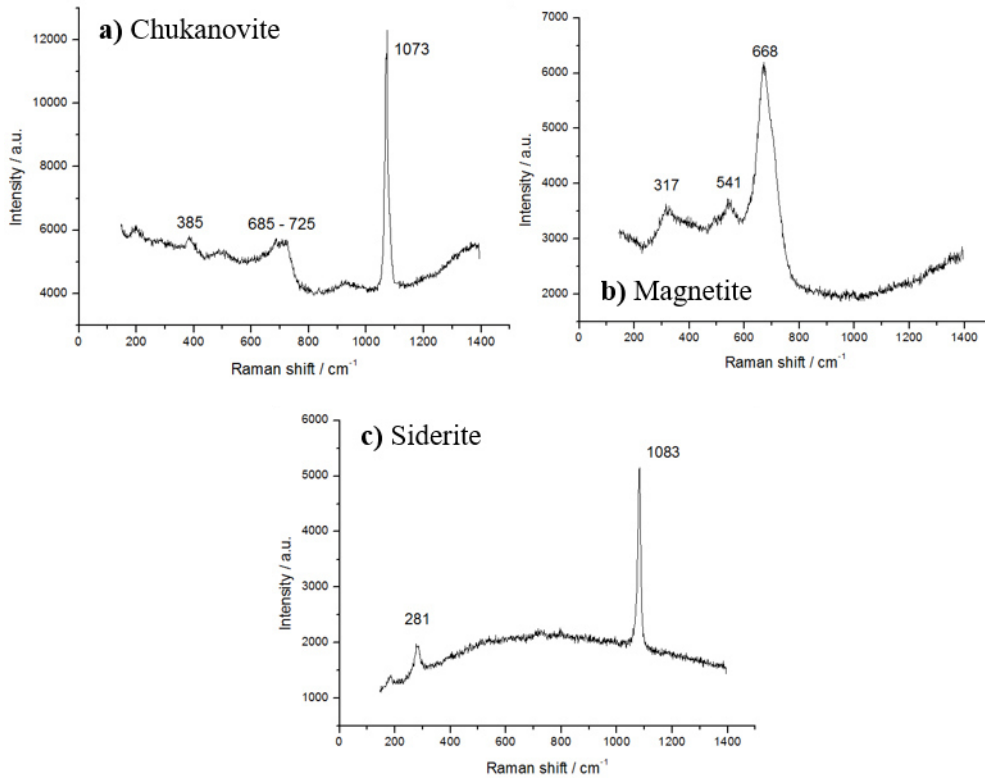


Figure 75 Raman spectrum of the corrosion products over a pit-like feature after exposure to the conditions in Figure 72 before  $O_2$  stop.

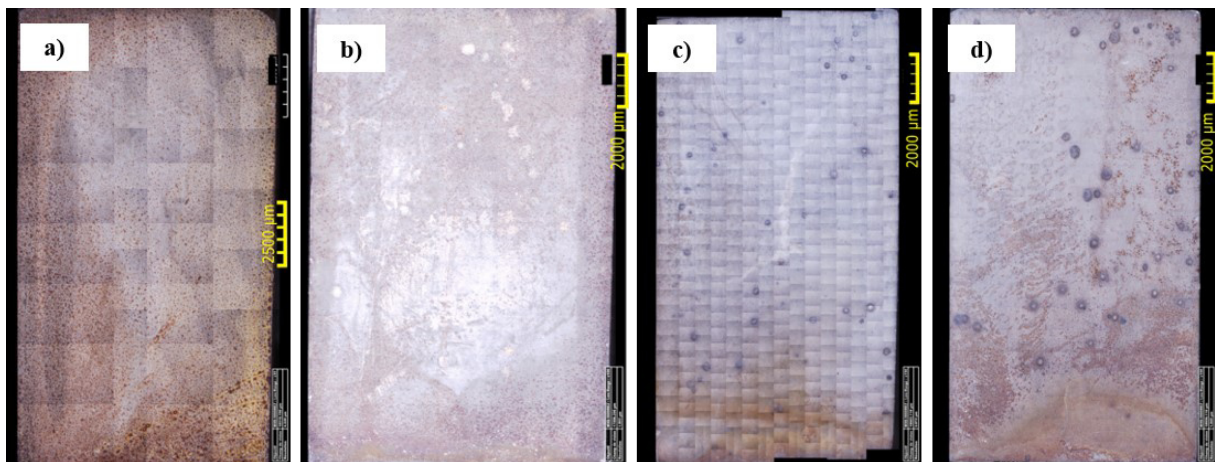
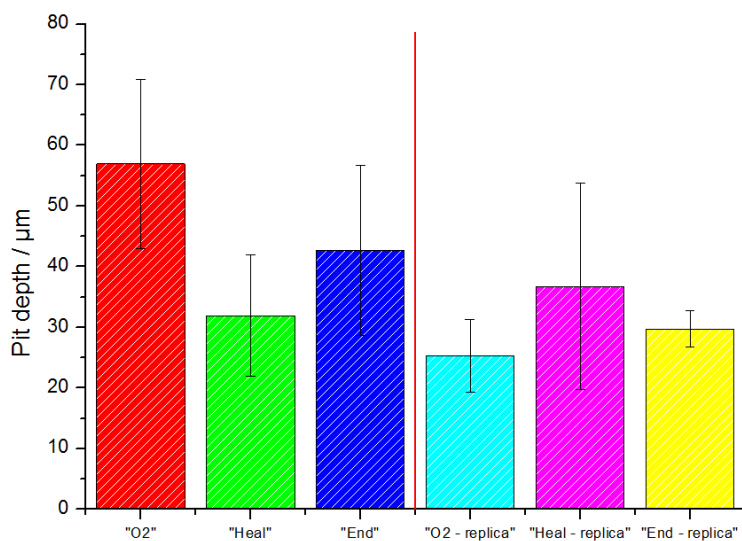


Figure 76 Optical pictures of the carbon steel surfaces, corresponding to different moments in the experiment, and after removing to the corrosion product layer with an inhibited acid solution: a) in pseudo-passive state, b) after  $O_2$  contamination (“ $O_2$  sample”), c) 24 h after  $O_2$  feed cut (“Heal sample”) and d) end of test 4 days after  $O_2$  feed cut (“End sample”).

Figure 77 reports the pit depth of the different samples removed from the cell at different moments. For one test, the “ $O_2$  sample” *i.e.* the pseudo-passive surface exposed to three days of oxygen contamination, has the deepest pits. The pit at the end of a test has a depth less equal to the one of the  $O_2$  sample. The depth for the sample after 24 hours of the interruption of the oxygen feed has mixed results being slightly higher and lower than the depth measured with the  $O_2$  sample. These results point out that the propagation of the localized corrosion features stops when oxygen is not present anymore

in the gas. The pit depth measurements confirm the key role of the oxygen on the localized corrosion features and its effect on the pseudo-passive state.



*Figure 77 Pit depth measurements at different moments in the test following ASTM G46 procedure [96]. Two replicas are shown for each condition.*

The aspect ratio (depth/diameter) of the localized corrosion features is quite low: the depth of the pit is in the order of the tenth of micrometers whereas their diameter is several hundreds of micrometers wide as shown in Figure 77.

The results confirm that the introduction of oxygen shifts the corrosion morphology to localized corrosion since no pits were observed on the sample removed before  $\text{O}_2$  contamination. Localized corrosion seems strictly related to a change in the electrochemical reactions at the surface because of the immediate rise of the OCP value and its instability all along the time of exposure to the  $\text{O}_2$  contamination. This shift in potential is also in relation to the protectiveness of the corrosion product layer. In fact, samples that have not reached pseudo-passive state do not change their potential when 171 ppb oxygen is introduced (Figure 69), the same occurs for oxygen introduced at the start of the experiment. Moreover, the cathodic behavior does not change: the potentiodynamic polarizations show a linear current-potential relationship with and without oxygen (Figure 35 and

Figure 54. pH 6.8,  $80^\circ\text{C}$ , 6 h of exposure time 171 ppb of oxygen contamination). No pseudo-passivation was observed when oxygen was present in the cell either since the start either introduced later for the conditions investigated. Moreover, the measurements of the depth of the pits show that the localized corrosion features stop propagating when  $\text{O}_2$  contamination is not present anymore (Figure 77). In fact, the sample removed after the interruption of the oxygen feed has a pit depth that is lower than the one removed just before the end of the oxygen contamination period. The global result is that the protectiveness of the corrosion product layer is restored once  $\text{O}_2$  does not contaminate the solution anymore.

Micro-Raman analysis reveals that siderite is not the only phase precipitating on carbon steel anymore. Magnetite and chukanovite were identified in the inner part of the tubercles. Anyhow, as for the tests where  $\text{O}_2$  was already introduced at the beginning, the precipitation of these phases is not ubiquitous on the surface, being siderite the principal component of the CPL as the SEM image in

Figure 71 a and the relative Raman spectrum in Figure 63 c display. An increase of pH would lead to the precipitation of thermodynamically stable magnetite. No thermodynamic stability domain is found for chukanovite since it is a metastable form in all conditions. For the experimental parameters considered in this study, the thermodynamic stable observed phase is siderite. Magnetite and chukanovite are found only in specific areas of the corrosion product layer, namely those affected by localized corrosion. Because the presence of magnetite and chukanovite is not generalized but concentrated in particular spots, their precipitation should be due to the local chemical conditions in and around the pits.

The specific local chemistry conditions are linked to the local electrochemical reactions. Particularly, the pH value and the  $\text{Fe}^{2+}$  concentration are probably different in that area of localized corrosion. Besides the stability of the precipitates, the kinetics of formation, that depend on the chemical species saturation, are a key parameter for evaluating the composition outcome of the corrosion product layer [45,52,105].

Once oxygen stops flowing into the cell, the electrochemical measurements and pit depth analysis in Figure 72 and Figure 77 respectively show that the localized corrosion stops, theoretically the pH and iron ion activity should return to the same value all over the surface. The metastable phase should transform into the most stable phase which is siderite however further investigations will be needed in order to confirm this hypothesis.

Results reported in this chapter show a clear link between the localized corrosion features, the pseudo-passivity and the oxygen contamination. Rosli *et al.* reported a mechanism that could explain the appearance of the localized corrosion features [94]. According to Rosli, oxygen induces some defects on the siderite film generating iron oxides which have a lower molar volume with respect to siderite [94]. For this reason, blisters form inside the corrosion product layer. A stagnant solution forms in these blisters and due to the ongoing electrochemical reaction, a lack of oxygen occurs in that spot. The different  $\text{O}_2$  concentrations between that spot and the rest of the surface generate a differential aeration cell where the area with the defect, being less noble, is the small anodic area whereas the rest of the surface behaves as the large cathodic area. The galvanic coupling between the two spots generates localized corrosion.

The results of the pit healing test supports a pit propagation mechanism due to galvanic coupling. Moreover it was observed that pseudo-passive scales are more susceptible to this form of localized corrosion. Indeed the mechanism requires a compact film so to form a differential aeration cell. Finally the chemical environment inside the localized corrosion feature promotes the precipitation of other phases such as chukanovite. This effect is not a direct consequence of oxygen addition since it is localized in the tubercles. A summary of the mechanism is reported in Figure 78.

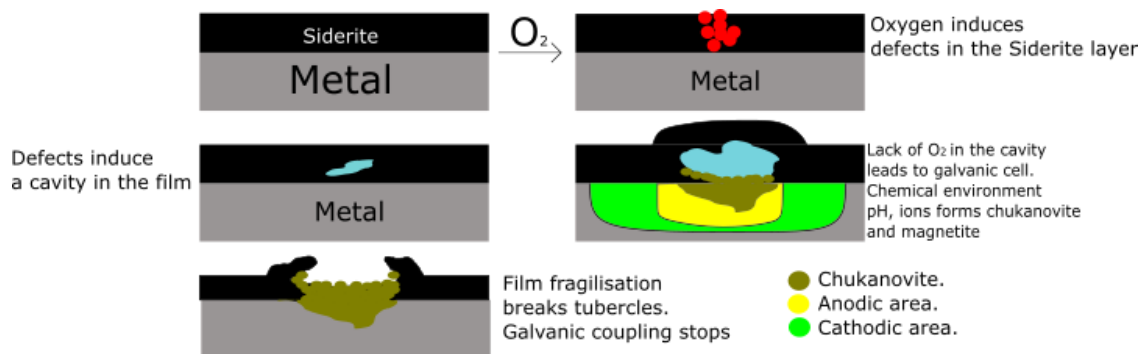


Figure 78 Diagram of the localized corrosion mechanism.

## 5.6 Conclusions on the oxygen contamination in a CO<sub>2</sub> saturated aqueous solution.

In this chapter, the effect of oxygen contamination in different concentrations and contamination moments was investigated. To my best knowledge, the range of dissolved oxygen concentrations is in the hundreds of ppb which is one order of magnitude lower than the tests reported in the literature.

The introduction of oxygen in the environment resulted in radical changes in the corrosion behavior of carbon steel and undermining the protectiveness of the corrosion product layer. The results of this chapter have been obtained in a narrow condition range due to the necessity of promoting a prompt pseudo-passivation by carbonates scales formation. Therefore, further validation of these observations should be performed at higher pressure, temperature and pH even in more critical conditions. Anyhow the main results of this chapter are hereafter summarized:

- The presence of oxygen contamination never leads to a full pseudo-passive state. In fact, the open circuit potential rises significantly (+200 mV / +300 mV) whereas the corrosion potential corresponding to the pseudo-passivity is simply around 100 mV. This transition was observed in all the conditions investigated regardless of the concentration of the introduced O<sub>2</sub> (from 90 to 270 ppb) inside the electrochemical cell. However, the condition where the electrolyte is totally deaerated does not exist. For our experimental procedure, a minimum concentration of 10 ppb is dissolved into the solution. The minimum tested dissolved oxygen contamination that does not result in pseudo-passivation was 90 ppb. Therefore, a threshold concentration for which pseudo-passivation is not possible anymore must exist. Considering the investigated conditions, the results and particularly the fact that O<sub>2</sub> was introduced at the beginning of the test, this threshold concentration must be between 10 ppb and 90 ppb.  
After the open circuit potential transition, the OCP is not stable and it keeps fluctuating.
- Uniform corrosion was always observed, with the adopted techniques of surface analysis, in all the experiments where no added dissolved oxygen was present. Every time that an anodic shift in potential was observed in the presence of oxygen, localized corrosion occurred all over the surface. The presence of localized corrosion does not make the LPR measurements relevant anymore since the Stern-Geary relationship is only valid in the case of uniform corrosion. The fluctuation of potential observed after the transition seems to be linked to the appearance of localized corrosion damages.
- For the experiments where this fluctuating potential transition was not observed, and therefore uniform corrosion occurred, the corrosion rate measured through mass-loss evaluation shows that higher oxygen contamination dissolved in the solution results in higher corrosion rates.
- The same result was observed at a lower temperature (60°C) where a higher corrosion rate was measured for higher dissolved oxygen concentration.
- Potentiodynamic polarization shows that the cathodic reactions in the pseudo-passive state with pure CO<sub>2</sub> is controlled by the charge transfer since a dependency between the potential and the current density is still observed, whereas the introduction of oxygen makes the cathodic reaction limited by mass-transfer. The polarization after 24 hours of exposure for both the contaminated and uncontaminated solution, results in activated controlled reactions (anodic and cathodic) which agrees with the impedance results.
- Oxygen is both responsible for the great anodic shift and for the localized corrosion of the samples. Interrupting the oxygen feed into the electrochemical cell restores the electrochemical conditions before the introduction of the contamination.

- The SEM observations show that the localized corrosion features are present in the samples when an oxygen contamination was introduced only. The measurements of the pit depths show that the localized corrosion features after four days from the interruption of the oxygen feed, are less or equal deep (tenth of micrometers) than the one measured before stopping the oxygen feed. This result indicates that the propagation of the localized corrosion feature stops when oxygen is not present anymore in the solution. The aspect ratio (depth/diameter) of the localized corrosion features is quite low: the diameter of the pits is one/two orders of magnitude greater than their depth. The pits are shallow. This feature indicates that the localized corrosion is not very aggressive due to limited penetration inside the carbon steel.
- The introduction of oxygen inside the system produces an immediate anodic shift of the OCP, these potential features is correlated to the development of localized corrosion. Nevertheless, the introduction of oxygen in a developed corrosion product layer that is not pseudo-passive does not produce any immediate shift. A delay between the two events is observed. This behavior points out that the change of the morphology towards localized corrosion is possible only when the corrosion product layer is in pseudo-passive state.
- Most of the corrosion product layer even in the presence of oxygen is formed by siderite as the Raman analysis reported. The localized corrosion features present different morphologies and compositions depending on the moment of the contamination. Large secondary phases precipitates appear when oxygen is present since the start of the test, whereas tubercular structures are produced when oxygen is introduced at the pseudo-passive state. Magnetite and chukanovite were identified as phases around the pit-hole of the localized corrosion features and inside the tubercular structures. Since these phases precipitated only where the localized corrosion features are, their formation is related to the local chemistry of the system. Finally, because siderite is the thermodynamically stable phase, the precipitation of other products depends on the kinetics of the precipitation reactions, thus temperature and activity of the ions in the solution.

## 6 Summary and general conclusions

CO<sub>2</sub> aqueous solution is a complex environment with a strong interplay between carbon steel and the environment. The iron carbonate corrosion product layer has a key role in protecting the surface. In certain conditions, the scales are particularly protective, and these conditions of the surface were deemed as pseudo-passive.

The first part of the work was concentrated on the selection of proper conditions in order to get a pseudo-passive state. Firstly, the iron carbonate saturation was increased rising the concentration of Fe<sup>2+</sup> with the addition of iron wool into the cell, later the pH was risen to 6.8. The former condition developed pseudo-passive scales however it raised concerns related to the addition of iron ions in the solution, particularly in relation to subsequent investigation with oxygen contamination. The latter condition gave good scaling properties, producing a pseudo-passive layer and keeping the system simple. Pseudo-passivation was identified through the increase of open circuit potential and the appearance of a second time constant at low frequency on impedance diagrams. The increase in modulus impedance at low frequency was concomitant with the anodic potential increase. Electrochemical techniques played a key role in the identification of the moment where pseudo-passivation occurs.

In our selected conditions (pH=6.8, T=80°C, P<sub>CO<sub>2</sub></sub>=0.54 bar, 2% NaCl solution), the corrosion product layer is formed by siderite (FeCO<sub>3</sub>). Magnetite was observed just once locally on the interface between the pseudo-passive corrosion product layer (CPL) and the carbon steel substrate. The CPL layer is compact and has around 10 μm thickness. SEM characterization especially integrating the ion polishing technique, proved useful in order to observe the structure of the pseudo-passive film. Furthermore, GXRD confirmed the SEM observations detecting only siderite on the surface layer.

The pseudo-passive state was investigated using electrochemical techniques. Principally EIS was used since it can give quantitative information about the impedance parameters and allow to propose an electrochemical mechanism about CPL formation and its electrochemical behavior in various experimental conditions. Potentiostatic and potentiodynamic polarization experiments were performed to support the impedance results. The investigation highlights a charge transfer controlled process before pseudo-passivity, whereas after pseudo-passivation, the anodic polarization does not affect over the system impedance.

The impedance measurements after 24 h of exposure to the corrosive solution show an increase of the charge transfer resistance when the working electrode was polarized anodically whereas an increase of charge transfer resistance was observed for cathodic overpotentials. On the contrary in the pseudo passive state, no significant variation of the impedance was observed in the case of anodic and cathodic overpotentials applied.

In the tested conditions, the flow conditions of the system do not have any influence on the impedance when carbon steel is in a pseudo-passive state. The working electrode still managed to reach pseudo-passivity even if a rotation of 600 rpm was applied. Increasing the rotation rate up to 2100 rpm did not cause any variation in the measured impedance.

Regarding these results, the impedance diagrams were analyzed by using electrical equivalent circuits.

The first equivalent circuit feature is that active surface reduction through coverage accounts for all the film protectiveness before pseudo-passivation. After pseudo-passivation, the film coverage and

thickness are such that a mass-transfer limitation kicks in to protect the surface. Coverage was justified by the fact that polarizing the cylindrical working electrode has a major impact on the system impedance and a simplified Randles circuit was used for describing this phenomenon. Moreover, a single time constant was observed. The extracted parameters of the double layer capacity and the charge transfer resistance were used to calculate the  $R_{ct} C_{dl}$  product. This product is independent of the extent of the active surface area since the resistance is directly proportional to the surface whereas the capacity is inversely proportional. Therefore, if a mere coverage effect would take place, this product should remain constant throughout the test [106]. This was indeed observed before the occurrence of a pseudo passive state but significant deviations were observed when the pseudo-passivation started.

The invariance of impedance with respect to potential and rotation rate suggested that mass transfer limited the carbon steel corrosion rate. Furthermore, the increase in OCP indicated that it was indeed the anodic process that slows down more than the cathodic one. Therefore, a mechanism where adsorbed intermediates participate in the iron dissolution reaction was proposed.

Finally, the effect of oxygen contamination in the order of ppb in the  $CO_2$  aqueous solution was investigated. A system was developed to finely tuning the dissolved oxygen concentration in the hundreds of ppb range. This methodology involved mixing carbon dioxide and a  $CO_2/O_2$  gas mixture controlling the flow of the gas mix. An oxygen probe was used to determine the oxygen concentration flowing out the gas cell and so calculate the dissolved  $O_2$  inside the solution using Henry's law.

The results highlighted that oxygen causes localized corrosion when the surface is in pseudo-passive state whereas it results in higher uniform corrosion rates when the surface is active. Localized corrosion features stop propagating when oxygen is not present anymore in the cell. These results were obtained confronting the corrosion coupons before and after oxygen introduction inside the electrochemical cell and measuring their depth once the oxygen flow was stopped.

Besides surface characterization, the effect of  $O_2$  is clearly observed electrochemically by a consistent rise of the OCP (300-400 mV) when it is introduced in pseudo-passive state. Moreover, the OCP fluctuated significantly after the introduction of oxygen in pseudo-passive state. Finally, the impedance data became quite noisy preventing any exploitation of the spectra.

Concerning the electrochemical changes due to the oxygen contamination, the cathodic processes were found limited by the mass transfer in the presence of oxygen whereas they are activation controlled when the scales are pseudo-passive. Potentiodynamic polarization in several conditions was carried out for determining the appropriate Stern-Geary coefficient in the various conditions.

The external "pits" morphology is tubercular. Moreover, in the internal central region of the pits, other phases than siderite were identified with Raman spectroscopy. Particularly, chukanovite and magnetite were observed. SEM observation highlighted that the rest of the surface did not change its composition remaining formed by siderite crystals alone.

This behavior was explained on the basis of the work Rosli where a galvanic coupling occurs between areas lacking oxygen (the "pit") and areas where oxygen gets more easily to the surface (the remaining surface part) [94].

## 7 Perspectives

The experimental results presented in this study were obtained in a narrow set of conditions justified by the necessity of obtaining pseudo-passive scales in the most reliable and fastest ways. This means that the mechanism and observations proposed should be investigated even in different environmental conditions specifically pH, temperature and salt concentration. The investigation should also be extended to other carbon steel materials with higher carbon content so to observe the effect that the perlite network could have on the outcome observed after oxygen contamination.

Besides changing the parameters that we have already mentioned in the previous paragraphs; new contaminants could be added together with oxygen to observe any cumulative effect.  $\text{Ca}^{2+}$  ions and other scaling ions could be interesting to observe.

The results in this study highlighted a threshold oxygen concentration that should cause the localized corrosion features when the surface is pseudo-passive. However, the exact value of this threshold has not been identified yet but it should be between 0 and 90 ppb of dissolved oxygen.

Elucidating the relationship between the corrosion product layer morphology, its composition and its protectiveness requires the combination of both electrochemical technics and surface analysis techniques. However, ex situ analysis is not always precise because it is the sum of different processes that may be hard to convolute. Therefore the implementation of in situ methods should be preferred when possible [107]. Also, new experimental procedures could be implemented such as coupling in situ Raman analysis and electrochemical measurements. This will be useful for acquiring surface changes in the scales when a variation of protectiveness is detected with the help of electrochemical techniques.

## 8 References

- [1] N. Mundhenk, S. Carrero, K.G. Knauss, R. Wonneberger, A. Undisz, Y. Wu, Kinetic and thermodynamic analysis of high-temperature CO<sub>2</sub> corrosion of carbon steel in simulated geothermal NaCl fluids, *Corrosion Science* 171 (2020) 108597. <https://doi.org/10.1016/j.corsci.2020.108597>.
- [2] T. Doi, T. Adachi, T. Kudo, N. Usuki, In situ investigation of CO<sub>2</sub> corrosion in Cr-containing steels in CO<sub>2</sub>-saturated salt solution at elevated temperatures and pressures, *Corrosion Science* 177 (2020) 108931. <https://doi.org/10.1016/j.corsci.2020.108931>.
- [3] H. Liu, J. Sun, J. Qian, B. Wang, S. Shi, Y. Zhu, Y. Wang, A. Neville, Y. Hua, Revealing the temperature effects on the corrosion behaviour of 2205 duplex stainless steel from passivation to activation in a CO<sub>2</sub>-containing geothermal environment, *Corrosion Science* 187 (2021) 109495. <https://doi.org/10.1016/j.corsci.2021.109495>.
- [4] R. Barker, Y. Hua, A. Neville, Internal corrosion of carbon steel pipelines for dense-phase CO<sub>2</sub> transport in carbon capture and storage (CCS) – a review, *International Materials Reviews* 62 (2017) 1–31. <https://doi.org/10.1080/09506608.2016.1176306>.
- [5] W. Sun, Kinetics of iron carbonate and iron sulfide scale formation in CO<sub>2</sub>/H<sub>2</sub>S corrosion, PhD Thesis, Ohio state, 2006.
- [6] R.A. de Motte, R. Barker, D. Burkle, S.M. Vargas, A. Neville, The early stages of FeCO<sub>3</sub> scale formation kinetics in CO<sub>2</sub> corrosion, *Materials Chemistry and Physics* 216 (2018) 102–111. <https://doi.org/10.1016/j.matchemphys.2018.04.077>.
- [7] E. Basilico, S. Marcelin, R. Mingant, J. Kittel, M. Fregonese, F. Ropital, The effect of chemical species on the electrochemical reactions and corrosion product layer of carbon steel in CO<sub>2</sub> aqueous environment: A review, *Materials and Corrosion* (2021). <https://doi.org/10.1002/maco.202012118>.
- [8] A.L. Soli, R.H. Byrne, CO<sub>2</sub> system hydration and dehydration kinetics and the equilibrium CO<sub>2</sub>/H<sub>2</sub>CO<sub>3</sub> ratio in aqueous NaCl solution, *Marine Chemistry* 78 (2002) 65–73.
- [9] Francesco J. Mojica, Frank J. Millero, The values of pK<sub>1</sub> pK<sub>2</sub> for the dissociation of carbonic acid in seawater, *Geochimica et Cosmochimica Acta* 66 (2002) 2529–2540.
- [10] T. Tanupabrungsun, Thermodynamics and Kinetics of CO<sub>2</sub> Corrosion of Mild Steel at Elevated Temperatures, Ohio State, 2013.
- [11] W. Li, B. Brown, D. Young, S. Netic, Investigation of pseudo-pasivation of mild steel in CO<sub>2</sub> corrosion, in: *Corrosion 2013*, Orlando, FL (USA), 2013.
- [12] M. Keddam, O.R. Mattos, H. Takenouti, Reaction Model for Iron Dissolution Studied by Electrode Impedance, *J. Electrochem. Soc.* 128 (1981) 266. <https://doi.org/10.1149/1.2127402>.
- [13] M. Keddam, O.R. Mattos, H. Takenouti, Reaction Model for Iron Dissolution Studied by Electrode Impedance, *J. Electrochem. Soc.* 128 (1981) 257. <https://doi.org/10.1149/1.2127401>.
- [14] K. Heusler, Der Einfluß der Wasserstoffionenkonzentration auf das elektrochemische Verhalten des aktiven Eisens in sauren Lösungen Der Mechanismus der Reaktion  $Fe \rightarrow$

- $Fe^{2+} + 2e^{-}$ , Zeitschrift für Elektrochemie, Berichte der Bunsengesellschaft für physikalische Chemie 62 (5), 1958.
- [15] J. Bockris, D. Drazic, A.R. Despic, The electrode kinetics of the deposition and dissolution of iron, *Electrochimica Acta* 4 (1961) 325–361. [https://doi.org/10.1016/0013-4686\(61\)80026-1](https://doi.org/10.1016/0013-4686(61)80026-1).
- [16] J. Bockris, D. Drazic, The kinetics of deposition and dissolution of iron: Effect of alloying impurities, *Electrochimica Acta* 7 (1962) 293–313. [https://doi.org/10.1016/0013-4686\(62\)87007-8](https://doi.org/10.1016/0013-4686(62)87007-8).
- [17] S. Nestic, N. Thevenot, J.L. Crolet, D.M. Drazic, Electrochemical properties of iron dissolution in the presence of CO<sub>2</sub> - Basics revisited, in: *Corrosion/96*, Denver, CO (USA), 1996.
- [18] A. Kahyarian, B. Brown, S. Nestic, Electrochemistry of CO<sub>2</sub> corrosion of mild steel: Effect of CO<sub>2</sub> on iron dissolution reaction, *Corrosion Science* 129 (2017) 146–151. <https://doi.org/10.1016/j.corsci.2017.10.005>.
- [19] R.F. Wright, E.R. Brand, M. Ziomek-Moroz, J.H. Tylczak, P.R. Ohodnicki, Effect of HCO<sub>3</sub><sup>-</sup> on electrochemical kinetics of carbon steel corrosion in CO<sub>2</sub>-saturated brines, *Electrochimica Acta* 290 (2018) 626–638. <https://doi.org/10.1016/j.electacta.2018.09.114>
- [20] F. Martinelli-Orlando, W. Shi, U. Angst, Corrosion Behavior of Carbon Steel in Alkaline, Deaerated Solutions: Influence of Carbonate Ions, *J. Electrochem. Soc.* 167 (2020) 61503. <https://doi.org/10.1149/1945-7111/ab7d44>.
- [21] A. Kahyarian, B. Brown, S. Nestic, Electrochemistry of CO<sub>2</sub> corrosion of mild steel: Effect of CO<sub>2</sub> on iron dissolution reaction, *Corrosion Science* 129 (2017) 146–151. <https://doi.org/10.1016/j.corsci.2017.10.005>.
- [22] T.C. Almeida, M. Bandeira, R.M. Moreira, O.R. Mattos, Discussion on “Electrochemistry of CO<sub>2</sub> corrosion of mild steel: Effect of CO<sub>2</sub> on iron dissolution reaction” by A. Kahyarian, B. Brown, S. Nestic, [*Corros. Sci.* 129 (2017) 146–151], *Corrosion Science* 133 (2018) 417–422. <https://doi.org/10.1016/j.corsci.2018.02.004>.
- [23] T. das Chagas Almeida, M.C.E. Bandeira, R.M. Moreira, O.R. Mattos, New insights on the role of CO<sub>2</sub> in the mechanism of carbon steel corrosion, *Corrosion Science* 120 (2017) 239–250. <https://doi.org/10.1016/j.corsci.2017.02.016>.
- [24] O.E. Barcia, O.R. Mattos, The role of chloride and sulphate anions in the iron dissolution mechanism studied by impedance measurements, *Electrochimica Acta* 35 (1990) 1003–1009. [https://doi.org/10.1016/0013-4686\(90\)90035-X](https://doi.org/10.1016/0013-4686(90)90035-X).
- [25] Y. Xiang, C. Li, Z. Long, C. Guan, W. Wang, W. Hesitao, Electrochemical behavior of valve steel in a CO<sub>2</sub>/sulfurous acid solution, *Electrochimica Acta* 258 (2017) 909–918. <https://doi.org/10.1016/j.electacta.2017.11.141>.
- [26] E. Remita, B. Tribollet, E. Sutter, V. Vivier, F. Ropital, J. Kittel, Hydrogen evolution in aqueous solutions containing dissolved CO<sub>2</sub>: Quantitative contribution of the buffering effect, *Corrosion Science* 50 (2008) 1433–1440. <https://doi.org/10.1016/j.corsci.2007.12.007>.
- [27] A. Kahyarian, B. Brown, S. Nešić, The Unified Mechanism of Corrosion in Aqueous Weak Acids Solutions: A Review of the Recent Developments in Mechanistic Understandings of Mild Steel Corrosion in the Presence of Carboxylic Acids, *Carbon*

- Dioxide, and Hydrogen Sulfide, *CORROSION* 76 (2020) 268–278.  
<https://doi.org/10.5006/3474>.
- [28] A. Kahyarian, S. Nestic, On the Mechanism of Carbon Dioxide Corrosion of Mild Steel: Experimental Investigation and Mathematical Modeling at Elevated Pressures and Non-Ideal Solutions, *Corrosion Science* (2020) 108719.  
<https://doi.org/10.1016/j.corsci.2020.108719>.
- [29] A. Kahyarian, Mechanism and prediction of mild steel corrosion in aqueous solutions containing carboxylic acids, carbon dioxide, and hydrogen sulfide, PhD thesis, Ohio State, 2018.
- [30] S. Nestic, J. Postlethwaite, S. Olsen, An Electrochemical Model for Prediction of Corrosion of Mild Steel in Aqueous Carbon Dioxide Solutions, *Corrosion* 52 (4) (1996) 280–294.
- [31] A. Kahyarian, B. Brown, S. Nešić, Technical Note: Electrochemistry of CO<sub>2</sub> Corrosion of Mild Steel: Effect of CO<sub>2</sub> on Cathodic Currents, *Corrosion* 74 (2018) 851–859.  
<https://doi.org/10.5006/2792>.
- [32] E. Gulbrandsen, K. Bilkova, 06364 – Solution chemistry effects on corrosion of carbon steels in presence of CO<sub>2</sub> and acetic acid in: *Corrosion 2006*, San Diego, CA (USA), 2006.
- [33] H. Fang, B. Brown, S. Nestic, Sodium Chloride Concentration Effects on General CO<sub>2</sub> Corrosion Mechanisms, *Corrosion* 69 (2013) 297–302.
- [34] S. Nestic, M. Nordsveen, R. Nyborg, A. Stangeland, A mechanistic model for carbon dioxide corrosion of mild steel in the presence of protective iron carbonate films - Part 2: A numerical experiment, *Corrosion* 59 (2003) 489–497.
- [35] J.W. Mullin, *Crystallization*, Oxford Press, 1993.
- [36] E. van Hunnik, B. Pots, E. Hendriksen, The formation of protective FeCO<sub>3</sub> corrosion product layers in CO<sub>2</sub> corrosion, in: *Corrosion/96*, Denver, CO (USA), 1996.
- [37] M.T. J. Greenberg, Precipitation and dissolution kinetics and equilibria of aqueous ferrous carbonate vs temperature, *Applied Geochemistry* 7-2 p185-190 (1992).
- [38] Robert D. Brown, Solubility of iron(II) carbonate at temperatures between 30°C and 80°C, *Talanta* 38-2 p205-211 (1991).
- [39] Sun Wei, Srdjan Nestic. Basics Revisited: Kinetics of Iron Carbonate Scale Precipitation in CO<sub>2</sub> Corrosion, *Corrosion* 06, San Diego, California, 2006.
- [40] S. Nestic, K.-L.J. Lee, A Mechanistic Model for Carbon Dioxide Corrosion of Mild Steel in the Presence of Protective Iron Carbonate Films—Part 3: Film Growth Model, *Corrosion* 59 (2003) 616–628. <https://doi.org/10.5006/1.3277592>.
- [41] K.L.J. Lee, A mechanistic modeling of CO<sub>2</sub> corrosion of mild steel in the presence of H<sub>2</sub>S, Ohio State, 2004
- [42] R. de Motte, Corrosion Deposits on carbon Steels in CO<sub>2</sub> media, R073 – RD/sm – 18-029, IFPEN technical note, 2018.
- [43] B. Ingham, M. Ko, N. Laycock, N.M. Kirby, D.E. Williams, First stages of siderite crystallisation during CO<sub>2</sub> corrosion of steel evaluated using in situ synchrotron small- and wide-angle X-ray scattering, *Faraday Discuss.* 180 (2015) 171–190.  
<https://doi.org/10.1039/c4fd00218k>.

- [44] G.R. Joshi, K. Cooper, X. Zhong, A.B. Cook, E.A. Ahmad, N.M. Harrison, D.L. Engelberg, R. Lindsay, Temporal evolution of sweet oilfield corrosion scale: Phases, morphologies, habits, and protection, *Corrosion Science* 142 (2018) 110–118. <https://doi.org/10.1016/j.corsci.2018.07.009>.
- [45] I. Azoulay, C. Rémazeilles, P. Refait, Corrosion of steel in carbonated media: The oxidation processes of chukanovite ( $\text{Fe}_2(\text{OH})_2\text{CO}_3$ ), *Corrosion Science* 85 (2014) 101–108. <https://doi.org/10.1016/j.corsci.2014.04.004>.
- [46] W. Li, B. Brown, D. Young, S. Netic, Investigation of Pseudo-Passivation of Mild Steel in  $\text{CO}_2$  Corrosion, *Corrosion* 70 (2014) 294–302.
- [47] Omkar A. Nafday, S. Netic, Iron carbonate scale formation and  $\text{CO}_2$  corrosion in the presence of acetic acid, *Corrosion* 05 Paper n. 05295 (2005).
- [48] V. Pandarinathan, K. Lepková, W. van Bronswijk, Chukanovite ( $\text{Fe}_2(\text{OH})_2\text{CO}_3$ ) identified as a corrosion product at sand-deposited carbon steel in  $\text{CO}_2$ -saturated brine, *Corrosion Science* 85 (2014) 26–32. <https://doi.org/10.1016/j.corsci.2014.03.032>.
- [49] J. Han, S. Nešić, Y. Yang, B.N. Brown, Spontaneous passivation observations during scale formation on mild steel in  $\text{CO}_2$  brines, *Electrochimica Acta* 56 (2011) 5396–5404. <https://doi.org/10.1016/j.electacta.2011.03.053>.
- [50] R. de Motte, E. Basilico, R. Mingant, J. Kittel, F. Ropital, P. Combrade, S. Necib, V. Deydier, D. Crusset, S. Marcelin, A study by electrochemical impedance spectroscopy and surface analysis of corrosion product layers formed during  $\text{CO}_2$  corrosion of low alloy steel, *Corrosion Science* (2020) 108666. <https://doi.org/10.1016/j.corsci.2020.108666>.
- [51] R.A. de Motte, A combined experimental and modelling approach to elucidate  $\text{FeCO}_3$  scale formation kinetics. PhD thesis, Leeds (UK), 2016.
- [52] I. Azoulay, C. Rémazeilles, P. Refait, Determination of standard Gibbs free energy of formation of chukanovite and Pourbaix diagrams of iron in carbonated media, *Corrosion Science* 58 (2012) 229–236. <https://doi.org/10.1016/j.corsci.2012.01.033>.
- [53] Yang Yang, B. Brown, S. Netic, M.E. Gennaro, B. Molinas, Mechanical strength and removal of a protective iron carbonate layer formed on mild steel in  $\text{CO}_2$  corrosion, *Corrosion* 2010 Paper n. 10383 (2010).
- [54] V. Ruzic, M. Veidt, and S. Nešić, Protective Iron Carbonate Films—Part 1: Mechanical Removal in Single-Phase Aqueous Flow, *Corrosion* 62 (2006) 419–432.
- [55] V. Ruzic, M. Veidt, and S. Nešić, Protective Iron Carbonate Films—Part 2: Chemical Removal by Dissolution in Single-Phase Aqueous Flow. *Corrosion* 62 (2006) 598–611.
- [56] M. Ko, B. Ingham, N. Laycock, D.E. Williams, In situ synchrotron X-ray diffraction study of the effect of microstructure and boundary layer conditions on  $\text{CO}_2$  corrosion of pipeline steels, *Corrosion Science* 90 (2015) 192–201. <https://doi.org/10.1016/j.corsci.2014.10.010>.
- [57] F. Farelas, M. Galicia, B. Brown, S. Netic, H. Castaneda, Evolution of dissolution processes at the interface of carbon steel corroding in a  $\text{CO}_2$  environment studied by EIS, *Corrosion Science* 52 (2010) 509–517.
- [58] B. Kinsella, Y. J. Tan, and S. Bailey, Electrochemical Impedance Spectroscopy and Surface Characterization Techniques to Study Carbon Dioxide Corrosion Product Scales, *Corrosion* 54 (1998) 835–842.

- [59] Y.J. Tan, S. Bailey, B. Kinsella, An investigation of the formation and destruction of corrosion inhibitor films using electrochemical impedance spectroscopy (EIS), *Corrosion Science* 38 (1996) 1545–1561. [https://doi.org/10.1016/0010-938X\(96\)00047-9](https://doi.org/10.1016/0010-938X(96)00047-9).
- [60] F. Pessu, R. Barker, A. Neville, Understanding Pitting Corrosion Behaviour of X-65 Carbon Steel in CO<sub>2</sub> Saturated Environments: The Temperature Effect, *Corrosion* (2015). <https://doi.org/10.5006/1338>.
- [61] F. Pessu, Investigation of pitting corrosion of carbon steel in sweet and sour oilfield corrosion conditions: a parametric study, PhD thesis University of Leeds, 2015
- [62] J.L. Crolet, N. Thevenot, and S. Netic, Role of Conductive Corrosion Products in the Protectiveness of Corrosion Layers. *Corrosion* (1998) 54 (3): 194–203.
- [63] M. B. Kermani and A. Morshed, Carbon Dioxide Corrosion in Oil and Gas Production—A Compendium. *Corrosion* (2003) 59 (8): 659–683.
- [64] Archie, Electrical Resistivity Log as an Aid in Determining Some Reservoir Characteristics, *Trans. AIME* 146:54-67 (1942).
- [65] A.A. Garrouch, L. Ali, F. Qasem, Using Diffusion and Electrical Measurements to Assess Tortuosity of Porous Media, *Ind. Eng. Chem. Res.* 40 (2001) 4363–4369. <https://doi.org/10.1021/ie010070u>.
- [66] B. Ghanbarian, A.G. Hunt, R.P. Ewing, M. Sahimi, Tortuosity in Porous Media: A Critical Review, *Soil Science Society of America Journal* 77 (2013) 1461. <https://doi.org/10.2136/sssaj2012.0435>.
- [67] J. Han, Y. Yang, S. Netic, B.N. Brown, Roles of passivation and galvanic effects in localized CO<sub>2</sub> Corrosion of mild steel, *NACE - International Corrosion Conference Series* 08332 (2008).
- [68] J. Han, B. N. Brown, and S. Nešić, Investigation of the Galvanic Mechanism for Localized Carbon Dioxide Corrosion Propagation Using the Artificial Pit Technique, *CORROSION* 66 (2010).
- [69] J. Han, D. Young, H. Colijn, A. Tripathi, S. Nešić, Chemistry and Structure of the Passive Film on Mild Steel in CO<sub>2</sub> Corrosion Environments, *Ind. Eng. Chem. Res.* 48 (2009) 6296–6302. <https://doi.org/10.1021/ie801819y>.
- [70] R. Wang, Y. Li, T. Xiao, Li Cong, Y. Ling, Z. Lu, C. Fukushima, I. Tsuchitori, M. Bazzaoui, Using Atomic Force Microscopy to Measure Thickness of Passive Film on Stainless Steel Immersed in Aqueous Solution, *Sci. Rep.* 9 (2019) 13094. <https://doi.org/10.1038/s41598-019-49747-0>.
- [71] Q.Y. Liu, L.J. Mao, S.W. Zhou, Effects of chloride content on CO<sub>2</sub> corrosion of carbon steel in simulated oil and gas well environments, *Corrosion Science* 84 (2014) 165–171. <https://doi.org/10.1016/j.corsci.2014.03.025>.
- [72] B. Ingham, M. Ko, N. Laycock, J. Burnell, P. Kappen, J.A. Kimpton, D.E. Williams, In situ synchrotron X-ray diffraction study of scale formation during CO<sub>2</sub> corrosion of carbon steel in sodium and magnesium chloride solutions, *Corrosion Science* 56 (2012) 96–104. <https://doi.org/10.1016/j.corsci.2011.11.017>.
- [73] S. Papavinasam, A. Doiron, and R. W. Revie, Effect of Surface Layers on the Initiation of Internal Pitting Corrosion in Oil and Gas Pipelines, *Corrosion Science* 65 (2009).
- [74] H. Fang, B. Brown, S. Nešić, Sodium Chloride Concentration Effects on General CO<sub>2</sub> Corrosion Mechanisms, *Corrosion* 69 (2013) 297–302. <https://doi.org/10.5006/0222>.

- [75] J.B. Han, J.W. Carey, J.S. Zhang, Effect of sodium chloride on corrosion of mild steel in CO<sub>2</sub>-saturated brines, *Journal of Applied Electrochemistry* 41 (2011) 741–749.
- [76] F.F. Eliyan, F. Mohammadi, A. Alfantazi, An electrochemical investigation on the effect of the chloride content on CO<sub>2</sub> corrosion of API-X100 steel, *Corrosion Science* 64 (2012) 37–43. <https://doi.org/10.1016/j.corsci.2012.06.032>.
- [77] S. Zhang, L. Hou, H. Du, H. Wei, B. Liu, Y. Wei, A study on the interaction between chloride ions and CO<sub>2</sub> towards carbon steel corrosion, *Corrosion Science* 167 (2020) 108531. <https://doi.org/10.1016/j.corsci.2020.108531>.
- [78] S. Zhang, L. Hou, H. Du, H. Wei, B. Liu, Y. Wei, An electrochemical study on the effect of bicarbonate ion on the corrosion behaviour of carbon steel in CO<sub>2</sub> saturated NaCl solutions, *Vacuum* 167 (2019) 389–392. <https://doi.org/10.1016/j.vacuum.2019.06.038>.
- [79] S.N. Esmaeely, Y.-S. Choi, D. Young, S. Nescic, Effect of calcium on the formation and protectiveness of an iron carbonate layer in CO<sub>2</sub> corrosion, *Materials Performance* 53 (2014) 54–59.
- [80] A.G. Collins, *Developments in Petroleum Science Geochemistry of Oilfield Waters: Chapter 7. Origin of Oilfield Waters*, Elsevier, 1975.
- [81] Hamad A. Alsaari, *Iron (II)-Calcium Carbonate precipitation interaction*, Rice University, 2008.
- [82] H.A. Alsaari, A.T. Kan, M.B. Tomson, Molar Ratio of Ca<sup>2+</sup> to Fe<sup>2+</sup> in the Supersaturated Solution of Iron Carbonate and Calcium Carbonate and in the Precipitate: Relation and Interpretation, SPE, Society of Petroleum Engineers, 2009, p.18.
- [83] H.A. Alsaari, N. Zhang, S. Work, A.T. Kan, M.B. Tomson, A New Correlation to Predict the Stoichiometry of Mixed Scale: Iron-Calcium Carbonate, SPE, Society of Petroleum Engineers, 2012, p.15.
- [84] S. Navabzadeh Esmaeely, Y.-S. Choi, D. Young, S. Nescic, Effect of Calcium on the Formation and Protectiveness of Iron Carbonate Layer in CO<sub>2</sub> Corrosion, *Corrosion* 69 (2013) 912–920. <https://doi.org/10.5006/0942>.
- [85] C. Ding, K. Gao, C. Chen, Effect of Ca<sup>2+</sup> on CO<sub>2</sub> corrosion properties of X65 pipeline steel, *International Journal of Minerals, Metallurgy and Materials* 16 (2009) 661–666. [https://doi.org/10.1016/S1674-4799\(10\)60009-X](https://doi.org/10.1016/S1674-4799(10)60009-X).
- [86] S.N. Esmaeely, D. Young, B. Brown, S. Nescic, Effect of Incorporation of Calcium into Iron Carbonate Protective Layers in CO<sub>2</sub> Corrosion of Mild Steel, *Corrosion* 73 (2016) 238–246. <https://doi.org/10.5006/2261>.
- [87] Z.D. Cui, S.L. Wu, S.L. Zhu, X.J. Yang, Study on corrosion properties of pipelines in simulated produced water saturated with supercritical CO<sub>2</sub>, *Applied Surface Science* 252 (2006) 2368–2374. <https://doi.org/10.1016/j.apsusc.2005.04.008>.
- [88] S.L. Wu, Z.D. Cui, F. He, Z.Q. Bai, S.L. Zhu, X.J. Yang, Characterization of the surface film formed from carbon dioxide corrosion on N80 steel, *Materials Letters* 58 (2004) 1076–1081. <https://doi.org/10.1016/j.matlet.2003.08.020>.
- [89] L.M. Tavares, E.M.d. Costa, J.J.d.O. Andrade, R. Hubler, B. Huet, Effect of calcium carbonate on low carbon steel corrosion behavior in saline CO<sub>2</sub> high pressure environments, *Applied Surface Science* 359 (2015) 143–152. <https://doi.org/10.1016/j.apsusc.2015.10.075>.

- [90] A. Shamsa, R. Barker, Y. Hua, E. Barmatov, T.L. Hughes, A. Neville, The role of  $\text{Ca}^{2+}$  ions on Ca/Fe carbonate products on X65 carbon steel in  $\text{CO}_2$  corrosion environments at  $80^\circ\text{C}$  and  $150^\circ\text{C}$ , *Corrosion Science* 156 (2019) 58–70. <https://doi.org/10.1016/j.corsci.2019.05.006>.
- [91] Y. Xiang, Z. Wang, X. Yang, Z. Li, W. Ni, The upper limit of moisture content for supercritical  $\text{CO}_2$  pipeline transport, *The Journal of Supercritical Fluids* 67 (2012) 14–21. <https://doi.org/10.1016/j.supflu.2012.03.006>.
- [92] J. Sun, C. Sun, G. Zhang, X. Li, W. Zhao, T. Jiang, H. Liu, X. Cheng, Y. Wang, Effect of  $\text{O}_2$  and  $\text{H}_2\text{S}$  impurities on the corrosion behavior of X65 steel in water-saturated supercritical  $\text{CO}_2$  system, *Corrosion Science* 107 (2016) 31–40. <https://doi.org/10.1016/j.corsci.2016.02.017>.
- [93] S. Wang, Effect of Oxygen on  $\text{CO}_2$  Corrosion of Mild Steel. MSc Thesis, Ohio State, 2009.
- [94] Nor Roslina Rosli, The Effect of Oxygen in Sweet Corrosion of Carbon Steel for Enhanced Oil Recovery, Ohio State, 2015.
- [95] B. Ingham, M. Ko, P. Shaw, Mobbassar Hassan Sk, Aboubakar M. Abdullah, N. Laycock, D.E. Williams, Effects of oxygen on scale formation in  $\text{CO}_2$  corrosion of steel in hot brine: In situ synchrotron diffraction study of anodic products, *Journal of the Electrochemical Society* 165(11) C756-C761 (2018).
- [96] ASTM International, ASTM-G46-94: Standard Guide for Examination and Evaluation of Pitting Corrosion, 2018.
- [97] J J.L. Crolet, The electrochemistry of corrosion beneath corrosion deposits, *Journal of Materials Science* 28 (1993) 2577–2588.
- [98] Damien Mollex, Spectre de la Goethite, Lithotheque ENS Lyon, <https://lithotheque.ens-lyon.fr>, 2016.
- [99] A. Michelin, E. Leroy, D. Neff, J.J. Dynes, P. Dillmann, S. Gin, Archeological slag from Glinet: An example of silicate glass altered in an anoxic iron-rich environment, *Chemical Geology* 413 (2015) 28–43. <https://doi.org/10.1016/j.chemgeo.2015.08.007>.
- [100] G.R. Joshi, Elucidating Sweet Corrosion Scales. PhD thesis, Manchester (UK), 2015.
- [101] Ilanith Azoulay, Corrosion des aciers à long terme: propriétés physico-chimique des hydroxysels ferreux, Université de la Rochelle, 2013.
- [102] ASTM International, ASTM G1: Standard Practice for Preparing, Cleaning, and Evaluating Corrosion Test Specimens, 2017.
- [103] S. Netic, K.-L.J. Lee, V. Ruzic, A mechanistic model of iron carbonate film growth and the effect on  $\text{CO}_2$  corrosion of mild steel, *Corrosion/2002*, paper 2237 (2002).
- [104] M. Nordsveen, S. Netic, R. Nyborg, A. Stangeland, A mechanistic model for carbon dioxide corrosion of mild steel in the presence of protective iron carbonate films - Part 1: Theory and verification, *Corrosion* 59 (2003) 443–456.
- [105] I. Azoulay, C. Rémazeilles, Ph. Refait, Oxidation of chukanovite ( $\text{Fe}_2(\text{OH})_2\text{CO}_3$ ): Influence of the concentration ratios of reactants, *Corrosion Science* 98 (2015) 634–642. <https://doi.org/10.1016/j.corsci.2015.06.002>.
- [106] O. Devos, C. Gabrielli, B. Tribollet, Simultaneous EIS and in situ microscope observation on a partially blocked electrode application to scale electrodeposition,

Electrochemical Impedance Spectroscopy 51 (2006) 1413–1422.  
<https://doi.org/10.1016/j.electacta.2005.02.117>.

- [107] R. Barker, D. Burkle, T. Charpentier, H. Thompson, A. Neville, A review of iron carbonate (FeCO<sub>3</sub>) formation in the oil and gas industry, Corrosion Science 142 (2018) 312–341. <https://doi.org/10.1016/j.corsci.2018.07.021>.